

On the compliant behaviour of free-standing Si nanostructures on Si(001) for Ge nanoheteroepitaxy

Von der Fakultät für Mathematik, Naturwissenschaften und Informatik
der Brandenburgischen Technischen Universität Cottbus

zur Erlangung des akademischen Grades

Doktor der Naturwissenschaften
(Dr. rer. nat.)

genehmigte Dissertation

vorgelegt von

Master of Science Engineer

Grzegorz Kozlowski

geboren am 21. April 1983 in Pila (Polen)

Gutachter: Prof. Dr. Thomas Schroeder

Gutachter: Prof. Ph. D. Giovanni Capellini

Gutachter: Prof. Dr. Bernd Tillack

Tag der mündlichen Prüfung: 24. April 2012

Über die Spannungsverteilung in Ge/Si Nanostrukturen auf Si(001) für Ge Nanoheteroepitaxie

Von der Fakultät für Mathematik, Naturwissenschaften und Informatik
der Brandenburgischen Technischen Universität Cottbus

zur Erlangung des akademischen Grades

Doktor der Naturwissenschaften
(Dr. rer. nat.)

genehmigte Dissertation

vorgelegt von

Master of Science Engineer

Grzegorz Kozlowski

geboren am 21. April 1983 in Pila (Polen)

Gutachter: Prof. Dr. Thomas Schroeder

Gutachter: Prof. Ph. D. Giovanni Capellini

Gutachter: Prof. Dr. Bernd Tillack

Tag der mündlichen Prüfung: 24. April 2012

Acknowledgements

Firstly, I would like to thank Prof. Dr. Thomas Schroeder and Prof. Hans-Joachim Müssig for giving me the opportunity to work in the Materials Research Department at IHP and to prepare my PhD there. I would like to express my gratitude especially to Prof. Dr. Thomas Schroeder. Without his encouragements and continuous guidance throughout these two years, this PhD thesis would never come true. In addition, I would like to thank Prof. Dr. Giovanni Capellini for discussions and Prof. Dr. Bernd Tillack and Prof. Dr. Martin Kittler for their support.

I would like to thank Dr. Peter Zaumseil for his support on the x-ray diffraction technique and creative discussions; Dr. Yuji Yamamoto and Dr. Joachim Bauer without whom the samples preparation would not be possible; Dr. Andreas Schubert for transmission electron microscopy measurements and discussions; Prof. Burkhard Dietrich and Dr. Olaf Seifarth for the introduction to Raman spectroscopy and fruitful discussions hereafter; Dr. Armin Fisher for discussions on finite element method calculations; Dr. Tobias Schüllli from the European Synchrotron Radiation Facility in Grenoble (France) for the support during beamtimes; Dr. Lars Zimmermann for introduction to photonics and discussions.

Many thanks to Dawid Kot, Lidia Tarnawska, Dr. Grzegorz Lupina, Jana Matejova, Christian Walczyk, Dr. Jaroslaw Dabrowski, Marvin Zöllner, Oliver Skibitzki, Yvonne Heier, Malgorzata Sowinska, Tomasz Grzela, Dr. Piotr Dudek, Damian Walczyk, Dr. Gunther Lippert, Dr. Christian Wenger, Canan Baristiran Kaynak, Dr. Mindaugas Lukosius, Dr. Thomas Bertaud, and Udo Kaletta for their personal and scientific support, friendly atmosphere, and for being always open to listen and to help.

Last but not least many thanks to my family and my girlfriend Cirsten Wurm for supporting me at each step, for their love and patience that I have put to the test during those years.

Abstract

Due to its superior optoelectronic properties, Germanium (Ge) is attracting increasing interest to build up future photonic modules within Si chip baseline technology. Despite clear advantages of Ge integration in Si technology (identical diamond crystal structure with Si, complementary metal oxide semiconductor (CMOS) compatibility due to no contamination risks etc.), it faces also some true challenges limiting the optoelectronic performance. Among them, thermal and lattice mismatch result in too high defect levels (which act as non-radiative recombination centres). Parasitic diffusion and formation of SiGe alloys at elevated temperatures is also a common problem. In this respect, selective chemical vapor deposition Ge heteroepitaxy approaches for high quality Ge nanostructure growth with reasonable thermal budget must be developed for local Ge photonic module integration.

A promising vision is offered by the compliant substrate effects within nanometer scale Ge/Si heteroepitaxial structures. Here, in contrast to the classical Ge deposition on bulk Si substrates, the thermal and lattice mismatch strain energy accumulated in the Ge epilayer is partially shifted to the free-standing Si nanostructure. This strain partitioning phenomenon is at the very heart of the nanoheteroepitaxy theory (NHE) and, if strain energy levels are correctly balanced, offers the vision to grow defect-free nanostructures of lattice mismatched semiconductors on Si. In case of the Ge/Si heterosystem with a lattice mismatch of 4.2%, the strain partitioning phenomenon is expected to be triggered when free-standing Si nanopillars with the width of 50 nm and below are used. In order to experimentally verify NHE with its compliant substrate effects, a set of free-standing Ge/Si nanostructures with diameter ranging from 150 to 50 nm were fabricated and investigated.

The experimental verification of compliant substrate effects is challenging and requires sophisticated characterization techniques. The main limitation corresponds to a simultaneous detection of a) the strain partitioning phenomenon between Ge and Si and b) the absence of defects on the nano-scale. In this respect, synchrotron-based grazing incidence x-ray diffraction was applied to study the epitaxial relationship, defect and strain characteristics with high resolution and sensitivity in a non-destructive way. Raman spectroscopy supported by finite element method calculations were used to investigate the strain distribution within a single Ge/Si nanostructure. Special focus was devoted to transmission electron microscopy to determine the quality of the Ge

epilayer.

It was found, that although high quality Ge nanoclusters can be achieved by thermal annealing on Si pillars bigger than 50 nm in width, no proof of strain partitioning phenomenon was observed. In clear contradiction to the present NHE theory, no strain partitioning phenomenon was found even for ~ 50 nm wide Si pillars for which the compliant substrate effects are expected. The absence of the strain partitioning between Ge and Si is caused by the stress field exerted by the SiO₂ growth mask on the Si nanopillar. In contrast to such nanostructures monolithically prepared from a Si(001) wafer, first results in this thesis clearly prove the strain partitioning phenomenon within Ge/Si nanostructures on Silicon-on-insulator substrate. Here, the compliant substrate effects were clearly observed for pillar widths even bigger than 50 nm.

This experimental work demonstrates, that NHE with its compliant substrate effects, offers an interesting approach for high quality Ge nanostructures on Si, avoiding even the misfit dislocation network with its non-tolerable electrical activity in Ge nanodevices. However, the theory does not yet include important aspects of thin film growth on the nano-scale and must be further developed. It is the aim of this PhD thesis to provide this experimental basis for the Ge/Si heterosystem.

Finally, it is noted that here developed growth approach is fully Si CMOS compatible and is not only relevant for Ge integration but also for other lattice mismatched alternative semiconductors (GaAs etc.) to enable higher performance / new functions in future Si microelectronics technologies.

Zusammenfassung

Germanium erfährt zunehmendes Interesse für die Entwicklung zukünftiger photonischer Module im Rahmen von Standard-Si-Technologien aufgrund seiner besonderen optoelektronischen Eigenschaften. Trotz klarer Vorteile für die Ge-Integration in eine Si-Technologie, wie beispielsweise die gleiche Gitterstruktur beider Materialien und Kompatibilität zum CMOS-Prozess ohne ein Kontaminationsrisiko, gibt es auch einige Herausforderungen, die die optoelektronische Leistungsfähigkeit beschränken. Dazu gehört die nicht perfekte Übereinstimmung der thermischen Ausdehnungs- und Gitterparameter, welche zu hohen Defektdichten führen, die als Rekombinationszentren wirken können. Interdiffusion und die Bildung einer SiGe-Legierung bei erhöhten Temperaturen ist ein weiteres generelles Problem. Unter diesem Aspekt sind Ansätze der selektiven chemischen Gasphasenabscheidung erforderlich, die das heteroepitaktische Wachstum von Ge hoher Qualität mit moderatem thermischem Budget für die photonische Modulintegration ermöglichen.

Ein vielversprechender Ansatz ist die Ausnutzung des Effekts des sich anpassenden Substrats von Ge/Si-Heterostrukturen in Nanometerdimensionen. Im Unterschied zur klassischen Ge-Abscheidung auf großflächigen Si-Substraten wird hierbei die in der Ge-Schicht aufgebaute Verspannungsenergie aufgrund der thermischen Ausdehnungs- und Gitterfehlanpassung teilweise an die freistehende Si-Nanostruktur weitergeleitet. Das Phänomen der Spannungsaufteilung ist der zentrale Punkt der Theorie der Nanoheteroepitaxie. Wenn die Niveaus der Spannungsenergie korrekt ausbalanciert werden, könnte die Vision eines defektfreien Wachstums von gitterfehlangepassten Halbleitermaterialien auf Si in Nanostrukturen Wirklichkeit werden. Im Falle des Ge/Si-Systems mit einer Gitterfehlanpassung von 4.2% wird das Einsetzen einer Spannungsaufteilung für freistehende Si-Säulen mit einem Durchmesser von 50 nm und darunter erwartet. Zur experimentellen Verifikation der Theorie der Nanoheteroepitaxie mit dem Effekt des sich anpassenden Substrats wurde ein Satz von freistehenden Ge/Si-Nanostrukturen mit Durchmessern von 150 bis 50 nm hergestellt und charakterisiert.

Die experimentelle Bestätigung des Effekts des sich anpassenden Substrats ist schwierig und bedarf anspruchsvoller Charakterisierungstechniken. Die entscheidende Limitierung betrifft die simultane Detektion der a) Spannungsaufteilung zwischen Ge und Si und der b) Abwesenheit von Defekten auf der Nanometerskala. Deshalb wurden Röntgenbeugungsexperimente unter streifendem

Einfall am Synchrotron durchgeführt, um die epitaktische Heterostruktur im Hinblick auf Defekt- und Spannungseigenschaften mit hoher Auflösung und Sensitivität zerstörungsfrei zu untersuchen. Raman-Spektroskopie unterstützt durch Berechnungen mit der Finite-Elemente-Methode wurde verwendet, um die Spannungsverteilung innerhalb einzelner Ge/Si-Nanostrukturen zu charakterisieren. Zusätzlich wurde großer Wert auf die Transmissionselektronenmikroskopie gelegt, um die Qualität der Ge-Schichten zu bestimmen.

Es wurde gezeigt, dass Ge Nanocluster hoher Qualität auf Si-Säulen mit einer Strukturgröße über 50 nm nach einer thermischen Temperung erzielt werden können. Es konnte bewiesen werden, dass keine Spannungsaufteilung, jedoch eine klassische, plastische Relaxation erfolgt. Im Gegensatz zur Theorie der Nanoheteroepitaxie, die eine Spannungsaufteilung für Si-Säulen kleiner als 50 nm vorhersagt, wiesen auch Ge/Si Heterostrukturen in diesen Strukturgrößen in unseren Messungen keine Spannungsaufteilung auf. Das Fehlen des Einsetzens einer Spannungsaufteilung zwischen Ge und Si konnte hauptsächlich auf die durch die SiO₂-Wachstumsmaske hervorgerufenen Spannungen zurückgeführt werden.

Im Gegensatz zu Nanostrukturen, die auf einem Si(001) Wafer aufgewachsen wurden, bestätigen erste Resultate dieser Arbeit das Einsetzen einer Spannungsaufteilung in Ge/Si Nanostrukturen auf Silicon-on-insulator Substraten. Der Effekt des sich anpassenden Substrats wurde sogar eindeutig für Strukturgrößen über 50 nm beobachtet.

Insgesamt zeigt die Arbeit, dass die Theorie der Nanoheteroepitaxie mit sich anpassendem Substrat ein interessanter Ansatz ist, um gitterfehlangepasste Halbleitermaterialien in hoher Qualität in eine Standard-Si-Mikroelektronik-technologie zu integrieren und hohe Leistung und/oder neue Funktionalitäten zu ermöglichen. Natürlich beinhaltet dies nicht nur Ge, sondern auch III-V Halbleiter wie z. Bsp. GaAs. Die Theorie berücksichtigt aber noch nicht einige wichtige Aspekte des Wachstums dünner Schichten im Nanometerbereich. Ursache ist das Fehlen wesentlicher experimenteller Daten, wie sie erst durch moderne Synchrotronquellen zugänglich geworden sind. Es ist dies das wesentliche Ziel dieser Arbeit, diese experimentelle Grundlage für das Ge/Si System zu legen.

Contents

1	Overview	1
1.1	Goal of the thesis	1
1.2	Organization of the thesis	2
2	Introduction	3
2.1	Historical overview	3
2.1.1	Si microelectronics	3
2.1.2	More Moore vs. More than Moore	3
2.2	Photonics	6
2.2.1	Light Source	7
2.2.2	Optical Modulator	10
2.2.3	Photodetector	11
2.3	Ge growth techniques	13
2.4	Nanoheteroepitaxy	16
2.5	Defect physics	22
2.5.1	Dislocation types	22
2.5.2	Dislocation motion	24
2.5.3	Defect sources	25
2.5.4	Defects filtering by reduced growth area	29
3	Experimental background	31
3.1	Sample preparation	31
3.2	Investigation techniques	33
3.2.1	X-ray diffraction	33
3.2.2	Raman spectroscopy	36
3.2.3	Transmission Electron Microscopy	40
3.2.4	Finite Element Method	42
3.3	Sample information	44

4	Results and discussion	47
4.1	Development of selective Ge CVD process on free-standing 150 nm wide Si nanostructures	49
4.1.1	Scene setting	49
4.1.2	Results and discussion	50
4.1.3	Summary	61
4.2	Growth and relaxation study of Ge nanocrystals on free-standing 90 nm wide Si nanopillars	62
4.2.1	Scene setting	62
4.2.2	Results and discussion	62
4.2.3	Summary	71
4.3	Compliant versus plastic relaxation of Ge nanostructures on free-standing sub 50 nm Si nanopillars	73
4.3.1	Scene setting	73
4.3.2	Results and discussion	73
4.3.3	Summary	79
5	Summary and Outlook	80
5.1	Studies motivation	80
5.2	Summary	81
5.3	Outlook	83
5.3.1	Growth mask optimization	84
5.3.2	Ge/Si nanostructures on Silicon-on-insulator (SOI)	84
6	Scientific visibility	89
6.1	Publications in peer-reviewed journals	89
6.2	Own presentations at conferences and courses	90
	Bibliography	91

Chapter 1

Overview

1.1 Goal of the thesis

Silicon (Si), the only material undeniably dominating the microelectronic industry in the 20th century, is approaching fundamental physical limits both within *More Moore* (miniaturization) and *More than Moore* (functionalization) approaches. In consequence, intensive research and development resources are devoted to alternative materials that are to add new, often innovative functions to Si baseline technology without compromising its high performance. In the 21st century, which is believed to be dominated by photonics, one of such promising material candidate is Germanium (Ge). Due to its superior, with respect to Si, optoelectronic properties, Ge offers a vision of high performance photonic modules which converged with integrated circuits would lead to a tremendous breakthrough in data communication and eventually provide high performance functional diversification of Si complementary metal oxide semiconductor (CMOS) platform.

The goal of this PhD thesis is to develop innovative heteroepitaxy growth approaches for high quality Ge nanostructures of thickness smaller than 100 nm on Si(001) substrates. As impurities (i.e. parasitic Si diffusion) and crystal defects (i.e. threading dislocations) limit the optoelectronic performance of Ge photonic modules, such heteroepitaxy approaches must work at a well-controlled thermal growth budget and carefully engineer the strain balance between Si and Ge.

In the classical case of heteroepitaxial Ge thin film growth on bulk Si substrates, the lattice mismatch of 4.2% relaxes plastically by defect nucleation beyond the critical film thickness. As result, defect densities too high for any photonic application are achieved. A promising approach to overcome this

fundamental problem is the concept of nanoheteroepitaxy. Here, Ge nanostructures are grown on free-standing Si nanopillars and the strain energy is not accumulated in the Ge epi-film alone but partially absorbed in the Si nanopillar. This strain partitioning phenomenon is at the very heart of the compliant substrate concept and, if strain energies are correctly balanced, offers the vision to grow defect free Ge nanostructures on Si. Note, that even the misfit dislocation network at the Ge/Si interface is avoided. A clear benefit of this growth approach is due to the well known "p-type doping" of misfit dislocations and their electrical activity which is undesired and difficult to control for Ge nanostructure devices. In this respect, special attention in this dissertation will be focused on structural characterization of Ge nanocrystals and experimental verification of the nanoheteroepitaxy theory as a method to grow defect-free Ge on Si nanostructures.

1.2 Organization of the thesis

The dissertation is ordered as follows. The introduction to the subject together with a brief historical overview of the microelectronic industry and its trends over the last years are given in chapter 2. Here, a detailed discussion of various approaches used for integration of Ge on Si substrate supported by a literature review is presented. In addition, the in-depth theoretical background of nanoheteroepitaxy theory together with the description of defects filtering methods is given. Next, chapter 3 comprises a detailed description of sample preparation and discussion of the main experimental techniques used in the studies. Chapter 4 consists of the main part of the studies. Here, results of the structural characterization together with a detailed discussion are given. Three sections present Ge/Si nanostructures of different feature size investigated using various experimental methods. The main part of the work ends with the summary and the outlook in chapter 5.

Chapter 2

Introduction

2.1 Historical overview

2.1.1 Si microelectronics

Silicon (Si) is the most common material platform in microelectronics. Although the first transistor was fabricated using germanium and other semiconductors show superior semiconductor properties (higher mobilities, higher saturation velocities, larger band gaps), it was Si that has dominated the industry for over 50 years. The reason was the economy of scale. Si is the cheapest technology for integrated circuits. It can be doped with donors or acceptors and can be easily used to form two types of insulators, i.e. SiO_2 and Si_3N_4 , which show an extreme homogeneity over a larger area. As the wafer size increased, integrated circuits could be built with an increasing number of transistors. In consequence of miniaturization, even more transistors could be placed on a single Si chip.

2.1.2 More Moore vs. More than Moore

In 1965, the director of Research and Development Laboratories of electronics pioneer Fairchild Semiconductor, Gordon E. Moore, drew a line through five points representing the number of components per integrated circuit for minimum cost per component developed between 1959 and 1964. This line showed that the number of transistors in a circuit increased exponentially and doubled approximately every two years. According to Moore, there was no indication that the rate of increase would significantly change within the next ten years, in which "economics may dictate squeezing as many as 65000 components on a single Si chip" [1]. The history has proven, though, that due to astonishing

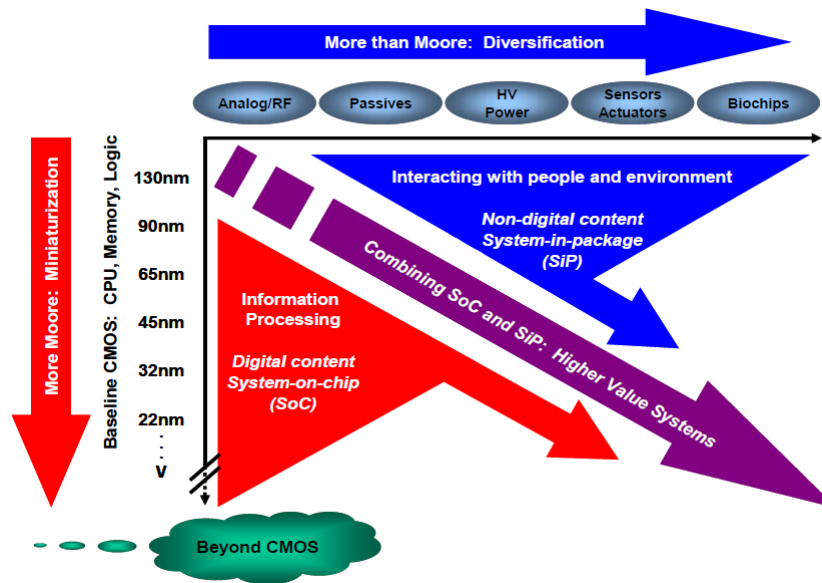


Figure 2.1: Two approaches in the nowadays microelectronic industry: More Moore and More than Moore [3].

progress in Si technology, the estimation was correct during the next 50 years.

Although in 1995 on reviewing the industry status, Moore concluded that "the current prediction is that this is not going to stop soon" [2], after the year 2000 many, including its author, stated that the Moore's law cannot be maintained forever. In order to clarify and substantiate the main technological requirements and needs to increase the performance of integrated circuits, the International Technology Roadmap for Semiconductors (ITRS) [3] was created. Although intensive research was conducted and many development resources were devoted to reach the milestones set by ITRS, the number of aspects for which "manufacturable solutions are not known" within the next few years is still growing from year to year. It is clear that from the physical point of view, the miniaturization process will finally reach its limits at the atomic level. Sooner than the technological limitation, however, the economical factors will probably become the fundamental barrier. This is due to the costs of R&D, testing and developing, building, and maintaining fabrication facilities. These costs increase exponentially [4, 5] as the process of Si complementary metal oxide semiconductor (CMOS) technology shrinks the dimension of devices. Since fewer developers could afford to follow the *More Moore* strategy, an alternative arose.

The miniaturisation of Si CMOS baseline depicted on the vertical axis

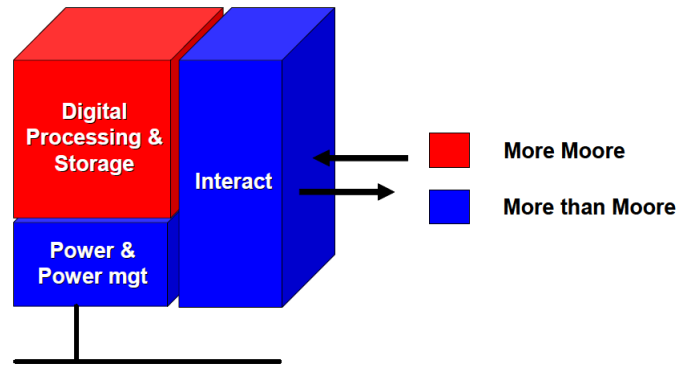


Figure 2.2: A product based on More than Moore approach combining modules of different functions [3].

in Fig. 2.1, works well for the digital components like microprocessor, memory or logic. However, this is not the case for the analogue world and such elements like radio frequency (RF) devices, passive components, sensors or Micro-Electro-Mechanical systems (MEMS) which play an equally important role in nowadays microelectronic products. On this basis, an alternative to *More Moore* approach is a trend known as *More than Moore* presented on the horizontal axis in Fig. 2.1. It is focused on diversification rather than miniaturization. It can be viewed as combining modules of different functions: digital signal and data processing, interaction with the people and/or the environment (e.g. via sensors and actuators) as well as powering (see Fig. 2.2).

Adding new functionalities to the existing Si CMOS baseline can be realized by System-On-Chip (SOC) or System-In-Package (SIP) [6]:

- SOC refers to a monolithic integration of all digital and analog elements on a single Si chip via heteroepitaxy, wafer bonding or nanostructure printing. It requires lower power consumption and less board area. An example of SOC solution are multiple core processors.
- SIP on the other hand, are many integrated circuits stacked vertically, connected by wires (e.g. through Silicon via (TSV)) and combined in a package. Each chip can be built separately with its own dedicated technology. Additionally, the purpose of the whole package can be modified by changing the design of only one building block. SIP offers thus a plug-and-play approach easily adjusting to the demands of different markets.

2.2 Photonics

While the twentieth century technologies were dominated by microelectronics, photonics is believed to prevail the twentieth first century [7]. The performance of a microprocessor is limited by the efficiency of getting information in and out of the processor. As the functionality of a Si circuit is increasing, the rate of data transfer on a Si chip is getting larger. Metal wires used nowadays as interconnects are unlikely to support this increasing demand [8]. In consequence, Si circuits will encounter an interconnection bottleneck in the near future. The main points of concern are information latency, high power consumption, and heat generation. Optical interconnects on the other hand, offer a much higher transfer bandwidth and low demand of energy.

The necessity of photonics in More than Moore approach can be understood on the example of wireless communication. In order to fulfil the increasing demand of data transfer, nowadays wireless local area network (WLAN) modules are realized with BiCMOS technology which offers higher operation speed and better signal to noise ratio. Additional problem is the attenuation of radio signal when moving away from the transceiver. This results in the so-called dead zones (e.g. tunnels) where no wireless signal is available. An alternative is offered by the Radio-over-Fiber (RoF) technology which utilizes light modulated by a radio signal and transmitted via optical fiber. The main advantages of RoF is decreased attenuation, low cost and complexity.

As result, converging electronic and photonic integrated circuits would lead to a tremendous breakthrough in data communication and eventually provide high performance functional diversification of Si chip craved by More than Moore strategy. Optical interconnects require, however, the development of Si CMOS compatible technologies of generation, guidance, control, and detection of photonic signal. Fig. 2.3 shows a schematic illustration of basic components needed to design an electronic-photonic integrated circuit (EPIC), i.e. optical system integrated with CMOS on a Si platform.

It turns out that building individual optical components is as much important as their integration on Si chip. One of the biggest challenges is the choice of materials to be used. A natural choice is Si. However, its indirect band gap makes it a poor light emitter. It lacks a strong electro optic effect required in light modulation and has low absorption coefficient in the range of wavelengths commonly used in optical communication, i.e. 1.3 - 1.55 μm (transmission window of SiO₂ optical fibers). In consequence, photonic elements are nowadays

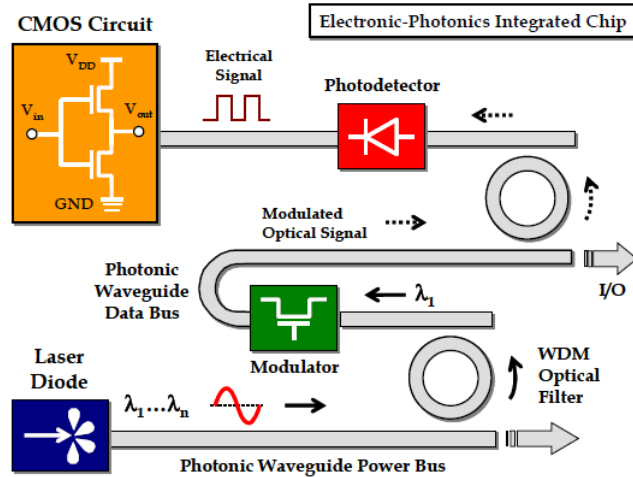


Figure 2.3: Combined Electronic-Photonics Integrated Circuit (EPIC) [9].

mostly made from direct band gap III-V compounds like GaAs and InP due to their superb optical properties. However, those materials are at present incompatible with Si technology and cannot be easily integrated with Si CMOS integrated circuit. The complexity of integration with Si technology can be avoided when a group IV semiconductor like Ge is used.

Due to its interesting optoelectronic properties, Ge has been experiencing a renaissance as a semiconductor material for the past few years. In the following paragraphs the main achievements in the development of Ge-based photonic devices required for EPIC system are discussed.

2.2.1 Light Source

Much work was dedicated to demonstrate light generation by Ge, Si and SiGe alloy [10, 11, 12, 13, 14, 15]. As result, the emission spectra in the range from 1.1 up to 2.2 μm is covered by $\text{Si}_{1-x}\text{Ge}_x$ compound with the strongest light intensity corresponding to Ge LED. Since Si and Ge are indirect semiconductors, in order to conserve the momentum, the radiative processes are mediated by lattice vibrations, i.e. phonons. The phonon population in Ge is higher than in Si or SiGe and results in the highest light intensity of a diode [13].

To support an EPIC system with a strong optical signal, a light amplification by stimulated emission of radiation (laser) with a high quantum efficiency is required. A laser can be built using already mentioned LED when additionally the inversion of electronic states inside a highly reflective optical cavity is realized.

Laser Diode

Although Ge is more promising than Si to build a laser diode, lattice vibrations partitioning in light generation in an indirect band gap semiconductor would limit its performance. Additionally, heat generated during the recombination processes would shorten its life time. On the other hand, an efficient light emission and detection is provided by direct interband transitions. Direct band gap semiconductors are thus more preferable for light sources.

The direct band gap at the Γ point of Ge which amounts to 0.8 eV is slightly bigger than the indirect band gap at L point of 0.66 eV (see Fig. 2.4). It was shown, that local band edges in Ge band structure can be controlled by strain [16, 17]. In consequence, depending on the strain sign, the local extrema at Γ and L points will shift upwards or downwards in the energy scale. Moreover, the impact of strain is different for different bands as shown in Fig. 2.4. For example, under tensile strain the lowering of Γ band occurs faster than the lowering of L band. As a result, by applying tensile strain of around 1.5%, Ge can be transformed into a direct band gap material. Due to the decrease of the energy gap, a red shift of the emitted spectra will be observed. It can be, however, compensated by doping with electrons which gives an additional flexibility in the choice of wavelength emission (Fig. 2.5). As result, band gap engineering together with band filling (electron doping) makes Ge a promising candidate for Si CMOS compatible laser [18, 19].

Quantum Cascade Laser

A quantum cascade laser (QCL) is a laser that can be built using an indirect semiconductor. When used as a unipolar device, the generation of light occurs via intraband transitions (THz regime) of either electrons or holes [7] (see Fig 2.6). QCL was first demonstrated in 1994 using III-V compounds (GaInAs and AlInAs) [20]. Si/SiGe and Ge/SiGe QCL have, however, many advantages over the laser based on III-V materials. They can be easily and cheaply integrated with Si technology and they lack polar optical phonon scattering [7]. The emission wavelength of QCL can be further tuned by strain, composition, and thickness of quantum wells. Si/SiGe [21, 22] and Ge/SiGe [23] structures were demonstrated.

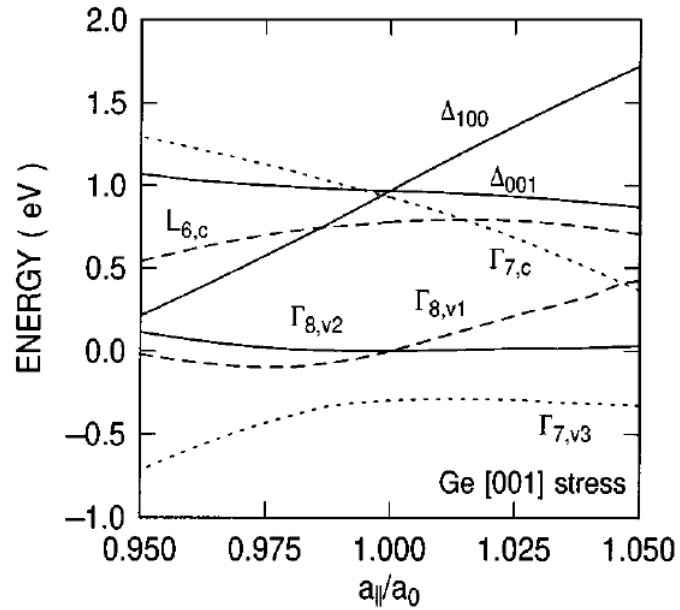


Figure 2.4: The calculated shift of valence and conduction bands at various symmetry points in Ge as a function of in-plane biaxial strain [16].

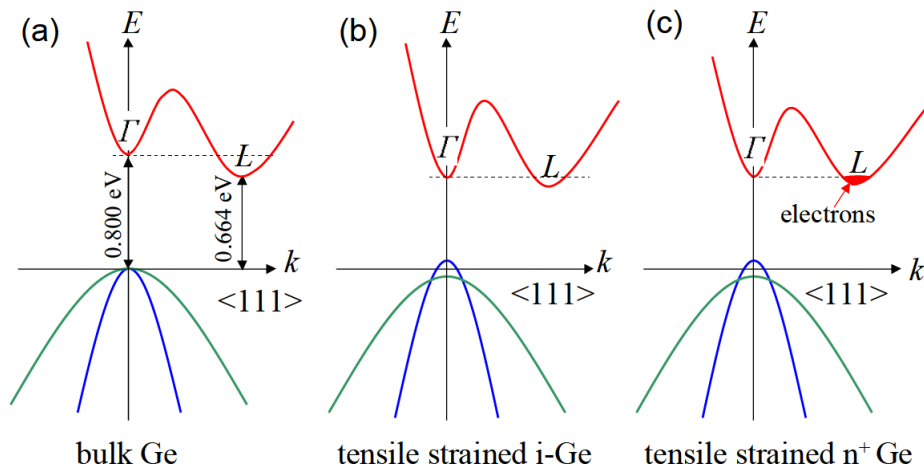


Figure 2.5: Schematic band structure of bulk Ge: a) unstrained material with 136 meV difference between the direct and the indirect gap, b) decreased difference between direct-indirect gap after applied tensile strain, c) compensation of the gap difference by n doping [17].

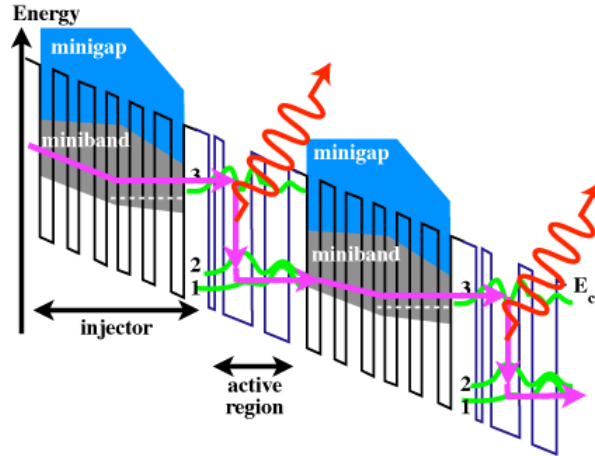


Figure 2.6: Schematic of the gain region of a quantum cascade laser.

2.2.2 Optical Modulator

After photons are generated in a laser, they do not carry any information and must be modulated. Encoding of electrical signal in form of 0s and 1s into the photonic beam takes place in a modulator. The optical structure is realized either as a ring resonator [24] or a Mach-Zehnder interferometer (MZI) [25]. Additionally, a modulator directly integrated into a waveguide was reported recently [26]. The modulation of electromagnetic wave is based on the change of refractive index of the material by applying an external electric field E . One speaks then of electro-optic effect which can be further distinguished into *electro-refraction* or *electro-absorption* when, respectively, real or imaginary part of the refractive index is altered. The basic phenomena governing the electro-optic effect are Pockels, Kerr, Franz-Keldysh, and quantum confined Stark effect (QCSE) [27, 28].

The **Pockels effect**, also known as linear electro-optic phenomenon, is a change in the real part of refractive index proportionally to the external electric field. It is typical only for materials which lack inversion symmetry and is not present in group IV semiconductors. In consequence, the most common optical modulators are produced using LiNbO_3 or III-V materials like GaAs or InP.

The **Kerr effect** is a second order electro-optic effect with the real part of refractive index changing proportionally to a square of external electric field. It is dominant in centrosymmetric materials (e.g. Si or Ge), however, it is much weaker than the linear effect.

An external electric field applied to a semiconductor causes bending of energy bands and the expansion of electron and hole wavefunction into the

bandgap. This enables a tunnelling process assisted by a photon with energy smaller than the energy gap. In consequence, a shift of fundamental absorption edge to longer wavelengths known as the *Franz-Keldysh effect* is observed. In comparison to Pockels and Kerr effects, the Franz-Keldysh effect is based on the change in both real and imaginary part of refractive index. Although Si shows a weak electro-optic effect, a promising candidate to be used as light modulator is Ge. It was reported [29] to show a strong Franz-Keldysh effect which can be further tuned by tensile strain. The strength of refractive index change is comparable to that observed for InP and LiNbO₃. A tensile strained GeSi modulator integrated into a Si waveguide on SOI wafer and exploiting Franz-Keldysh effect was recently demonstrated by Liu et al. [26]. A small amount of Si in Ge caused a shift of absorption edge and enabled an optimal efficiency in the range of 1.55 μm . The footprint and ultra low power consumption was shown to be comparable to Si microring resonators and much smaller than Si MZI. Even smaller active device area was reported by Lim [30]. In his work, a novel Ge electro-absorption modulator of high efficiency was presented.

A phenomena similar to Franz-Keldysh effect is observed in multi quantum wells (MQW). One speaks then of *quantum confined Stark effect* (QCSE). Due to carrier confinement in the structure, the overlap of electron and hole wavefunctions increases. This situation is changed when an external electric field is applied. Electrons and holes are pulled towards opposite sides of each quantum well, the overlap of wavefunctions decreases and lowers the absorption of light. Additional change in energy separation is observed. QCSE effect was demonstrated in Ge quantum wells [31], Si/SiGe [32], and Ge/SiGe [33] superlattices.

2.2.3 Photodetector

The last building block needed to realize the EPIC system is a photodetector. It converts a photonic signal back into electrical impulse at the end of an optical bus. Photodetectors must fulfil such requirements like high sensitivity at operating wavelengths, high response speed, and high signal-to-noise ratio. Much effort was spent to build a Si photodetector. As result, efficient devices were demonstrated to operate in the range of 850 nm [34]. Higher wavelengths are, however, inaccessible for Si. A long-wavelength absorption cut-off established by the band gap of Si (1.12 eV) amounts to approximately 1.1 μm [35]. For wavelengths longer than this value, the light will not be detected due to very small absorption coefficient. In consequence, pure Si photodetectors

are inadequate for light detection in the range of 1.3 - 1.55 μm typical for telecommunication.

The materials that nowadays dominate the market of photodetectors are III-V compounds due to their high absorption efficiency and large drift velocity required for fast response time. However, III-V materials are difficult to integrate with Si CMOS technology and eventually in EPIC systems.

An alternative to III-V compounds is Ge. Due to a small bandgap, Ge offers much higher absorption coefficient than Si in the wavelengths regime typical for telecommunication technologies and can be used as a promising candidate for Si photonics. Many structure types of Ge-based photodetectors were demonstrated over the last years.

Among them, the most commonly used is the *pin diode* operating in reverse bias [36, 37, 38]. A big interest in pin diode is due to the fact that the quantum efficiency and response time can be optimized by adjusting the thickness of depletion region (intrinsic layer) [34]. When light is absorbed, an electron-hole pair is created. The carriers are then separated by a built in electric field inside the junction and contribute to the current flow in the external circuit [35]. Normally, the intrinsic layer is thicker than the doped regions to promote creation of electron-hole pair in the regions where they can be quickly swept out by the electric field. One speaks then of a drift current. A so called diffusion current corresponds to carriers generated outside the depletion layer and diffusing into the reverse biased junction. The diffusion current is, however, undesirable. Due to long response time and carrier recombination on dislocations and point defects, it results in lower collection efficiency than the drift current [39].

Unlike pin diode, a *metal-semiconductor-metal (MSM) photodiode* works in a photoconductive mode which means that the resistivity of the junction changes when it is exposed to light illumination. The diode operates only at non zero bias condition with one of three modes depending on the photon energy $h\nu$ and the applied voltage [35]. If $h\nu$ is smaller than the energy gap of the semiconductor E_g , an electron in the metal can be excited over the metal-semiconductor barrier (Schottky barrier). If $h\nu > E_g$, an electron-hole pair in the semiconductor is created and the device behaves similar to pin photodiode. Additionally, if applied voltage is comparable to the avalanche breakdown voltage, the diode can be operated in the avalanche mode. Although small band gap of Ge leads to higher absorption in the telecommunication wavelengths, it results in a smaller Schottky barrier and large dark current of MSM detec-

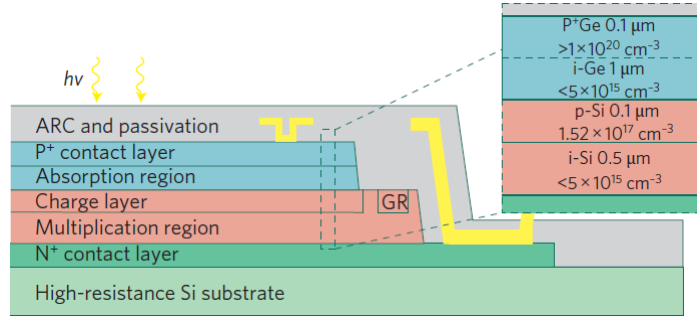


Figure 2.7: Schematic cross-section of a Ge/Si APD consisting of separate absorption (Ge) and multiplication (Si) regions (ARC: anti-reflection coating [43]).

tor [34]. In consequence, the power consumption of Ge MSM photodiode is increased. It was shown that application of dopant segregation technique [40] or asymmetric electrodes [41] can limit the dark current. High performance Ge metal-insulator-semiconductor photodetectors were also demonstrated [15, 42].

When the avalanche multiplication at high reverse bias occurs, a pin or MSM photodiode can be operated as *avalanche photodiode (APD)*. The multiplication leads to a high internal current gain which can be used to detect low power signals. In consequence, the sensitivity of avalanche photodiodes is higher than the sensitivity of normal pin or MSM diodes. A figure of merit for APD is signal-to-noise ratio characterized by a so-called ionization ratio k which is the ratio of the ionization coefficient of one type of carriers to the ionization coefficient of the second type of carriers [35]. For small k , the noise is decreased and the performance of APD is increased [44]. This is the case for Si which shows better multiplication properties than typical III-V compounds [39, 43] but not for Ge. It was shown, however, that high absorption of Ge and efficient carrier multiplication of Si can be combined to create a high performance Ge/Si APD competing with traditional group III-V APD [43]. Additionally, to tailor the quantum efficiency and multiplication gain, a separate absorption-charge-multiplication (SACM) structure can be used [39]. In this case, light absorption and multiplication process occurs, respectively, in Ge and Si [43] (see Fig. 2.7).

2.3 Ge growth techniques

The superior optoelectronic properties of Ge with respect to Si, make this semiconductor a very promising candidate for photonic technologies. However, the

key factor of all applications is the quality of the material. It was reported, that defects in semiconductors interact with charge carriers and should be treated as scattering [45, 46] or recombination centres [47], lowering the performance of any device. In consequence, much effort was dedicated to achieve good crystal quality of Ge on the Si platform. The greatest challenge is the big lattice mismatch of 4.2% which results in a complex Stranski-Krastanov growth mode leading to a) high surface roughness and b) a threading dislocations density (TDD) too high for many applications [39]. We next give a short overview of techniques developed over last years addressed to achieve smooth Ge epilayer with low TDD on Si:

Direct growth on Si(001)

There are two main approaches for depositing Ge epilayer with low TDD on Si(001). One way is to grow Ge directly on Si wafers. In order to suppress the tendency of islanding and provide a thin closed layer with a relatively smooth surface, low temperature growth is realized. In the second step, higher temperature is used and results in higher growth rate and improved TDDs. To lower the TDD further, thermal processing, e.g. cycling annealing, was reported [48, 49, 50]. Rather *thick* ($>1 \mu\text{m}$) Ge layers are needed to achieve $\text{TDD} < 10^7 \text{ cm}^{-2}$.

SiGe buffer

Possibly the most investigated method to achieve Ge with low TDD employs a graded SiGe alloy as a buffer between the epilayer and the Si substrate [51, 52, 53]. By lowering the grading rate, it was possible to limit the rate of dislocation nucleation. Desirable termination of threading dislocations occurs at the interface of each sub-layer to avoid propagation further to the surface. Using the graded SiGe buffer, the thickness of deposited Ge layer can be reduced and ultra-thin (strained) Ge films of high quality can be achieved. However, the trade off for a good quality *thin* Ge film is the extended thickness of the buffer (typically of the order of a few μm), which makes the integration process (e.g. planarization) challenging (see Fig. 2.8).

Several methods to reduce the thickness of SiGe were proposed lately. Ang [9] and Huang [54] presented a very thin ($\ll 1 \mu\text{m}$) low-temperature pseudo-graded SiGe layer. A thin relaxed low temperature Ge buffer growth approach was also presented by Kasper et al. [55, 56]. The relaxation process was triggered by point defects injected near the (Si)Ge/Si interface. Another

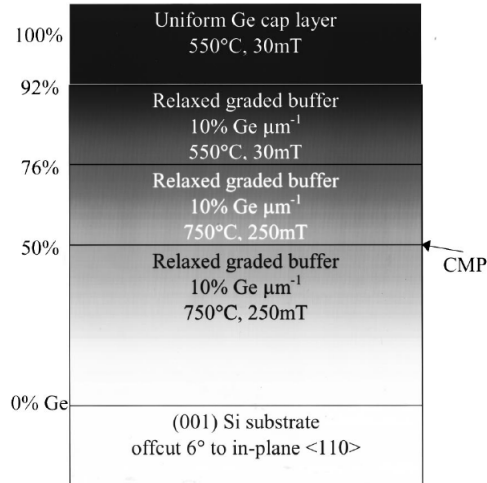


Figure 2.8: Schematic of the structure and growth conditions required for Ge integration on Si(001) via SiGe graded buffer [53].

technique was given by Mantl et al. who used He ion implantation in the Si substrate and subsequent annealing known as the so-called "Jülich process" [57, 58].

Oxide buffer

An alternative to SiGe is the use of an oxide buffer [59, 60]. The rich physics and chemistry of oxide thin films allows to tailor important epi-Ge growth parameters (lattice constant, thermal expansion coefficient, surface energy, strain etc.) over a wide range [61, 62]. An advantage is for example given by the fact that the oxide buffer acts also as a diffusion barrier against Si. As result, ultra-pure Ge thin films can be achieved on Si. However, this research approach is rather new and achievable Ge defect densities are still higher than with respect to the classical SiGe buffer approach.

Mesa structures and selective growth

A very promising method to further reduce TDD is to combine the above approaches with the selective growth of Ge for example in mesa windows [63], i.e. small areas defined in a SiO₂ mask on Si(001). By designing appropriate strain field, one may expect stress induced dislocation gliding through the epilayer towards the edge of mesas and exiting the material at the free surface [48, 64, 65]. Growing in mesa areas was applied for example in the aspect ratio trapping (ART) [66, 67, 68, 69] where the arms of dislocations threading

through Ge were stopped at the sidewalls and eventually trapped inside SiO₂ trench.

Moreover it was shown, that melt and regrowth by millisecond laser annealing can remove stacking faults and microtwins and improve the crystalline quality of Ge [70].

2.4 Nanoheteroepitaxy

In this thesis, we evaluate experimentally a novel Ge growth approach on Si, namely the so-called Nanoheteroepitaxy (NHE). The NHE theory was proposed by Zubia [71] and is based on free-standing nanopatterned Si(001) structures acting as nanoseeds for selective Ge growth. This approach is fundamentally different from the use of mesa windows on planar Si(001) [72]. The main advantages of the 3D NHE are best understood by a direct comparison with the classical heteroepitaxy of lattice and thermal mismatched layer on a planar substrate [73].

Fig. 2.9a depicts the case of the classical Ge heteroepitaxy on Si(001) substrate. At the first stage of the growth, the strain energy originating from the lattice mismatch is compensated by the elastic deformation of the epilayer. One speaks then of a pseudomorphic growth: Ge crystal is tetragonally distorted by matching the lateral lattice constant to the one of Si. As result, the stress in Ge is relieved in the vertical direction (process i). However, this mechanism is not efficient enough and as the growth proceeds, the strain energy in the epilayer increases further. In consequence, above a so-called ***critical thickness***, the accumulation of strain energy triggers the formation of defects in form of misfit dislocations at the heterointerface (process iv) whose threading arms (process v) penetrate through the whole layer and limit thus the performance of any device application.

In contrast to a classical planar heteroepitaxy, a free-standing Si nanoisland can elastically relax the mismatch strain by vertical and horizontal deformation of the epilayer and the nanopatterned substrate (process i and ii). Such 3D strain relief provides that the strain energy drops exponentially with increasing distance from the interface. In consequence, as the growth continues, the strain energy saturates. If the maximal value of the strain energy is kept below the level required for nucleation of misfit dislocations, a defect-free Ge of infinite thickness can in principle be grown on Si(001). Provided that the lateral dimensions of the nanoisland are small enough, the strain energy in

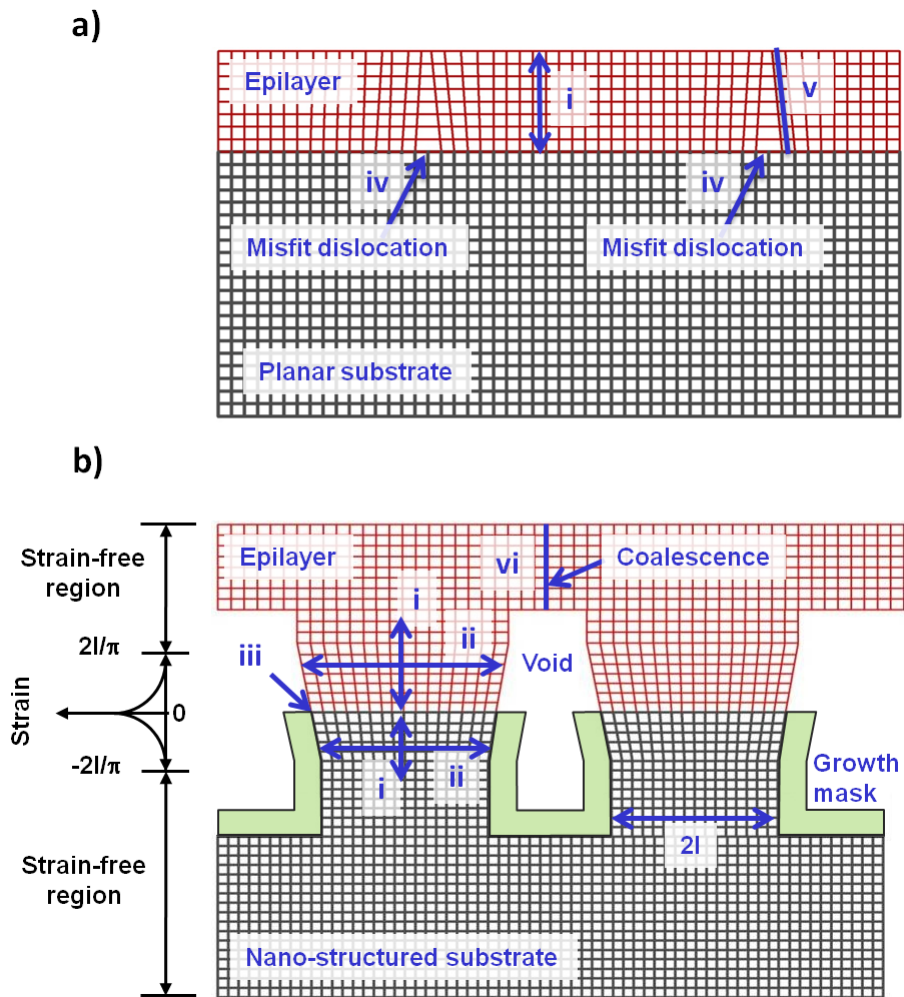


Figure 2.9: Classical planar heteroepitaxy (a) and 3D nanoheteroepitaxy (b) [74].

Ge can be further lowered by the partitioning of the strain energy between the epilayer and the substrate. One speaks then of a **compliant substrate**. Furthermore, due to the reduced dimensions of the Si-nanoisland, similar to the growth in mesa windows, defects can glide through the Ge layer and exit the material when the heterointerfaces are appropriately oriented (process iii). In comparison, processes (ii) and (iii) have only a very limited effectiveness in case of planar systems.

A crucial stage of the nanoheteroepitaxy approach is the transition from vertical towards lateral growth. After fully relaxed Ge seed structures on the Si nanoislands are realized, epitaxial lateral overgrowth (ELO) techniques must be applied to form a defect-free closed Ge layer. The coalescence (process vi) must be carefully controlled so that the thin film formation does not become the source of defect nucleation (lattice tilts in ELO wings etc). It is noted, that compliant substrate effects of the Ge/Si heterosystem are in the focus of this thesis and the coalescence of Ge nanoclusters followed by the formation of a closed layer is beyond the scope of the work presented here.

Next, a quantitative description on the level of strain energy in the epilayer on planar and patterned substrates is discussed.

Calculation of strain energy

Fig. 2.10 shows the strain energy in Ge thin films on Si(001) versus film thickness for various heteroepitaxy approaches. As a barrier for defect formation, the defect nucleation energy E_D of a screw dislocation is included, as the latter is in diamond lattices like Si and Ge lower in energy than true edge dislocations [75]:

$$E_D = \frac{Yb^2}{4\pi(1-\nu)w_D} \ln\left(\frac{R}{b}\right) \quad (2.1)$$

where Y denotes the Young modulus, b the Burger vector, ν the Poisson ratio, w_D the effective width of an isolated dislocation and R the distance towards the next free surface. The strain energy E_{class} in case of the classical, planar Ge integration approach on Si(001) is included in Fig. 2.10 and follows the relationship

$$E_{class} = \frac{Y}{1-\nu} \varepsilon_T^2 h_{epi} \quad (2.2)$$

where h_{epi} labels the Ge thickness and $\varepsilon_T = 2|a_{epi} - a_{sub}| / (a_{epi} + a_{sub})$ the lattice mismatch. It is seen in Fig. 2.10 that the strain energy E_{class} ($h_{sub} = 450 \mu\text{m}$) in case of a Si(001) substrate thickness h_{sub} of 450 micrometer is always bigger than the defect nucleation energy E_D . In other words, the Ge thin film is

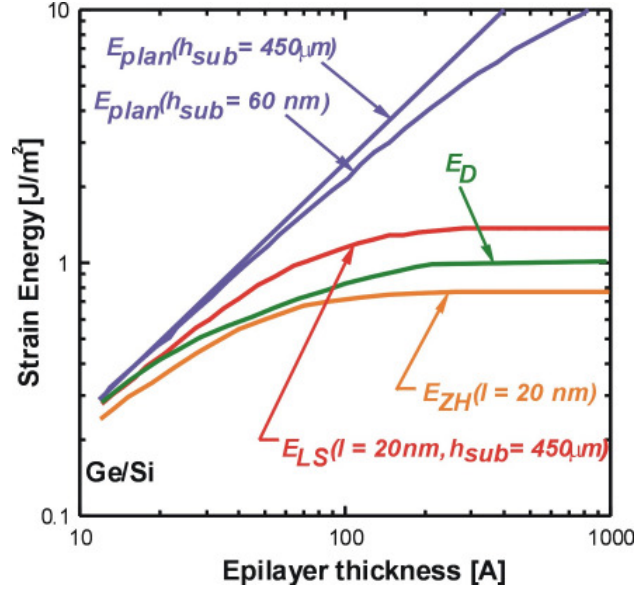


Figure 2.10: Strain energy of different Ge thin film heteroepitaxy approaches on classical planar (E_{class}) and patterned (E_{LS} and E_{ZH}) Si(001) wafers [71].

expected to plastically relax by screw defect nucleation. It is seen in Fig. 2.10 that the same also holds for the strain energy E_{class} ($h_{sub} = 60$ nm) in case of a compliant planar Si(001) substrate, even if the thickness is unrealistic thin ($h_{sub} = 60$ nm) [76]. The "nature" of a compliant substrate is best described by the following equation:

$$E_{compl} = \frac{Y_{epi}}{1 - \nu_{epi}} \varepsilon_{epi}^2 h_{epi} + \frac{Y_{sub}}{1 - \nu_{sub}} \varepsilon_{sub}^2 h_{sub} \quad (2.3)$$

It is clearly seen that the strain energy is distributed between the epilayer and the substrate. In other words: ε_{epi} and ε_{sub} are smaller than the maximum value ε_T for a rigid substrate. In case of a compliant substrate, the degree of strain distribution between the film and the substrate is given by the respective materials parameters, best described by the "compliance parameter" [77]:

$$K = \frac{Y_{epi}}{1 - \nu_{epi}} \frac{1 - \nu_{sub}}{Y_{sub}} \quad (2.4)$$

The consequence of this type of "lever rule" is: The bigger the K value, the higher the strain adsorption by the substrate. For example, Fig. 2.10 shows in case of E_{class} ($h_{sub} = 60$ nm) that the compliant character of the 60 nm thick Si(001) wafer increases with Ge film thickness but does not change the central relationship between strain energy on the one hand and defect nucleation on the other hand. The approach of such thin template was used by Powell et

al. [78] who presented a relaxed SiGe layer with 15% Ge deposited on ultra thin silicon-on-insulator (SOI) substrate. The epilayer relaxation, although achieved by nucleation of misfit dislocations at the SiGe/Si interface, occurred without the injection of dislocations into SiGe material. Furthermore, threading dislocation segments were found in the thin underlying Si cap. This was possible by growing SiGe layer thicker than the Si cap without exceeding the critical thickness and was followed by a strain transfer from SiGe towards Si. The biggest limitation of this approach is the requirement of thinner Si caps as the mismatch towards the epilayer increases. For example, SiGe with 50% Ge content would require 10 nm thick Si cap. The challenge of preparing a homogeneous few nanometres thick Si template layer makes this technique not feasible for such material like pure Ge.

In 1986, Luryi and Suhir (LS model) published a central work on nano-heteroepitaxy on 3D nano-patterned Si(001) wafers for the integration of lattice matched semiconductors [79]. The central idea is to make use of 3D strain relieving mechanisms to limit strain accumulation in the growing epilayer. Fig. 2.10 demonstrates in form of the E_{LS} curve the substantial decrease of the strain energy in Ge growth on 3D nano-patterned Si(001), using a feature size of $2l = 40$ nm. However, it was not possible to lower E_{LS} below E_D . Please note that the saturation of E_D beyond a Ge thickness of 20 nm is given by the fact that the distance R to the next free surface in Eq. 2.1 is not any longer given by the film thickness but by the feature size of the 3D nanostructure (phenomenon of 3D nano-heteroepitaxy). Zubia and Hersee developed in 1999 the LS model further by including also compliant substrate effects (ZH model) [71]. Analytically similar to Eq. 2.3, the ZH model is described by:

$$E_{ZH} = \frac{Y_{epi}}{1 - \nu_{epi}} \varepsilon_{epi0}^2 h_{epi}^{eff} + \frac{Y_{sub}}{1 - \nu_{sub}} \varepsilon_{sub0}^2 h_{sub}^{eff} \quad (2.5)$$

However, important differences are introduced: The terms ε_0 describe, for the substrate as well as the epilayer, the strain directly at the heterointerface which decreases in magnitude with increasing distance from the Ge/Si boundary. The effective thicknesses h_{eff} of substrate and epilayer exactly describe these parts of the material, over which the strain energy decays. The ZH model is presented in Fig. 2.10 by the curve E_{ZH} for Ge on Si(001), making use again of 3D nanostructures with a feature size of $2l = 40$ nm: The main result is given by the fact that, due to the activation of 3D strain relaxation and compliant substrate mechanism, the strain energy E_{ZH} for all film thicknesses stays below the energy E_D triggering the nucleation of screw dislocation. In consequence,

the ZH model offers the vision to grow defect-free Ge heterostructures on Si(001) of unlimited thickness by making use of the 3D nanoheteroepitaxy approach.

An important conclusion can be drawn by simplifying Eq. 2.5. Assuming that the materials constants Y and ν of epilayer and substrate are similar, the lattice mismatch is distributed in an equal way: $\varepsilon_{sub} = \varepsilon_{epi} = \varepsilon_T/2$. Given the fact that the effective thickness h_{eff} in substrate and epilayer over which the strain decays are mainly determined by the effectiveness of the 3D relaxation mechanisms, it becomes obvious that h_{eff} crucially depends on the lateral feature size $2l$ of the Si nanostructure template. A quantitative evaluation shows that h_{eff} can be approximately expressed by l/π . In consequence, Eq. 2.5 can be simplified to a form which is very similar to Eq. 2.2 of the classical planar heteroepitaxy approach:

$$E_{ZH} = \frac{Y}{1-\nu} \varepsilon_T^2 \frac{l}{2\pi} \quad (2.6)$$

In general, it can be concluded from a comparison of the Eq. 2.2 and 2.6: The feature size of the 3D nanopatterned Si wafer must strongly decrease with increasing lattice mismatch ε_T between the substrate and the epilayer. Typically, calculations show that the critical feature size of the 3D nanostructure l_c is about 15 to 30 times bigger than the critical film thickness h_c in case of planar heteroepitaxy approaches. For the Ge/Si(001) system with the lattice mismatch of 4.2% and critical film thicknesses of less than 3 nm, it can be estimated that 3D nanoheteroepitaxy feature sizes l of 20 to 100 nm are required.

Such nanocontact heteroepitaxy was also used in the epitaxial lateral overgrowth (ELO) with rapid melting growth [80, 81, 82, 83] or in the epitaxial III-V (InP, GaP, GaAs or InAs) nanowires formation on Si [84, 85, 86]. Despite similarities between those approaches and the here presented NHE

- crystal dimensions small enough to allow effective dislocations gliding through the material and exiting at free surfaces,
- separation of neighbouring crystals to prevent the formation of interface defects during coalescence (e.g. anti-phase domain in III-V alloys on group IV semiconductor heteroepitaxy),
- efficient 3D strain relief mechanism to reduce strain energies,

a conceptual difference of NHE lies in the compliant substrate effects and the suppression of defects formation by the strain partitioning phenomenon. It is

important to realize, that the experimental verification of compliant substrate effects requires sophisticated characterization techniques. The main limitation corresponds to the simultaneous detection of two effects:

- the strain partitioning phenomenon between the Ge epilayer and the nanopatterned Si substrate,
- the absence of plastic relaxation by nucleation of defects.

2.5 Defect physics

As already mentioned, beyond the so-called critical thickness, the strain accumulated in the epilayer due to lattice and thermal mismatch can be partially released by nucleation of misfit dislocations. Associated with them are threading dislocations running through the whole epi-film.

In this chapter, the basics of defect physics in diamond lattices (Si, Ge) are introduced. The knowledge about their nature is crucial to develop defect reduction approaches since defects lower the performance of photonic devices. Additionally, it is required for understanding the method of defects filtering by using a small growth area described at the end of this section.

2.5.1 Dislocation types

Dislocations are linear defects along which the interatomic bonds are disrupted. They are characterized by a line vector, the Burgers vector, and glide plane [87]. The line vector l is a vector along the dislocation. The Burgers vector b is determined by a Burger circuit procedure. The angle between b and l determines the type of a dislocation. If b is perpendicular to l , one speaks of an edge dislocation (see Fig. 2.11a). The edge dislocations are often called 90° dislocations. If b and l are parallel or antiparallel, a screw or 0° dislocation is formed (see Fig.2.11b). Although pure edge and screw dislocations are observed in real crystals, the most common are dislocations of mixed character like the one shown in Fig.2.11c.

The Burgers vector indicates both the direction and the amount of slip that was used to create the dislocation. If an external stress is applied to the crystal, the dislocation will slip (glide) in the direction of the b vector. The slip plane is defined by the Burgers vector and the line vector.

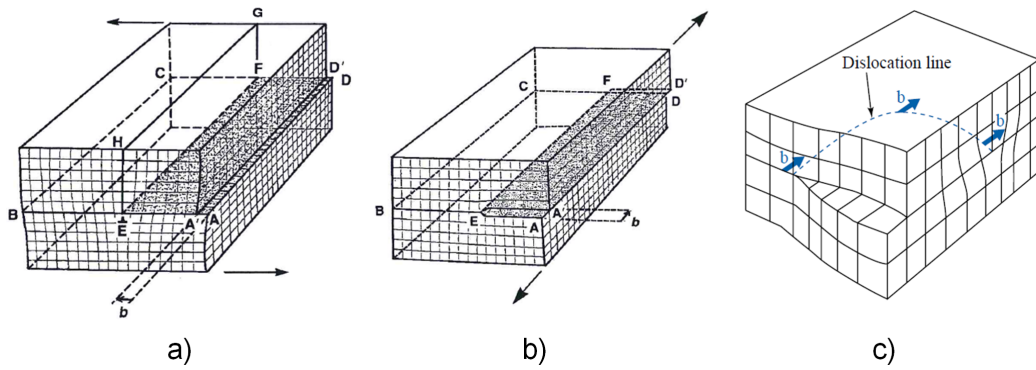


Figure 2.11: Dislocation types: a) edge, b) screw, c) mixed [88].

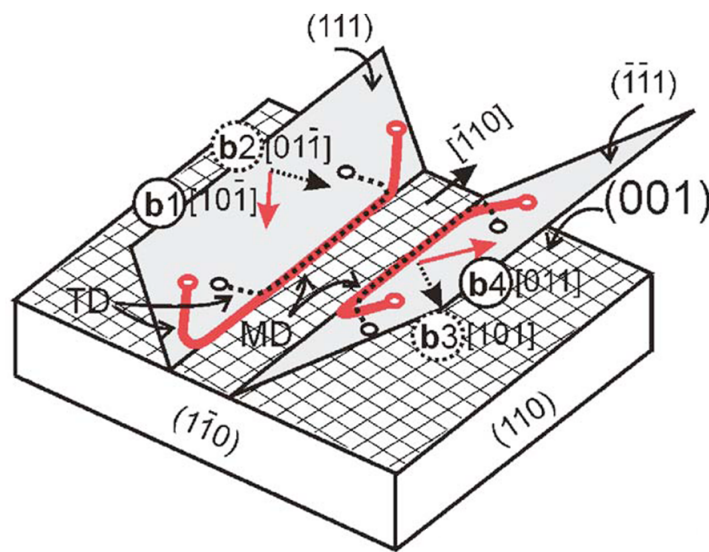


Figure 2.12: Schematic illustration of eight slip systems of 60° misfit dislocations in Ge(SiGe)/Si(001) system [91].

Dislocations in diamond crystal

Typical dislocations in diamond structures (Si, Ge) are 90° dislocations and 60° dislocations (the angle between b and l amounts to 60°) with partially edge and screw nature.

The Burgers vector of misfit dislocations in (001) heteroepitaxy are often of type $\frac{a}{2} \langle 110 \rangle$ with the slip plane corresponding usually to $\{111\}$ planes (Fig. 2.12). As result, misfit dislocations in Ge(SiGe)/Si(001) system are created along two perpendicular $\langle 110 \rangle$ directions in the plane view of the epilayer (Fig. 2.13). One speaks then of the cross-hatch pattern [89, 90].



Figure 2.13: Plane view TEM micrograph of 20-nm-thick Ge/Si(001) with the cross hatch pattern [90].

2.5.2 Dislocation motion

There are two main approaches to limit the amount of threading dislocations (TD) in the epilayer. One way is to filter them out by blocking from further propagation (and multiplication) towards the surface of the crystal. This approach was presented already in section 2.3 where threading arms in Ge are blocked on the sidewalls of deep trenches in the SiO₂ mask (aspect ratio trapping). The other way to remove TDs is to apply external stress which results in a dislocation movement.

The source of applied stress does work on the crystal and the dislocation behaves as if it was subjected to a force equal to the work performed on a moved distance. The force acting on a dislocation is given by the so-called Peach-Koehler formula [92]:

$$F/L = (\sigma \cdot b) \times s \quad (2.7)$$

where F/L is a vector force per unit length, σ is an arbitrary stress tensor, b is the Burgers vector, and s is a unit vector in the direction of the line vector. In the scalar form Eq. 2.7 is written as:

$$F = \tau b. \quad (2.8)$$

Here, τ is the shear stress on the slip plane in the slip direction and b is the length of Burgers vector.

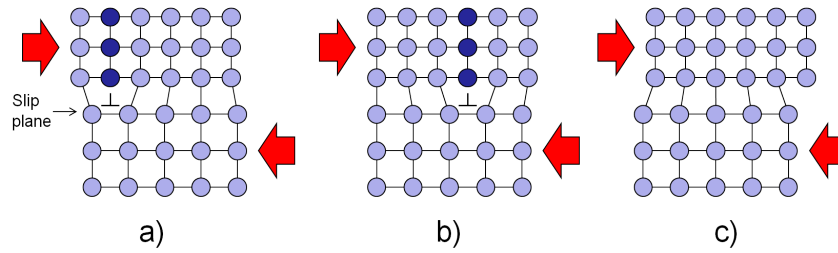


Figure 2.14: Glide of an edge dislocation in the slip plane under externally applied shear stress (a, b). Creation of a step from the extra half plane (c).

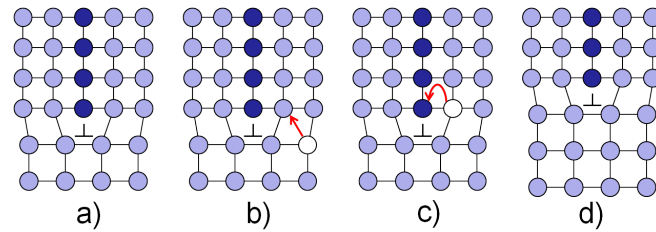


Figure 2.15: Climb movement: a) crystal with an edge dislocation, b,c) migration of a vacancy towards dislocation core, d) shift of the edge dislocation by one atomic distance.

There are two types of dislocation motion, glide and climb. Glide is a conservative movement in the direction of the Burgers vector and occurs at relatively low temperatures. As an example, in Fig. 2.14 a glide of an edge dislocation is depicted. Under external shear stress, the rearrangement of atoms close to the dislocation moves it towards the edge of the crystal until it finally exits the material. In contrast to glide, climb is a non-conservative motion which occurs out of the glide plane and involves creation and migration of point defects like vacancies (see Fig. 2.15). It is temperature activated and occurs mainly at higher temperatures.

2.5.3 Defect sources

Defect injection in a perfect epilayer requires an infinite activation energy. In the real material, this energy is lowered by inhomogeneities. In consequence, nucleation of misfit dislocation can be triggered by: fixed sources inherited from the substrate and surface imperfections of the epilayer or the substrate schematically depicted in Fig.2.16. Interaction and multiplication processes can be responsible for additional increase of the dislocation density.

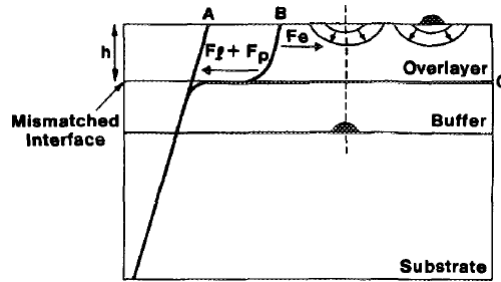


Figure 2.16: Defect sources: fixed sources (left), heterogeneous surface half loop (middle), homogeneous surface half loop (right) [72].

Substrate defect and surface inhomogeneities

Fixed sources are sources that have a constant density per unit area. They originate from substrate imperfections and can propagate through the epilayer as threading dislocations. As discussed in the previous paragraph, if experienced to a force, such threading arm can move away from its nucleation center and create a long misfit dislocation at the interface.

The nucleation of surface half loop is triggered by inhomogeneities on the surface of the epilayer or the substrate. One speaks then of homogeneous or heterogeneous surface half loop nucleation, respectively. The energy required for nucleation of the half loop is lowered by local changes in the strain field around the imperfection. The process is analogue to the phase change triggered by nucleation germs. One can define a critical radius R_c beyond which the half loop is stable. It continues growing until it reaches the interface between the epilayer and the substrate. In consequence, a misfit dislocation is created with two threading arms which are mobile under applied stress. Loops with radius smaller than R_c will shrink and eventually vanish. A detailed analysis of the nucleation of half-loops was given by Matthews [73, 93].

Defects interaction

Nucleation of dislocations causes a perturbation of the stress field in the vicinity of a dislocation. The interaction between dislocations involves a superposition of those stress fields and can result in one of two cases.

- If the combined stress field is smaller than the stress field of a single dislocation, the energy of the configuration decreases and the dislocations attract each other. It is the case for two regions of overlapping compressive (tensile) strain.

- If the combined stress field is bigger than the stress field of a separate dislocation, the energy of the configuration increases and the dislocations repel each other. This process is typical for the region of compressive (tensile) strain overlapping with the region of tensile (compressive) strain.

In general, two parallel dislocations on the same glide plane, will repel each other provided that their Burgers vectors are parallel. In consequence, a group of misfit dislocations with the same Burgers vector may prevent dislocations from gliding to the edge of the crystal [72]. If the Burgers vectors of two parallel dislocations on the same glide plane are antiparallel, the dislocations attract each other. The situation becomes more complicated when two dislocations occupy neighbouring glide planes. In this case, dependent on the dislocation position regions of attraction and repulsion can be defined.

Provided that two dislocations attract each other, an additional dislocation reaction may be triggered with a subsequent creation of a single dislocation. It does not necessary occur on the whole length of the dislocations which results in a node formation.

There are two conditions that must be fulfilled for a dislocation reaction to occur: the Burgers vectors must be conserved and the process must be energetically favourable. Interestingly, a reaction of two dislocations with opposite Burgers vectors leads to annihilation of both dislocations.

In diamond (Si, Ge) and zinc blende structure, two 60° dislocations with line vector $[110]$ can react and create a single edge dislocation according to [87]:

$$\frac{a}{2} [101] + \frac{a}{2} [0\bar{1}\bar{1}] \rightarrow \frac{a}{2} [1\bar{1}0] \quad (2.9)$$

Although the resulting edge dislocation decreases by a half the density of threading dislocations, it is immobile and has a small probability of exiting the crystal. It is thus a permanent threading dislocation [72].

Another example of the interaction phenomena is the attraction of point defects to dislocation. Local changes in the strain field around a dislocation lead to the migration of impurity atoms. Depending on their size with respect to the host atom, impurities migrate either to region of tensile or compressive strain. This attraction results in the formation of impurities cluster around dislocation lines known as the *Cottrell cloud* or the *Cottrell atmosphere* [94]. Since this segregation lowers the energy of the system, the dislocation is in consequence pinned and its further movement is hindered.

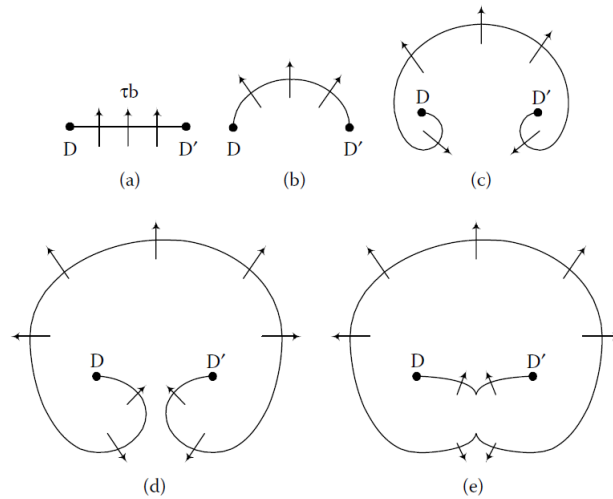


Figure 2.17: The Frank-Read source [87].

Dislocation multiplication

The last most important source of threading dislocations are dislocation multiplication processes. The TEM studies on epitaxial GaAs showed, that multiplication phenomena are responsible for creation of more threading dislocation than fixed sources alone [95].

Possible mechanisms of dislocation multiplications are Frank-Read source, spiral source or Hagen-Strunk multiplication.

The Frank-Read source [96] is depicted schematically in Fig. 2.17 and was observed experimentally in Si wafer (Fig. 2.18). Under applied shear stress, a dislocation pinned to two points (D and D') in the glide plane starts expanding and bends. After a certain time, such a bowed dislocation closes itself and the created loop expands further. The dislocation section pinned between the two points comes back to the initial configuration and the whole process starts again. In consequence, Frank-Read source keeps producing loops as long as the necessary shear stress is applied.

Spiral source operates similarly to Frank-Read source. In this case however, the dislocation is pinned only to one point [96]. The spiral source was demonstrated experimentally in Si [98] and proposed in heteroepitaxial films [99].

The Hagen-Strunk multiplication [100], on the other hand, involves interaction of two intersecting dislocations rather than pinning of a single dislocation. However, its experimental evidence is very limited.

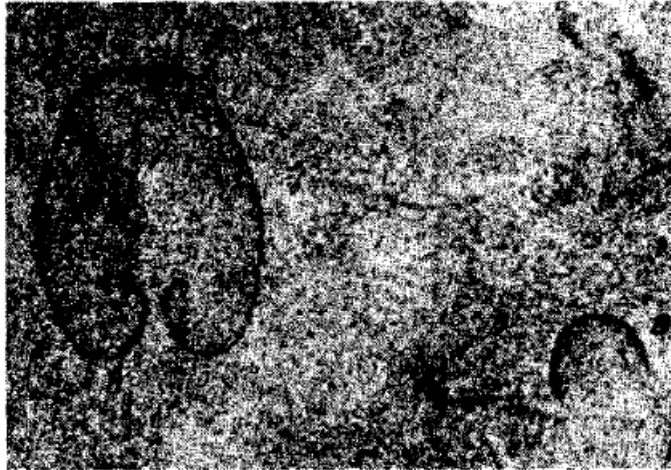


Figure 2.18: $[2\bar{2}0]$ X-ray topograph of sawed and chemically polished Si wafer with bended Frank-Read source [97].

2.5.4 Defects filtering by reduced growth area

Fitzgerald et al. reported a theoretical investigation of the growth area influence on the quality of heterostructures in terms of misfit and threading dislocation density [72]. In his work, fixed source and interaction together with multiplication processes were assumed as mechanisms of defect nucleation.

The use of large growth areas can be summarized as follows:

1. The amount of fixed sources responsible for threading dislocations in the epilayer is increased as the area of growth.
2. The probability of a threading dislocation to escape the epilayer by gliding is decreased since the distance to an edge of the crystal is bigger.
3. Each fixed source and threading dislocation (when moved) leave a long misfit dislocation which enhances the probability of dislocation interactions and multiplication.
4. A long misfit dislocation releases a big amount of strain energy which is responsible for the gliding of threading arms. In consequence, a certain number of dislocations will be trapped in the epilayer before the strain energy approaches zero (hardening limit).

The consequences presented above are not the case for a small growth area where more threading dislocations will reach the crystal edge and the interaction between dislocations is limited. It was shown [72], that small amount of

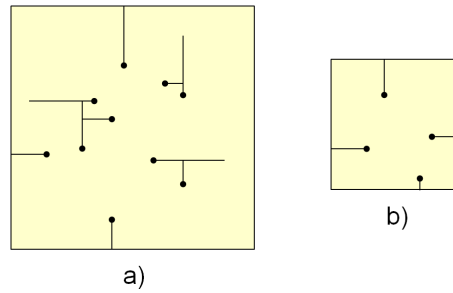


Figure 2.19: Schematic diagram showing the influence of growth area on the defects filtering in the epilayer.

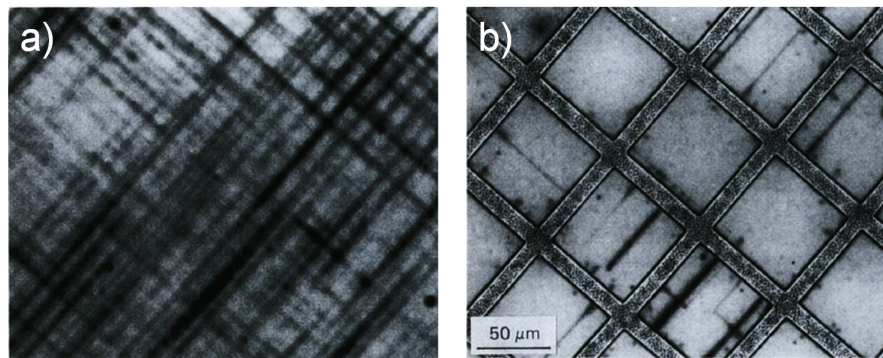


Figure 2.20: EBIC images of a 280 nm thick $\text{Ge}_{0.19}\text{Si}_{0.81}$ layer on unpatterned (a) and $70\ \mu\text{m}$ patterned (b) Si [52].

strain in the epilayer grown on a small area can be used for an efficient filtering of defects. The advantages of small growth area are depicted schematically in Fig. 2.19. As result, in terms of dislocation density, small rather than large growth areas provide a chance to grow epilayer of high quality.

The theoretical investigation of Fitzgerald was confirmed by experimental studies on SiGe/Si heterostructures. Fig. 2.20 presents a plane view electron beam induced current (EBIC) micrograph of $\text{Ge}_{0.19}\text{Si}_{0.81}$ grown on unpatterned and patterned Si substrate. It clearly shows, that the density of misfit dislocation can be essentially reduced by using a small growth area.

Chapter 3

Experimental background

3.1 Sample preparation

In the following section, technological processes used for a) patterning the Si(001) substrate and b) selective Ge deposition will be discussed in detail.

Si nanostructures were realized using photo-lithography and a modified gate spacer process of the IHP 0.13 μm BiCMOS technology schematically shown in Fig. 3.1. After a standard cleaning procedure, Si(001) substrate was covered by SiO_2 and Si rich nitride (SiRN) used as an anti-reflective coating (ARC) for lithography and a hard mask (HM) for etching. After covering by a positive resist and a mask, the wafer was exposed to 248 nm wavelength light of KrF deep-UV Nikon Scanner S207. Line nanostructures were imprinted using a single exposure whereas the island pattern was obtained by an additional exposure through the mask rotated by 90° (Fig. 3.1b). The HM and Si were then etched using dry (plasma) etching (Fig. 3.1c). Next, the sidewalls and bottom trenches of nanostructures were covered by SiO_2 in two steps. The first stage employed a rapid thermal oxidation (RTO) process at 1010°C . As a drawback, a region of unintentionally oxidized Si under the ARC known as the bird's beak was created [101, 102]. The consequence of thermal oxidation is further discussed in the next chapter. In the second step, the whole structure was covered by tetraethyl orthosilicate (TEOS) using chemical vapor deposition (CVD) in 640°C shown in Fig. 3.1d. Si_3N_4 was deposited on top as a protection layer during the plasma etching of the spacer. In some cases, an additional thermal oxidation at 900°C was required to cover the areas of open Si at the bottom of trenches (Fig. 3.1g). In the following, the Si_3N_4 and HM was removed by chemical wet etching and the HF last clean was applied. As the result of the process discussed here, the sidewalls and bottom trenches of

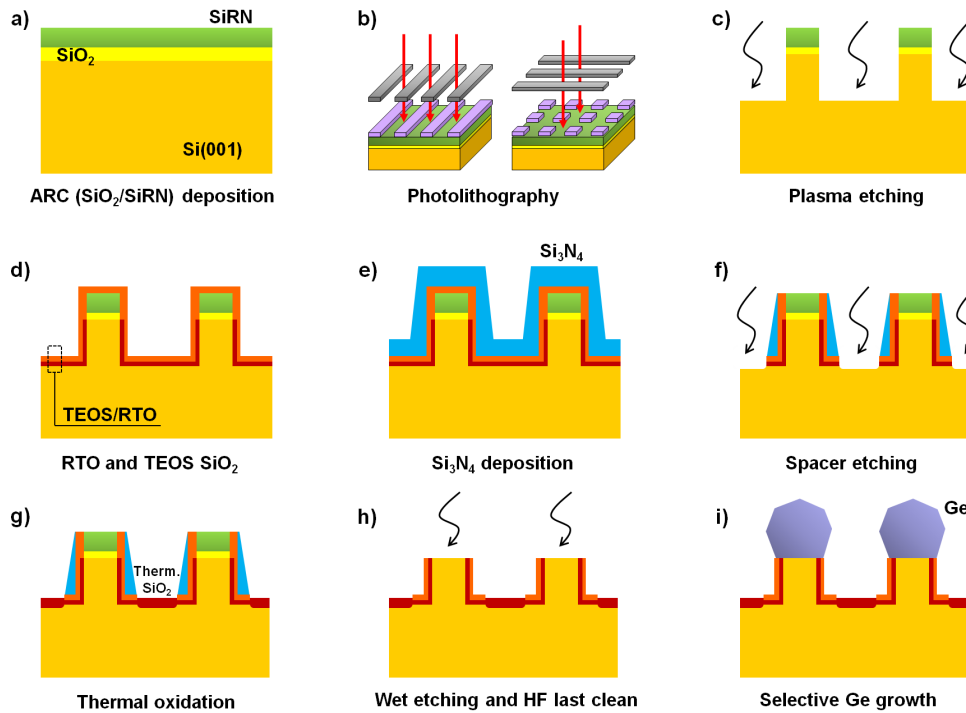


Figure 3.1: Schematic illustration of nanopatterning process used to prepare Si nanostructures for selective Ge deposition.

the Si nanostructure were protected by SiO_2 growth mask whereas the top surface of the Si pattern was uncovered and prepared for selective Ge deposition.

The Ge growth was performed using the single wafer reduced pressure (RP) CVD system. The recipe was optimized for Ge deposition on blanket $\text{Si}(001)$ wafers [50]. In order to remove a thin native SiO_2 layer, after the HF last clean the wafers were baked at 850°C in H_2 atmosphere. Next the Si wafer was cooled down to 600°C , H_2 ambient was substituted by N_2 and the cooling was continued down to 300°C . The initial Ge seed layer was grown using $\text{N}_2\text{-GeH}_4$ gas mixture. This low temperature growth was required to obtain a two-dimensional Ge layer on the Si substrate [103]. Next, the wafer was heated up to 550°C in H_2 and the Ge growth was continued with $\text{H}_2\text{-GeH}_4$ ambient.

3.2 Investigation techniques

3.2.1 X-ray diffraction

X-ray diffraction (XRD) is a non-destructive analytical method used mainly in the analysis of crystallographic structure, chemical composition, and physical properties of a material. XRD is based on the elastic scattering of the electromagnetic wave with the energy in the range of 120 eV to 120 keV by a periodic distribution of electron density. Due to the high energy of the incoming x-ray, its interaction with matter can be described by *Thomson scattering*, i.e. the interaction of light with a free electron. From the classical electromagnetic theory, the oscillating vector of electrical field induces a force acting on the free electron. The charge is accelerated and, as result, radiates with the frequency equal to the frequency of the initial light. Its intensity measured at distance R and under angle ϕ to the incoming light can be written using a so-called Thomson scattering equation [104]:

$$I_e = I_0 \frac{e^4}{m^2 c^4 R^2} \left(\frac{1 + \cos^2 \phi}{2} \right). \quad (3.1)$$

Here, I_0 and $(1 + \cos^2 \phi)/2$ are, respectively, the intensity and the polarization factor of the unpolarized incoming light. It must be noted, that the prefactor $e^4/(m^2 c^4 R^2)$ is of the order of 10^{-26} cm^2 which makes the x-ray scattering process highly inefficient. It is evident that the scattering from an atomic nucleus is at least 10^6 times less efficient than from an electron cloud and can thus be neglected. The intensity I can be increased by using a volume material (more scattering centres). However, in case of thin films and nanostructures, a reliable XRD structure analysis can be offered only by high brilliance synchrotron radiation sources.

Scattering from a crystal

In the previous section, the interaction of an x-ray with a free electron was discussed in detail. Since the interatomic distances are comparable with the wavelength of incoming light, a small crystal exposed to x-rays gives rise to constructive and destructive interference of the scattered wave. In consequence, a diffraction pattern can be observed and further analysed.

In order to properly describe this effect, two additional factors must be taken into account: the *structure factor* F and the *lattice factor* G . At point P , the intensity of x-rays with the wavelength λ scattered from a cubic crystal

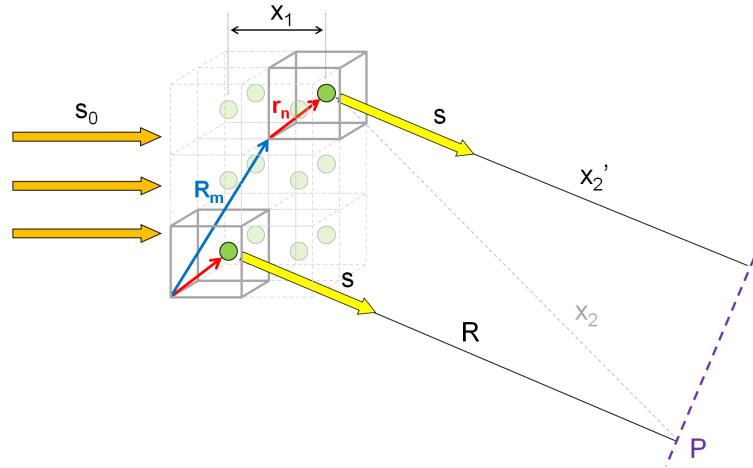


Figure 3.2: Schematic scattering of a parallel x-ray beam on a small crystal. R_m denotes the position of m^{th} unit cell whereas r_n corresponds to the position of n^{th} atom in a unit cell. The crystal is small enough to assume that the primary and the scattered beam are plane waves which leads to $(x_1+x_2) \rightarrow (x_1+x_2')$ [104].

with $N_i a_i (i = 1, 2, 3)$ edges along a_i crystal axes is written as

$$I = I_e F^2 G, \quad (3.2)$$

where

$$F = \sum_n f_n e^{i2\pi/\lambda \cdot (s-s_0)r_n}, \quad (3.3)$$

$$G^2 = \frac{\sin^2(\pi/\lambda \cdot (s-s_0)N_1 a_1/2)}{\pi/\lambda \cdot (s-s_0)a_1/2} \cdot \frac{\sin^2(\pi/\lambda \cdot (s-s_0)N_2 a_2/2)}{\pi/\lambda \cdot (s-s_0)a_2/2} \cdot \frac{\sin^2(\pi/\lambda \cdot (s-s_0)N_3 a_3/2)}{\pi/\lambda \cdot (s-s_0)a_3/2}. \quad (3.4)$$

Here, s_0 and s are the unit vectors defining the propagation direction of initial and scattered beam, respectively. Scattering from a small crystal is shown schematically in Fig. 3.2.

In Eq. 3.3, f_n is the form factor of the n^{th} atom whereas r_n is the position of the n^{th} atom in the unit cell. Thus, the structure factor F corresponds to the atomic arrangement within a unit cell and can be used to determine the type of crystal structure. Since the scattering efficiency is proportional to the sum over all its electrons, XRD provides additionally information about the stoichiometry of the specimen.

From its definition, the lattice factor G corresponds to the periodicity of the crystal. The shape of the observed signal depends strongly on the number

of unit cells N_i (Eq. 3.4). In general, peak height increases and its full width at half maximum decreases for higher N_i . As a result, the lattice factor plays an important role in determining the size and the long range order (e.g. defects presence) within the crystal. Moreover, the intensity of the scattered x-ray is essentially zero except the cases when the three coefficients of G are simultaneously close to their maxima. This condition leads to the selection rules for an XRD signal expressed mathematically in the form of the so-called *Laue equations*:

$$\begin{aligned}\pi/\lambda(s - s_0)a_1 &= h\pi \\ \pi/\lambda(s - s_0)a_2 &= k\pi \\ \pi/\lambda(s - s_0)a_3 &= l\pi \quad ,\end{aligned}\tag{3.5}$$

where h , k , and l are integer numbers. Laue equations are valid in the approximation of kinematical scattering theory which is based on the assumption that an x-ray photon can be scattered only once. A detailed theory of XRD can be found in [104].

XRD experimental setup

All XRD experiments presented here were carried out using synchrotron radiation (SR) at the European Synchrotron Radiation Facility (ESRF) in Grenoble (France) shown in Fig. 3.3.

SR is emitted from electrons travelling at very high speed bent in a magnetic field. First, electrons are fired into a linear particle accelerator (linac). Before entering the main storage ring, their velocity is increased inside a booster (see Fig. 3.3). Bending magnets (BM) provide a circular trajectory of the particles in the storage ring. They are also responsible for the emission of x-rays by electrons alternated in the magnetic field. In straight sections between BMs, additional insertion devices (e.g. undulators, wigglers) can be installed. Insertion devices (IDs) consist of periodic dipole magnets which force a passing electron to oscillate and radiate more efficiently than BMs [106]. X-rays are then directed into a beamline. For the purpose of this work, the ID01 beamline was used during the experiment.

In the beamline, x-rays enter the optics cabin (see Fig. 3.3) which, among the others, contains a double-crystal Si(111) monochromator located between two mirrors to filter and focus the beam. Additionally, the optic hutch provides a constant focal distance during the energy tuning. Next, x-rays are directed

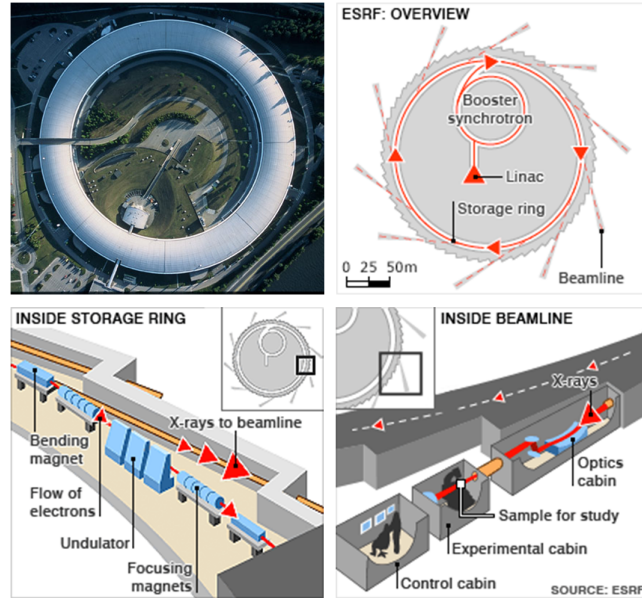


Figure 3.3: Schematic illustration of ESRF: overview, storage ring and beamline [105].

into the experimental hutch with a sample mounted on a diffractometer (see Fig. 3.4). The scattered light is analysed by a detector.

All measurements presented in this work were done with the beam energy of 11 keV in the grazing incident mode. A small incident angle (0.15°) of the incoming x-ray beam enabled an increased sensitivity towards Ge/Si nanostructures and suppression of Si(001) substrate signal [106].

3.2.2 Raman spectroscopy

Raman spectroscopy is a method used to study vibrational states of a material. It is based on inelastic scattering of a monochromatic light known as the Raman effect. It was first predicted by A. Smekal [107] and observed experimentally by K. S. Krishnan and C. V. Raman [108].

The initial energy of light used in Raman spectroscopy $\hbar\omega_0$ is smaller than the separation between electronic states of the investigated specimen (see Fig. 3.5). As result, in contrast to fluorescence, a photon is not fully absorbed and subsequently emitted by a molecule. The Raman effect is based rather on an interaction between the incoming electromagnetic wave and the electron cloud which alters vibrational and rotational states of the material. The molecule is excited to a virtual state of a limited lifetime after which a scattered photon is emitted and analysed. Most photons are scattered elas-



Figure 3.4: 2+4-circle diffractometer + 2 circle analyser stage at ID01 (ESRF) [105].

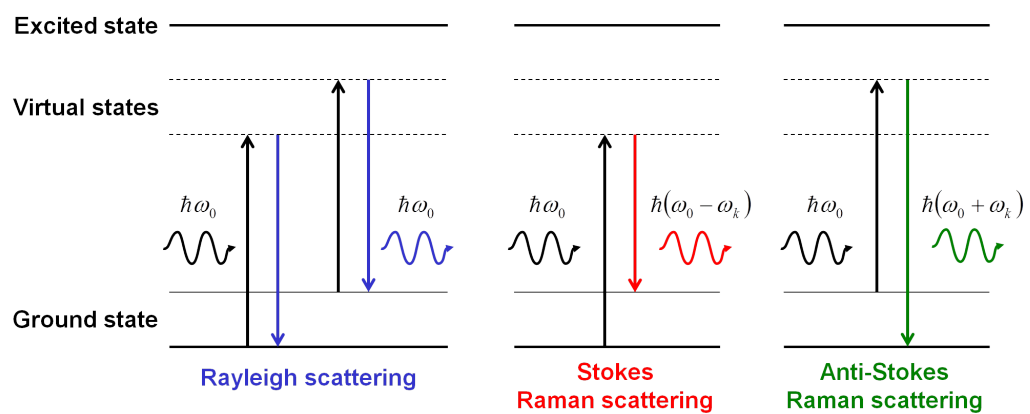


Figure 3.5: The diagram of energy levels involved in the Raman process.

tically by the specimen. One speaks then of a *Rayleigh scattering*. However, approximately 1 out of 10^7 is scattered inelastically and reaches a detector with an energy $\hbar\omega_s$ different than $\hbar\omega_i$. The conservation must hold, thus:

$$\hbar\omega_0 = \hbar\omega_s \pm \hbar\omega_k \quad (3.6)$$

The energy difference $\hbar\omega_k$ gives a direct information about vibrational and rotational states of the molecule. If the scattered photon is emitted with a smaller energy, the molecule will occupy a state energetically higher than the initial state. One speak then of the *Stokes process*. On the other hand, if the scattered photon is emitted with a higher energy, the molecule will finally occupy a state energetically lower than the initial state. This phenomenon is known as the *anti-Stokes process* and can occur only if the molecule is not in its ground state. This fact makes the probability and thus the intensity of anti-Stokes transition strongly temperature dependent. Next, a more detailed description of the interaction between light and matter will be given.

Stokes and anti-Stokes processes

An electromagnetic wave can interact with the material via an oscillating electrical vector E . In consequence, an induced electric dipole moment is created by displacing the electronic cloud of the specimen with respect to its atomic core. The polarization P is defined as

$$P = \epsilon_0 \chi E. \quad (3.7)$$

Here, ϵ_0 is the vacuum permittivity and the proportionality factor χ is the second rank tensor known as the *susceptibility*. It describes the capability of electronic cloud to follow the alternating external electric field:

$$E = E_0 \cos(\omega_0 t). \quad (3.8)$$

The susceptibility modulated by the lattice oscillations can be expanded into the Taylor series around the equilibrium position. If we limit the expansion to the first two terms then

$$\chi = \chi_0 + \sum_k \left(\frac{\partial \chi}{\partial Q_k} \right)_{Q=0} Q_k, \quad (3.9)$$

where χ_0 is the susceptibility tensor without any vibration. The summation in Eq. 3.9 runs over all vibrational modes k defined as

$$Q_k = Q_{k0} \cos(\omega_k t + \phi). \quad (3.10)$$

Putting Eq. 3.7-3.10 together and after some basic trigonometry one gets

$$\begin{aligned}
P &= \chi_0 E_0 \cos(\omega_0 t) \\
&+ \frac{1}{2} \left(\frac{\partial \chi}{\partial Q_k} \right)_0 Q_{k0} E_0 \cos((\omega_0 - \omega_k)t + \phi) \\
&+ \frac{1}{2} \left(\frac{\partial \chi}{\partial Q_k} \right)_0 Q_{k0} E_0 \cos((\omega_0 + \omega_k)t + \phi). \tag{3.11}
\end{aligned}$$

Thus, the oscillating electric field induces a dipole moment oscillating at three different frequencies and, in consequence, giving rise to three different photons. The first term in Eq. 3.11 corresponds to a photon scattered elastically (Rayleigh process) with the unchanged energy $\hbar\omega_0$. Next two terms describe the Raman effect: the energy of the scattered photon is different by the energy of the vibrational mode k and amounts to $(\omega_0 - \omega_k)\hbar$ and $(\omega_0 + \omega_k)\hbar$ for Stokes and anti-Stokes process, respectively.

Not all vibrations give rise to the Raman scattering. The selection rule for the Raman effect is given by the pre-factor $\left(\frac{\partial \chi}{\partial Q_k} \right)_{Q=0}$ often referred to as the Raman tensor R : a vibration is Raman active provided that it alters the susceptibility of the material. The scattering efficiency can be expressed as

$$I \sim \sum_k |e_i R_k e_s|^2, \tag{3.12}$$

where e_i and e_s are the unit polarization vectors of, respectively, incident and scattered light. The form of the Raman tensor R depends on the crystal structure and was given by Loudon [109]. For cubic crystal of Si or Ge, there are three Raman tensors corresponding to two transverse optic modes (TO) polarized along x and y axis and one longitudinal optic (LO) mode polarized along z axis. In Cartesian coordinate system, they can be written as

$$\begin{aligned}
\mathbf{R}_{\text{TOx}} &= \begin{pmatrix} 0 & 0 & 0 \\ 0 & 0 & d \\ 0 & d & 0 \end{pmatrix}, & \mathbf{R}_{\text{TOy}} &= \begin{pmatrix} 0 & 0 & d \\ 0 & 0 & 0 \\ d & 0 & 0 \end{pmatrix}, \\
\mathbf{R}_{\text{LOz}} &= \begin{pmatrix} 0 & d & 0 \\ d & 0 & 0 \\ 0 & 0 & 0 \end{pmatrix} \tag{3.13}
\end{aligned}$$

The form of the Raman tensor together with the scattering geometry (allowed polarization vectors e) defines whether a mode can be detected or not. More comprehensive description of Raman effect and Raman spectroscopy can be found in [110] or [111].

Raman experimental setup

All Raman measurements were carried out on an InVia Raman spectrometer provided by Renishaw. Its schematic illustration is shown in Fig. 3.6. The laser beam was created by one of the three lasers: 364 nm Ar ion laser, 457/488/514 nm triple Ar laser, and 633 nm He-Ne laser. Next, it was directed into the spectrometer, broadened by a beam expander and shined on the sample via a Leica microscope. Various objectives with x100, x50, x20, and x5 magnification were used for visible light. The respective values of the numerical aperture (NA) amount to 0.85, 0.75, 0.4, and 0.12. A special x100 objective with NA of 0.9 was used for the ultraviolet light (364 nm). The light scattered from the sample was directed back to the objective. This experimental setup is known as a so-called micro-Raman in backscattering geometry. The Rayleigh light was filtered out. Next, the beam was collimated and diffracted on a grating. Gratings with 3600, 2400, and 1800 lines per millimetre were used for, respectively, 364, 514, and 633 nm laser wavelength. Finally, scattered light was focused on a Si CCD camera and recorded.

It is noted, that the used backscattering geometry tightens Raman selection rules discussed in the previous section by implying only certain directions of initial and scattered vectors of electric field e . In particular, the investigation of (001) substrates using the setup described here provides information only about one, i.e. LO, phonon mode. In practice, TO modes give a small contribution when using high NA objectives.

3.2.3 Transmission Electron Microscopy

Transmission electron microscopy (TEM) is one of the basic microscopy techniques. It uses electrons transmitted through a specimen and interacting with it to provide information about morphology, crystal structure, defects, and composition of the material. Since electrons have a small de Broglie wavelength, TEM offers much higher spatial resolution than classical light microscopy and is nowadays capable to distinguish objects as small as a few Angstroms. A trade-off for this powerful technique is the time consuming and destructive preparation of very thin (~ 100 nm thick) samples.

Background

The source of electrons in a transmission electron microscope is an electron gun (e.g. tungsten filament) which produces a monochromatic electron beam with

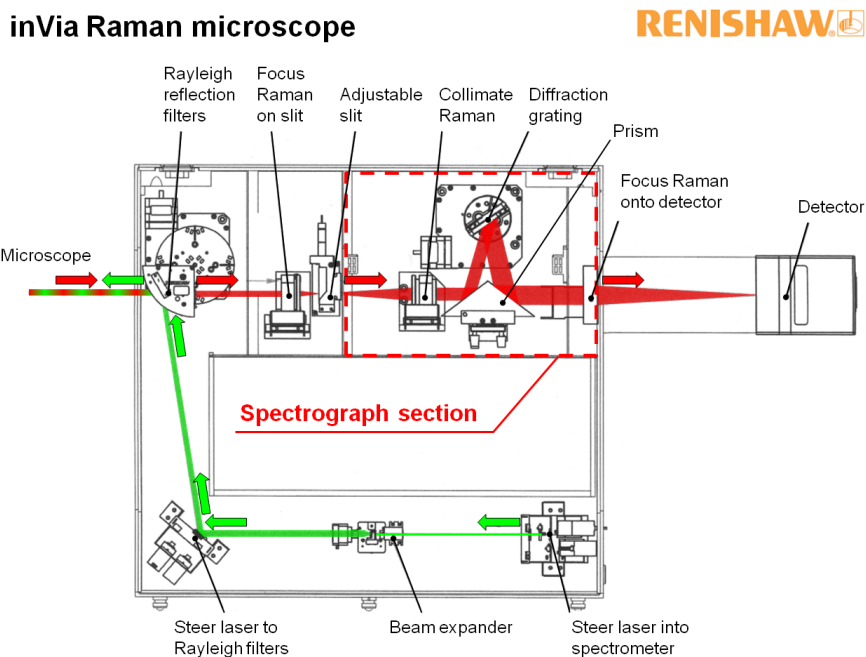


Figure 3.6: Schematic illustration of inVia Renishaw Raman spectrometer.

energy in the range from 20 to 300 keV. This beam is next tuned and focused by a series of magnetic lenses onto the sample. The electrons exiting the material are either backward or forward scattered (see Fig. 3.7). The first group consists of e.g. secondary electrons used in scanning electron microscopy (SEM) or Auger electrons employed in Auger spectroscopy. The forward scattered beam is made of electrons which are not scattered, or are scattered inelastically or elastically. The first group consists of electrons that did not interact with the specimen. Their transmission decreases as the sample thickness increases. As a result, thicker regions correspond to darker images whereas thinner regions correspond to brighter images. Similar rule holds for materials of different density. Inelastically scattered electrons can be investigated by so-called electron energy loss spectroscopy (EELS). In consequence of inelastic processes, additional x-rays are emitted and can be used in energy-dispersive x-ray spectroscopy (EDX). The elastically scattered electrons conserve their energy and momentum and give rise to the contrast in TEM images. Provided that the specimen is crystalline, those electrons are diffracted by the crystal lattice and form, similar to XRD, a diffraction pattern used further to analyse the material structure.

A comprehensive description of the TEM technique can be found for example in [112].

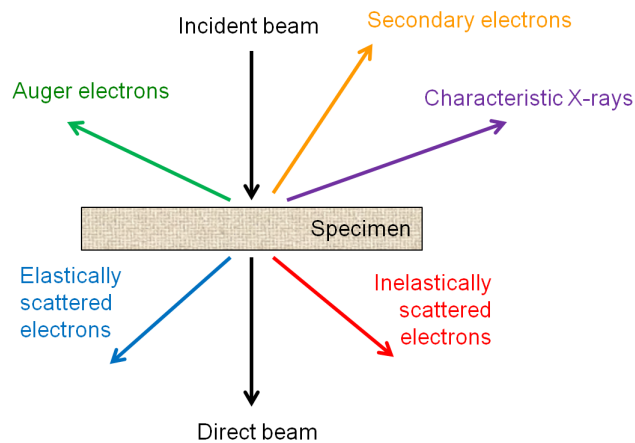


Figure 3.7: Signals originating from a specimen exposed to a high energy electron beam (after [112]).

TEM experimental setup

The TEM investigations were carried out mainly on a FEI Tecnai Osiris microscope shown in Fig. 3.8. In some cases, also a Philips CM200 transmission electron microscope was used. In both systems, electrons are emitted from a Schottky field emission gun operating at high temperatures in ultra-high vacuum conditions. Point resolution at the maximum applicable voltage of 200 kV amounts to 0.26 and 0.27 nm for Tecnai Osiris and CM200, respectively. Both microscopes are equipped with bright and dark field detectors which are used to retrieve various crystallographic information. In addition, Tecnai Osiris consists of high angle annular dark field (HAADF) detector which provides a material contrast.

3.2.4 Finite Element Method

Finite element method (FEM) is nowadays one of the most common numerical technique addressed to find approximate solutions for engineering problems. It is used in fields where the exact solution cannot be obtained or would require much resources in terms of time and calculation power. Efficient and easy-to-use parametrization of various regions of complex geometry and properties expands the application of FEM further to physical problems. The development of the method is tightly bound to computer science. From its development in the 40's by R. Courant [113] until 70's, finite element analysis (FEA) was mostly limited to mainframe computers. However, a dramatic drop in prices together with a boost of computer performance increased the applicability of

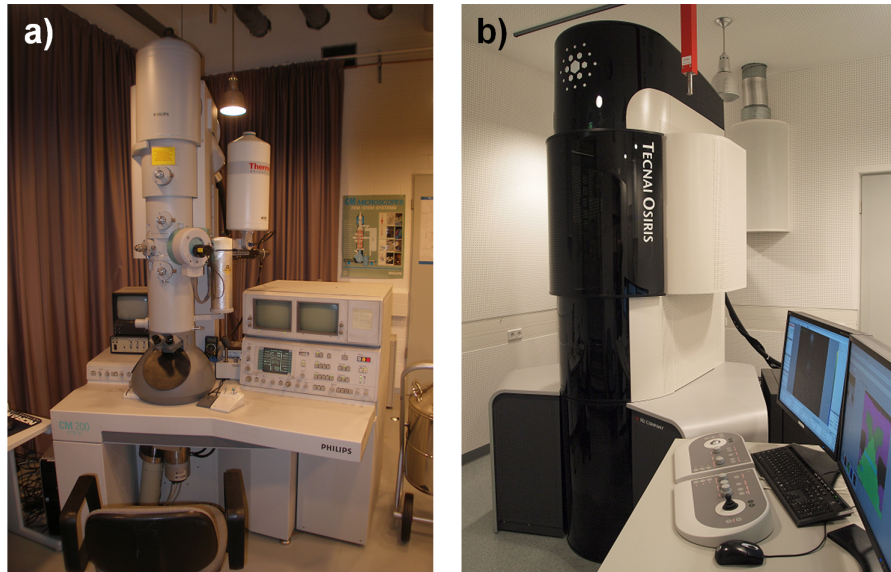


Figure 3.8: Transmission electron microscopes at IHP: a) Philips CM200, b) FEI Tecnai Osiris.

FEM. Nowadays, calculations with an outstanding precision can cope with not only linear but also non-linear systems.

The main aim of FEA is to model a behaviour of an object to a series of given conditions usually found by solving partial differential equations (PDE). The exact analytical solutions can be, however, found only for the simplest and idealized problems. In more complex cases often with a few boundary conditions, PDEs can be solved only numerically. FEA employs a system of points (nodes) forming a grid (mesh) over the whole analysed object. One speaks then of a domain discretization into finite elements schematically shown in Fig. 3.9. All relevant material properties and boundary conditions are at this stage implemented in the computer model. The position of nodes depend on the anticipated magnitude of response. As result, areas of high response (interfaces between materials, corners, etc.) consist of high density of nodes whereas low density of nodes is assigned to regions of small response. Provided that the finite elements are sufficiently small, the solution of PDE in each element can be approximated by a simple function giving rise to the global solution of the PDE.

More detailed information about FEM together with its mathematical formulation can be found for example in [114] or [115].

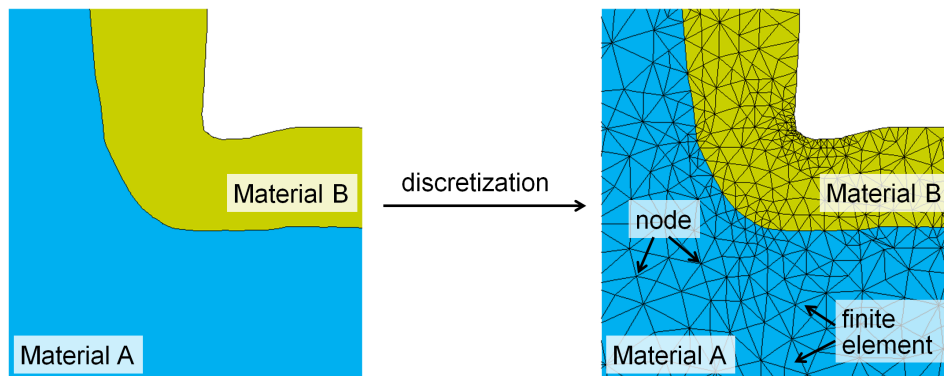


Figure 3.9: Schematic discretization of domain consisting of two regions characterized by different material properties.

FEM simulation

FEM was used to calculate strain field distributions in Ge/Si nanostructures. The strain was then correlated with the experimental results of Raman spectroscopy and XRD studies. A commercial package FlexPDE was employed for this purpose [116]. FlexPDE turns a PDE system into a finite element model and solves it numerically. It offers a script editor, a mesh generator, a finite element solver, and a graphic user interface.

3.3 Sample information

In the following, detailed information on the samples studied in various chapters is given.

Characterization techniques employed in chapter 4.1

Si(001) wafer was nanopatterned according to the recipe reported in section 3.1. In order to investigate the influence of SiO₂ growth mask on the Si nanopattern, samples with two different values of oxide thickness, i.e. 15 nm (5 nm of RTO and 10 nm of TEOS) and 25 nm (10 nm of RTO and 15 nm of TEOS) were investigated. Selective Ge deposition was performed as described in section 3.1. Precise process conditions are reported elsewhere [50].

Micro-Raman measurements were carried out using an InVia Renishaw spectrometer working in backscattering geometry. The samples without epi-Ge were characterized with 364 nm light. Its penetration depth in Si is approximately 12 nm. A x100 objective with numerical aperture of 0.9 was used.

Due to a negligible Raman cross-section of Ge for UV light, a 514 nm laser was used to investigate the samples with Ge epilayer. Its penetration depth in Ge and Si is 19 and 760 nm, respectively. A x100 objective with numerical aperture of 0.85 was used in this case. In order to exclude the effect of heating the material by the laser, its power was reduced. All Raman measurements were done in a series of scans across the line structures on a distance of several micrometers with a step width of 0.1 μm and the polarisation vector of the incident light perpendicular to the structure. The polarisation of the scattered light was neither analysed nor filtered out.

Simulation of stress field was carried out using FlexPDE commercial package based on the Finite Element Method (FEM) [116].

A Philips CM200 transmission electron microscope (TEM) was used to characterize the structure quality of the Si nanopillars and the epi-Ge nanocrystals.

Characterization techniques employed in chapter 4.2

Free standing, 90 nm wide and 150 nm high Si pillars with a periodicity of 360 nm along $\langle 110 \rangle$ crystal direction were realized on a Si(001) substrate as described in section 3.1. The epilayer deposition, depending on its thickness, was carried out in either one- or two-step process by RP-CVD [50]. As a result, Ge nanocrystals with thickness ranging from 4 to 80 nm on open Si seeds were achieved. To study the influence of thermal treatment, the sample with 80 nm thick Ge was additionally annealed for one minute at 800°C in H_2 ambient.

Synchrotron based x-ray diffraction (XRD) studies were performed at the ID01 beamline of the European Synchrotron Radiation Facility (ESRF) in Grenoble (France). To increase the sensitivity towards Ge/Si nanostructures and to suppress the Si(001) substrate signal, the measurements were done in grazing incidence (GI) mode at 0.15° and an x-ray beam energy of 11 keV.

Cross section transmission electron microscopy (TEM) studies were carried out in $\langle 110 \rangle$ projection using a FEI Tecnai Osiris. In addition, elemental analysis by energy dispersive x-ray spectroscopy (EDX) was performed.

Characterization techniques employed in chapter 4.3

50 nm in diameter free-standing Si pillars with a periodicity of 360 nm along $\langle 110 \rangle$ were realized on a Si(001) substrate using a combined CMOS gate spacer process of the IHP 0.13 μm BiCMOS technology [117] and an additional

isotropic wet etching. The Ge growth was carried out in a two-step process by RP-CVD [50].

Synchrotron based XRD studies were performed in GI mode at 0.15° incident angle and an x-ray beam energy of 11 keV at the ID01 beamline at ESRF in Grenoble (France).

Chapter 4

Results and discussion

After the theoretical description of nanoheteroepitaxy approach and its vision of Ge integration on Si(001) in section 2.4, a detailed study of experimental results and discussion is given here.

In **section 4.1**, an investigation of Ge/Si(001) nanostripes is presented. Although the width of the pattern (150 nm) is bigger than the values theoretically predicted for the compliant substrate effects, **the purpose of the study is to develop a successful process of Si substrate nanopatterning and selective Ge deposition**. In addition, the influence of the SiO₂ growth mask on the nanostructured Si substrate is discussed. The choice of the Ge/Si stripe pattern is to allow for a relatively straightforward interpretation of Raman spectroscopy results supported by finite element method calculations. Transmission electron microscopy studies were additionally carried out to report on the structural quality of the nanostructures.

Section 4.2 is dedicated to studies on **growth and relaxation processes in Ge nanocrystals on free-standing Si(001) nanopillars**. The width of Si nanostructures is decreased from around 150 nm, discussed in section 4.1, to 90 nm. The thickness of Ge nanoclusters ranges from 4 to 80 nm and is characterized by synchrotron based x-ray diffraction and transmission electron microscopy. In addition to relaxation studies, the influence of thermal treatment on the quality of Ge nanocrystals is discussed.

Theoretical predictions of the Si pillar width required for the strain partitioning phenomenon are experimentally verified in **section 4.3. Compliant substrate effects versus plastic relaxation in Ge nanocrystals on 50 nm wide Si(001) nanopillars** are presented here.

It is noted, that the discussion presented in this chapter covers the work which was published or submitted to scientific journals. A detailed publication

information is given in chapter 6.1.

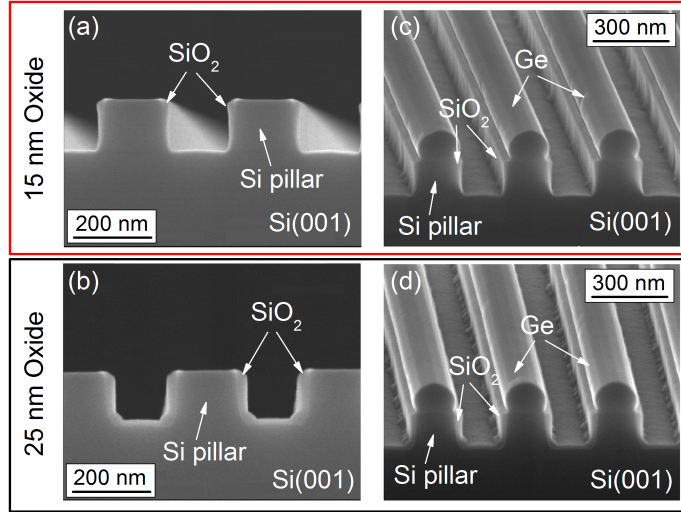


Figure 4.1: SEM of nanopatterned Si structures with 15 and 25 nm thick growth mask: a,b) samples without epi-Ge, c,d) samples with epi-Ge.

4.1 Development of selective Ge CVD process on free-standing 150 nm wide Si nanostructures

4.1.1 Scene setting

In this chapter, we report on Ge selectively grown by chemical vapor deposition on free-standing Si(001) nanostructures. Si(001) substrate is patterned in form of 140 nm high and 150 nm wide stripes along $\langle 110 \rangle$ crystal direction with sidewalls and trenches covered by thermal SiO₂ mask. By opening growth windows of uncovered Si on top of each nanopillar, Ge growth selectivity is realized. The samples with 15 and 25 nm thick oxide mask are characterized by Raman spectroscopy and transmission electron microscopy supported by finite element method simulation. The analysis indicates that, although nanopatterned Si is stressed by thermal oxide, the Si structure quality is not affected. Additionally, the epi-Ge crystal grows in a relaxed form and nearly the whole strain energy is released by the nucleation of a misfit dislocation network at the Ge/Si interface. The residual stress is mainly accumulated in the bird's beak region of Ge/Si nanostructures. More details about the sample processing and characterization for this chapter can be found in section 3.3.

4.1.2 Results and discussion

Scanning electron microscope (SEM) images of nanopatterned Si substrate are shown in Figs. 4.1a and b. Free-standing Si nanostructures after selective Ge deposition are presented in Figs. 4.1c and d with, respectively, 15 and 25 nm SiO₂ growth mask.

Si nanopattern with SiO₂ growth mask

We start the discussion with the results of Raman spectroscopy performed on nanopatterned Si covered with 15 and 25 nm SiO₂. Fig. 4.2a presents the Raman shift of Si-Si vibration obtained in a series of scans across the structure. The spectrum recorded at each point is fitted using a Voigt function. The Raman shift is then calculated as the difference between peak position of the investigated sample and the Si(001) reference. It is visible in Fig. 4.2a, that the measured values of Raman shift are negative for both cases. This situation corresponds to the Si nanostructure stressed by the growth mask. The thickness of SiO₂ affects the average Raman shift, namely the thicker the SiO₂ growth mask, the bigger the Raman shift to negative values: the average Raman shift amounts to -0.14 and -0.44 cm⁻¹ for 15 and 25 nm oxide, respectively. Additionally, the oxide influences the amplitude of the peak position variation when moving across the structure. As seen in Fig. 4.2a, a difference of 0.1 cm⁻¹ is observed for 15 nm SiO₂. This value increases to 0.17 cm⁻¹ for 25 nm SiO₂. The experiment was done with a laser spot size smaller than the periodicity of the structure (360 nm). The full width at half maximum (FWHM) equals 300±50 nm. The Fourier transformation of the signal in Fig. 4.2b reveals, that the periodicity of the Raman shift as well as the peak intensity oscillation in both samples originates from the periodicity of the structure. Small deviation from this value can be caused by a small misalignment of the sample with respect to ⟨110⟩ direction. Next, FEM analysis of both samples was performed in order to investigate the stress field distribution and the observed Raman shift in more detail. First, the description of our theoretical model together with main assumptions is given.

The exact shape of the Si nanopillar and the SiO₂ growth mask employed in the calculation was taken from cross-section TEM images. The substrate thickness was increased until its influence on the stress in the nanopatterned pillar was eliminated. The domain was then built from three nanostructures equally spaced from each other. Both right and left boundaries were fixed in

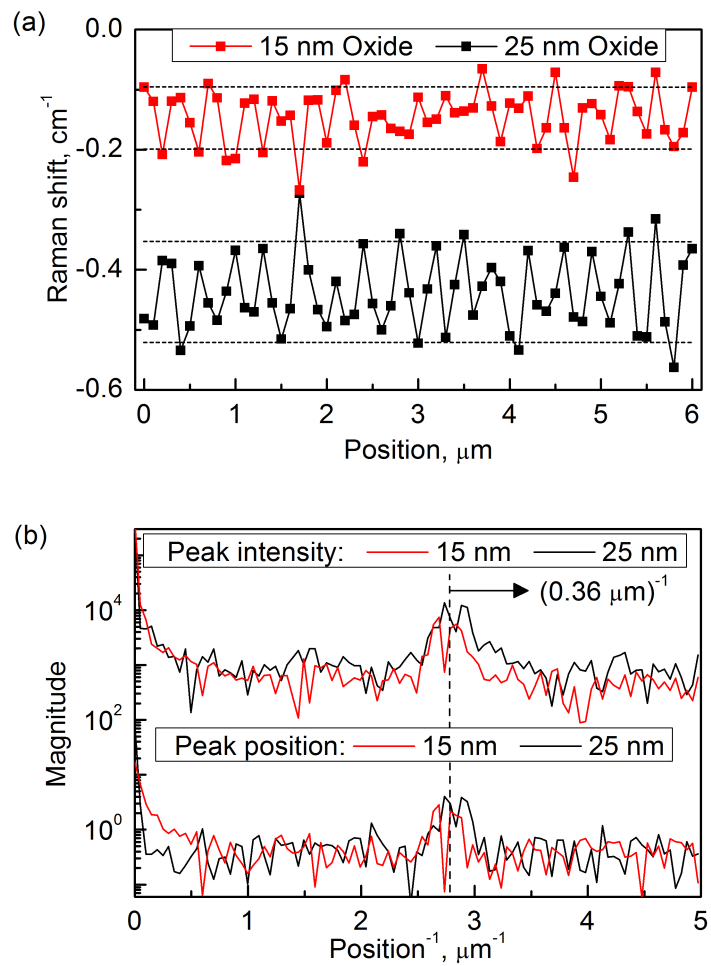


Figure 4.2: Dependence of Si-Si vibration Raman shift on position during a scan across the structure (a) and Fourier transform of the Si-Si peak intensity and position (b).

the in-plane x direction (no displacement in x direction was allowed). A rigid Si substrate was realized by the bottom of the domain fixed in z direction.

No initial stress is assumed in Si. In SiO₂ growth mask however, there are two homogeneously distributed stress components, i.e. thermal and growth stress. The first one arises from different thermal expansion coefficients between substrate and the oxide whereas the second one originates from the process of growing SiO₂ on Si. It is known, that when a Si surface is thermally oxidized, a newly formed dioxide expands and stresses Si. Additionally in nonplanar (patterned) case, when Si under the antireflection coating (ARC) is oxidized a so-called bird's beak is created [101, 102]. Throughout this chapter we assume that the growth stress in SiO₂ amounts to 300 MPa [102] and treat this value as a case study. In consequence, we try to interpret the experimental results only in a qualitative way. The calculated displacement field in a Si pillar covered with 25 nm thick oxide mask is presented in Fig. 4.3. In the x direction, Si is strongly compressed especially at the base of the pillar and at the top edge of the pillar (bird's beak region). The first effect comes from the fact, that the free surface of the oxide is limited and the material cannot expand freely as it does for example at the sidewall. In consequence, the force acting on the pillar base is bigger and so is the x -displacement. On the other hand, the bird's beak area in Si is vulnerable for displacement as it is an edge region with two fronts of acting oxide. Additionally, the whole nanopillar is tensile strained in z direction. We now discuss how the simulated stress field is used to calculate the Raman shift.

It was shown, that mechanical stress and strain changes the phonon frequencies of materials [118, 119]. The strength of this influence on the frequency of three optical phonons can be calculated by solving the secular equation [101, 110]:

$$\begin{vmatrix} p\varepsilon_x + q(\varepsilon_y + \varepsilon_z) - \lambda & 2r\gamma_{xy} & 2r\gamma_{xz} \\ 2r\gamma_{xy} & p\varepsilon_y + q(\varepsilon_x + \varepsilon_z) - \lambda & 2r\gamma_{yz} \\ 2r\gamma_{xz} & 2r\gamma_{yz} & p\varepsilon_z + q(\varepsilon_x + \varepsilon_y) - \lambda \end{vmatrix} = 0 \quad (4.1)$$

where p , q , and r are the phonon deformation potentials (PDPs), ε_{ij} and γ_{ij} are normal and shear strain components, respectively. We assume, that no displacement along the line structure is allowed. This assumption, known as the plane strain approximation, corresponds to an object (xz plane) being constrained without friction between two rigid immobile plates. It additionally implicates, that all ε_y components in Eq. 4.1 vanish. The elasticity constants

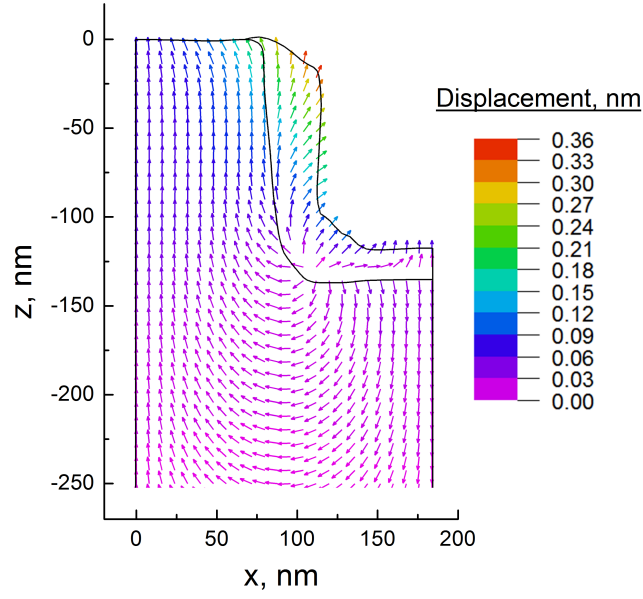


Figure 4.3: Displacement field in Si nanostructure under stress from SiO₂ mask.

C_{ij} (combining strain and stress according to elasticity relations) as well as PDPs are rotated to reflect the patterning along $\langle 110 \rangle$ direction. The shift of Raman frequencies of three optical phonons can now be calculated from:

$$\Delta TO_1 = \frac{1}{2\omega_0} (p'\varepsilon_x + q\varepsilon_z), \quad (4.2)$$

$$\Delta TO_2 = \frac{1}{2\omega_0} (q'\varepsilon_x + q\varepsilon_z), \quad (4.3)$$

$$\Delta LO = \frac{1}{2\omega_0} (q\varepsilon_x + p\varepsilon_z). \quad (4.4)$$

Here, ω_0 is the phonon frequency in the absence of stress and amounts approximately to 301 and 520 cm^{-1} for Ge and Si, respectively. The rotated PDPs are found from [120]:

$$p' = \frac{1}{2}(p + q) + r, \quad (4.5)$$

$$q' = \frac{1}{2}(p + q) - r. \quad (4.6)$$

Due to symmetry reasons, in the backscattering geometry from a (001) surface, only the third Raman mode (Eq. 4.4) can be observed. In Figs. 4.4a and b we present the Raman shift of LO mode in the whole nanostructure covered by, respectively, 15 and 25 nm thick SiO₂. The values at the top pillar and at the bottom trench ((001) surfaces) are positive. The maximal value corresponds

to the bird's beak region and is higher for a thicker oxide. This observation is in contradiction with the experimental results where only negative Raman shift was observed (see Fig. 4.2). It is evident from the calculation, that the only region corresponding to negative Raman shift is the central part of the nanopillar and the (1-10) sidewall. The selection rules for backscattering from (110) surface allow, however, the detection of additional TO modes (Eq. 4.2 and 4.3) which eventually mix with LO mode. In Figs. 4.4c to f we show the Raman shift of TO_1 and TO_2 modes for 15 and 25 nm thick SiO_2 . The values at the sidewalls are indeed negative and (especially in case of TO_2) dependent on the oxide thickness. Although the values of TO_2 mode shift in the upper part of the sidewall are comparable for both oxide thicknesses, the Raman shift in the lower part is around twice bigger in case of 25 nm thick SiO_2 (see Figs. 4.4e and f). In order to reproduce the experimental results shown in Fig. 4.2a, one should consider two additional effects, i.e. laser spot size and the distribution of scattered light. The FWHM of laser spot although smaller than the lateral periodicity of the nanostructures, is bigger than the pillar width. This means that the experimental signal is averaged over approximately 300 nm. In consequence, a scan across the structure changes only the average value of Raman shift by the varying contribution of more positive or negative signal elements. The distribution of light inside the structure is the second effect. Since, we consider materials with different optical properties and structures with dimensions smaller than the light wavelength, one could expect that the signal will not scatter from the grating homogeneously [121]. In consequence, different regions of the structure will sum differently to the total signal observed experimentally. In conclusion, our simulations indicate that the experimentally observed negative Raman shift is mainly caused by the strain state of the Si nanostructure sidewalls. In addition, the observed bigger negative Raman shift for thicker SiO_2 points to an important contribution of the TO_2 mode to the overall signal. It must, however, be pointed out that this preliminary interpretation is calling for an in-depth analysis of the Raman signal from such nanopatterned Si wafers. Such an analysis, including in especial the light distribution, in the Si grating, is however beyond the scope of this selective Ge growth study.

To investigate whether the patterning process generates any crystal defects (e.g. oxidation induced stacking faults) in Si nanostructures, cross section TEM images of both samples with different SiO_2 thickness are presented in Figs. 4.5a, b. It is visible that the nanopatterned structure is of high quality.

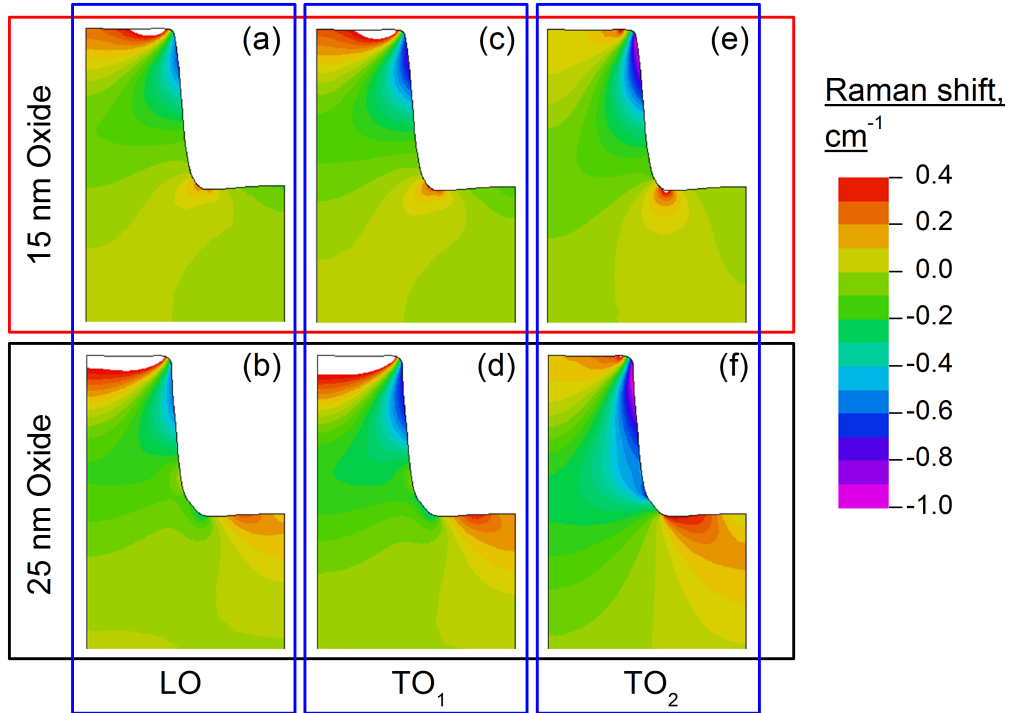


Figure 4.4: Raman shift of Si-Si vibration in nanopatterned Si structures without epi-Ge covered by 15 nm and 25 nm SiO₂: a,b) LO mode, c,d) TO₁ mode, e,f) TO₂ mode.

It was reported, that the bird's beak is the place of defect injection [102], however, high resolution micrographs in Figs. 4.5c, d show no defects in Si nanostructures.

Ge selectively deposited on Si nanostripes

We start with the results of Raman spectroscopy of the samples presented in Figs. 4.1c and d. In Fig. 4.6 we present the shift of Si-Si and Ge-Ge vibration for two thicknesses of SiO₂ growth mask (15 and 25 nm). All the spectra were collected on an area of 6x6 μm with a step of 0.1 and 0.5 μm in horizontal and vertical direction, respectively. The mapping was done using a laser configured to use a linefocus lens. Similarly to the case without Ge, the Raman shift of the Si signal is negative. Again, this is caused by the SiO₂ growth mask. The changes are, however, smaller than in the case of uncovered Si nanostructures. The reason for this behaviour is due to a different penetration depth of 364 and 514 nm laser light which equals, respectively, to 12 and 760 nm in Si. A smaller shift of Si-Si peak in the latter case is thus caused by an averaging effect of a larger volume which the Si signal originates from. The Raman shift

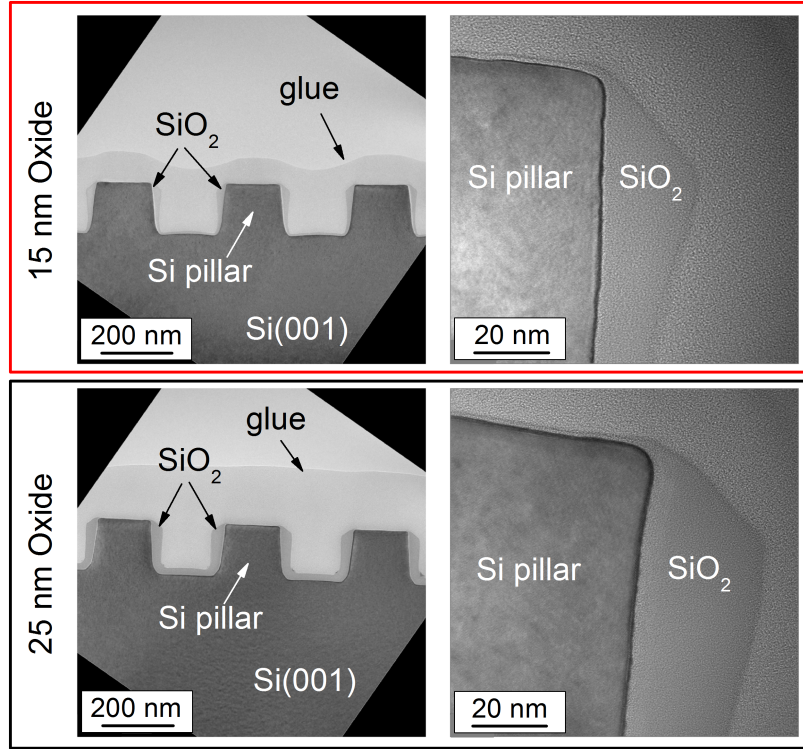


Figure 4.5: Cross section TEM image of nanopatterned Si substrate.

of Ge-Ge vibration is as well negative, however, the absolute values are rather small (from -0.25 to 0.05 cm^{-1}). Partially blurred Ge signal may be caused by fluctuations in residual strain fields originating from e.g. the growth mask and/or threading dislocations trapped in the epilayer. Neither for Si-Si nor Ge-Ge vibrations, the influence of SiO_2 thickness is clearly visible. It is noted, that a well defined periodicity is resolved in all maps. Fourier transformation of the peaks position as well as peaks intensity (not shown) proves that it reflects the lateral periodicity of the structure. Next, in order to understand the experimental data, we describe the results of finite element simulation.

As it was already discussed, when Ge is grown on Si, next to thermal mismatch an additional strain due to different lattice constants takes place. The lattice mismatch amounts to 4.2% and is used as a starting value of the strain in FEM simulation. No initial stress is assumed in the Si structure. Next to the thermal stress, we assume 300 MPa growth stress in the oxide mask (similar to the samples without Ge). The simulated stress field is then used to calculate the strain energy density (see Fig. 4.7) defined as work done per unit volume [122]:

$$U = \frac{1}{2}(\sigma_x \varepsilon_x + \sigma_y \varepsilon_y + \tau_{xy} \gamma_{xy}) \quad (4.7)$$

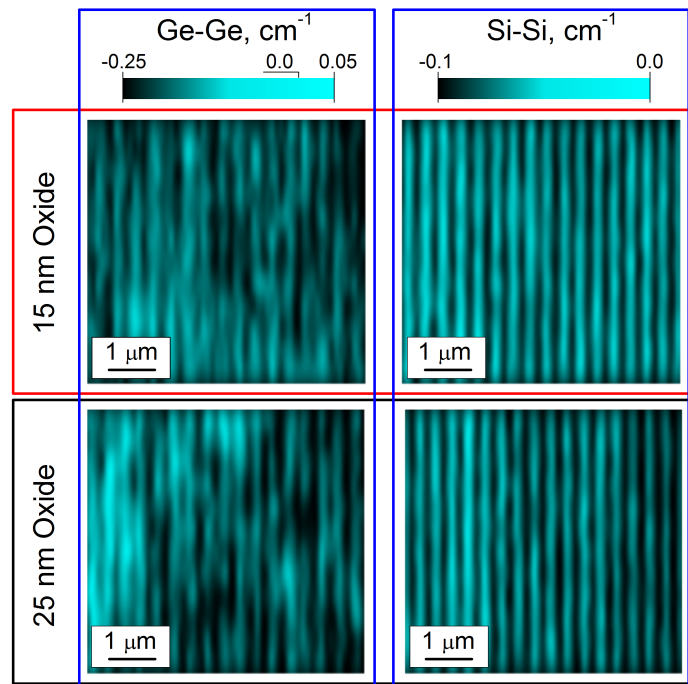


Figure 4.6: Map of Raman shift of Si-Si and Ge-Ge vibration. The average values for Ge (Si) signal are -0.13 (-0.05) and -0.14 (-0.06) cm^{-1} for 15 and 25 nm SiO_2 respectively.

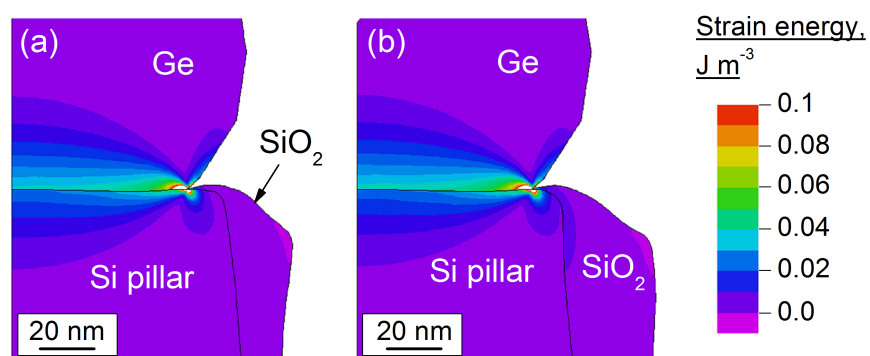


Figure 4.7: Strain energy density of Ge/Si nanostructure with 15 (a) and 25 nm (b) thick oxide.

Here σ_i and τ_{xy} are normal and shear stress components. The highest value of the strain energy is present at the Ge/Si interface and close to the bird's beak region. It is important to realize, that this region is directly affected by the growth mask: Si top pillar is compressed by expanding SiO₂ (see Fig. 4.3). The strain energy density decreases when a thinner oxide is used. Besides the strained Ge/Si interface area, we observe a rapid decay of strain energy in the Ge crystal away from the Ge/Si interface. To verify the Ge epilayer quality, TEM micrographs are discussed next.

In Fig. 4.8, we present TEM images of sample with 15 nm thick SiO₂ growth mask (same tendencies observed for 25 nm thick oxide). The cross section image in Fig. 4.8a is an overview of a few line structures. Good growth selectivity and reproducibility of the epilayer shape with well pronounced facets are visible. In Fig. 4.8b we superimpose a typical Ge nanostructure shape by a Wulff construction. The latter depicts the Ge equilibrium crystal shape (ECS). The used surface energies correspond to relaxed and reconstructed geometry recently calculated by Stekolnikov et al. [123]. $\langle 001 \rangle$, $\langle 113 \rangle$, $\langle 111 \rangle$, and close to $\langle 110 \rangle$ facets can be identified. A small deviation in the shape of the Ge crystal in comparison to ECS is visible. The surface of $\langle 113 \rangle$ facet is bigger whereas the surface of $\langle 111 \rangle$ facet is smaller than the one arising from the theoretical crystal shape. The difference arises from the fact, that the crystal depicted by the Wulff construction is assumed to grow on an unlimited area. Although this criterion is met in the first stage of growth, it is no more valid when Ge reaches the edges of the Si pillar and SiO₂ growth mask. From this moment on, the growth of the facets which are constricted by the size of the nanoseed will be hindered or stopped whereas the facets which are not limited (e.g. by the oxide mask) will expand freely. Due to the selective Ge CVD growth process, the Ge crystal can only grow in vertical direction, preserving the shape of the Wulff construction with the low energy facets (e.g. $\langle 113 \rangle$ in Fig. 4.8b) most pronounced. Despite these small differences, one can see that the Ge nanostructure shape fits well to fully relaxed ECS (Fig. 4.8b). This result demonstrates, that in line with the Raman study, the selective Ge nanoheteroepitaxy process results in a (nearly) fully relaxed Ge on the free standing Si nanostructures. Similar conclusions were derived from our recent x-ray diffraction studies [124]. A small deviation in the shape of neighbouring Ge nanostructures as well as slight asymmetry within each Ge crystal is visible and may be caused for example by residual stress originating from the nanopatterning procedure. Most of the strain energy is, however,

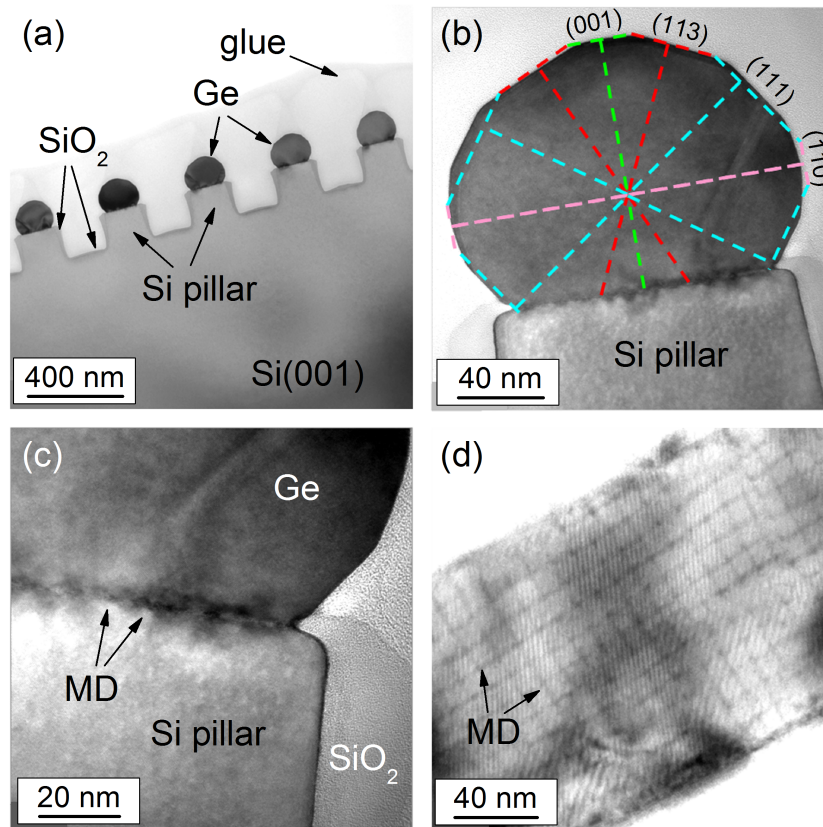


Figure 4.8: Cross section overview (a), Wulff construction (b), region close to bird's beak (c), and plane view (d) TEM images of epi-Ge grown on nanopatterned Si substrate with 15 nm SiO_2 mask.

released by nucleation of misfit dislocations (MDs) visible in Fig. 4.8c at the Ge/Si interface and in the plane view in Fig. 4.8d. The average MDs spacing equals approximately 10.6 nm which is slightly higher than the theoretical predicted value of 9.6 nm [125]. In consequence, the epi-Ge nanostructures are not fully, but almost fully relaxed. The value of residual strain based on the MDs spacing amounts to 0.4%. It is noted in addition, that a detailed XRD investigation of the quality of Ge crystal in terms of defects was given by Zaumseil et al. [124]. The studies show that, additional structural defects (stacking faults and microtwins) are generated when the Ge nanostructures start to overgrow the SiO_2 mask. As long as the amount of Ge is smaller (case studied here), the Ge nanostructures are of high quality and mostly defect-free (Fig. 4.8b).

In the FEM simulation, we assume that the initial strain in epi-Ge originates from thermal mismatch and the residual strain. In Figs. 4.9a, b, and c, we present the calculated distribution of Raman LO, TO_1 , and TO_2 shift

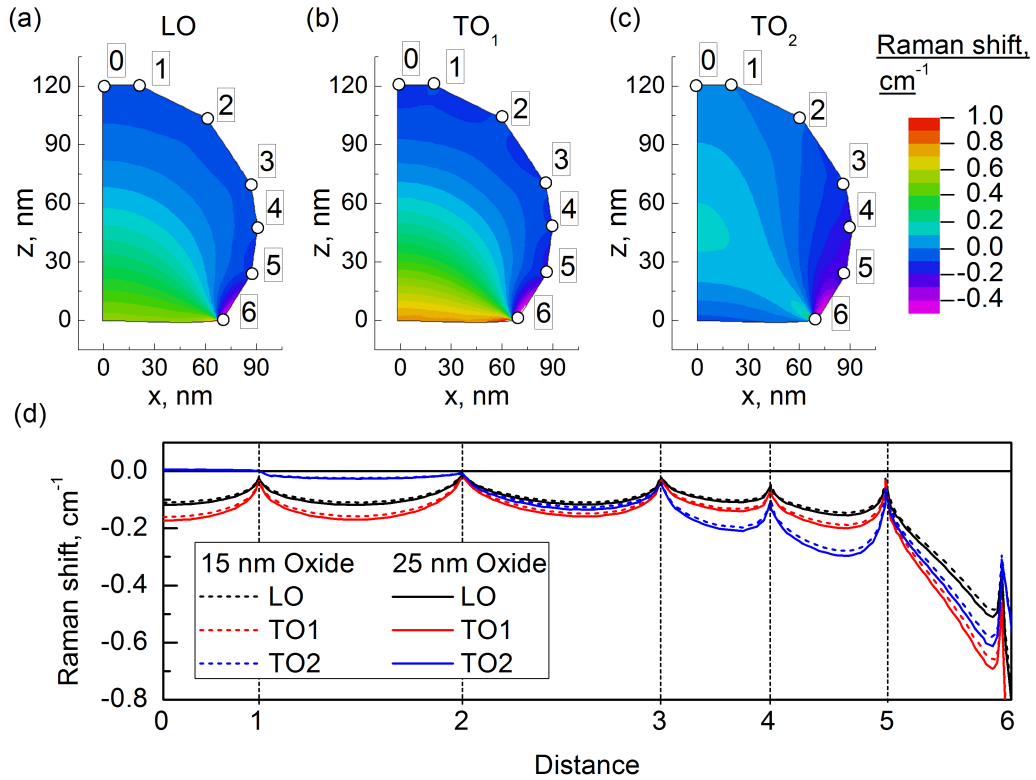


Figure 4.9: Calculated Raman shift in Ge crystal on Si nanostructure covered by 25 nm oxide: (a) LO, b) TO_1 , and c) TO_2 . Comparison of Raman shift on the surface of Ge (d).

in the whole Ge crystal on top of the Si nanostructure with 25 nm thick SiO_2 growth mask. Since the used 514 nm laser wavelength provides an information depth of approximately 20 nm in Ge, in Fig. 4.9d we plot discrete values of the Raman shift on the crystal surface moving from the top (point 0) to the bird's beak (point 6). Due to numerical aperture of the objective, the material between points 5 and 6 is at least partially shadowed in the experiment. The Raman shift on Ge crystal surface for all modes is mostly negative. Nearly no oxide dependence is visible and would not be resolved experimentally. It is noted, that the experimental values of the averaged Raman shift (Fig. 4.6) change in the same range like the simulated value on the surface of Ge crystal (from -0.25 to 0.05 cm^{-1}). In addition, the calculation reveals that the Raman shift close to the shadowed bird's beak is the highest in the whole epilayer. This region is highly affected by the thickness of expanding SiO_2 . The latter point is of importance for controlling the Ge growth and structure on the nano-scale in future studies for device applications.

4.1.3 Summary

In summary, we presented a successful development of a selective Ge CVD heteroepitaxy process on free standing Si(001) nanostructures. By a proper lithography mask and doping profile, such structures could be relevant for future photonic application. We investigated first the influence of the SiO₂ growth mask on the quality of nanopatterned Si. We found, that the amount of stress in the substrate depends on the thickness of the oxide, i.e. nanostructures covered with thicker SiO₂ are subjected to bigger stress. However, no oxidation related defects were observed and Si nanostructures of high quality were realized. Next, we investigated selectively grown epi-Ge. Our work indicates, that the lateral dimensions of the Si nanoseeds can be used to influence or even control the shape of Ge nanostructures. The shape of the Ge crystals are close to the ECS which, together with Raman studies, demonstrates that Ge growth is nearly fully relaxed. Most of the strain energy in the epilayer is released by the nucleation of misfit dislocations at the Ge/Si interface. Residual strain is of the order of thermal strain.

After studies on the classical approach of Ge selective integration on 150 nm wide Si nanopatterns presented here, discussion in the next section will be focused on growth studies on nearly two times narrower Si nanopillars.

4.2 Growth and relaxation study of Ge nanocrystals on free-standing 90 nm wide Si nanopillars

4.2.1 Scene setting

In the previous section, we developed a CVD based selective growth process of Ge on 150 nm wide Si nanostructures. Here, using synchrotron based x-ray diffraction and transmission electron microscopy, we study in detail the growth and relaxation processes in Ge nanocrystals with thickness ranging from 4 to 80 nm grown on 90 nm wide Si nanopillars. We show, that the strain in Ge nanostructures is plastically released by nucleation of misfit dislocations which lead to relaxation degrees in the range from 50 to 100%. The growth of Ge nanocrystals follows the equilibrium crystal shape terminated by low surface energy (001) and {113} facets. However, the shape and size of Ge crystal is not uniform and the crystal quality is limited by volume defects on {111} planes. This is not the case for the Ge/Si nanostructures subjected to thermal treatment. Here, improved structure quality together with high uniformity of shape and size is observed. More details about the sample processing and characterization for this chapter can be found in section 3.3.

4.2.2 Results and discussion

Scanning electron microscope (SEM) images of the investigated nanostructures are shown in Fig. 4.10. The Si nanopillars with variable amount of Ge coverage are clearly visible. For all investigated samples, high Ge growth selectivity is evident. Corresponding TEM micrographs of one representative Ge/Si nanostructure are shown for each sample on the right of Fig. 4.10.

The thinnest 4 nm epi-Ge in Fig. 4.10a (referred later as sample A) shows a rough surface. From the TEM micrograph it is visible, that Ge forms nanoislands of different sizes on Si. Ge clustering could be caused for example by inhomogeneous strain fields in the Si seeds that influence Ge growth mode. In the near future, a detailed surface science study will be performed to elucidate whether the Ge growth mode on Si nanostructures follows the Stranski-Krastanov characteristic known from Si bulk substrates [63]. In Fig. 4.10b (sample B), 8 nm thick Ge with (001) and most likely (113) crystal facets is visible. Those facets are common for Ge clusters grown on Si and form during the morphology transition from "huts" to "domes" [63]. The typical height to

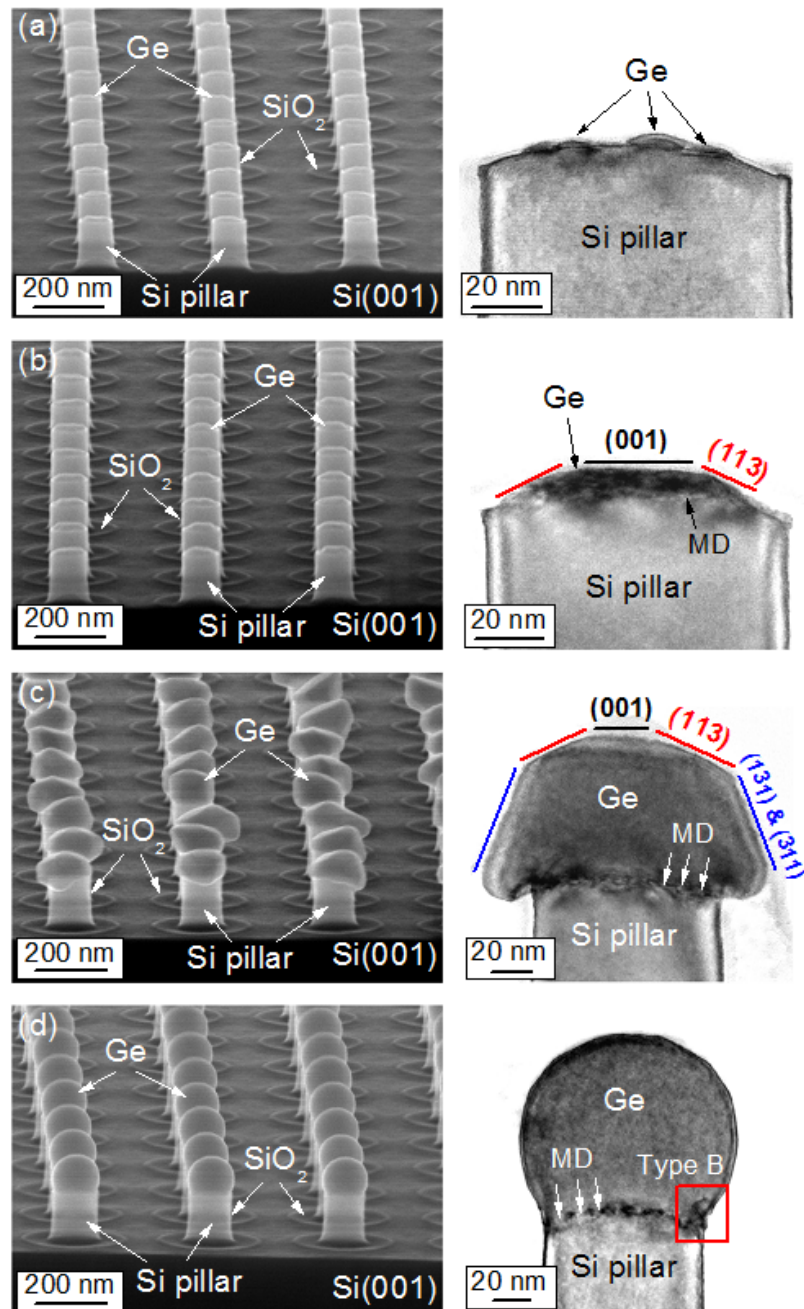


Figure 4.10: Ge clusters on free-standing Si nanopillars: 4 nm (a), 8 nm (b), 80 nm (c), and annealed 80 nm thick Ge (d).

length ratio of 0.15 for Ge domes is also observed in Fig. 4.10b. Its value can be, however, influenced by the limited Si seed area. In Fig. 4.10c, we present 80 nm thick Ge nanostructures (sample C). A wide distribution of Ge crystal shape may be caused by residual strain fields in the Si seed prior to Ge growth and/or formation of microtwins in epi-Ge during the deposition [126]. Despite this inhomogeneity, typical (001) and (113) facets are identified. In addition, (13L) and (31L) facets intersecting at (110) plane were found in a plane view TEM image. The inclination of the third observed "facet" in Fig. 4.10c proves that it is the edge of intersecting (131) and (311) facets. In line with the theoretical calculations presented by Stekolnikov et al. [123], this result shows that the as deposited Ge crystal is built mainly from {113} facets of low surface energy. The absence of (111) facets and thus a small deviation from the expected equilibrium crystal shape is likely caused by a limited area of the Si seed. In Fig. 4.10d, we present the annealed sample D with round shape clusters of high uniformity (see SEM micrograph). A closer look on the TEM image reveals that the Ge nanostructure is composed of additional facets. This morphological change in comparison with sample C is driven by the rearrangement of Ge atoms minimizing the total crystal energy for a given elevated temperature. During the annealing process, Ge atoms migrate away from areas of high surface energy E_{surf} at the Ge/SiO₂ interface. Since the step free energy decreases at higher temperatures [127, 128], E_{surf} can be further reduced by formation of additional facets and lowering the surface area. On the other hand, the volume energy is decreased by Ge atoms migrating away from areas of high strain fields e.g. the region of unintentionally oxidized Si known as the bird's beak [129]. In consequence, a round-shape crystal with uniform size and shape distribution is developed by annealing and a subsequent thermal quenching.

In addition, the analysis of the TEM micrograph in Fig. 4.10d indicates, that nearly the whole Ge nanostructure is of high quality and defect-free, exhibiting type A crystal orientation inherited from the Si substrate. However, material with a stacking vector rotated 180° around $\langle 111 \rangle$ direction (type B) is also observed in the epilayer region overgrowing the SiO₂ mask (marked by a red square). This area was already discussed as a possible source of additional structural defects (stacking faults and microtwins) [124]. The residual stress accumulated close to the bird's beak may additionally contribute to defect nucleation [102]. Two crystal orientations are present also in samples not subjected to the thermal treatment. In addition, we found misfit dislocations (MDs) at the Ge/Si interface for samples B, C, and D. Their average spacing

in Figs. 4.10c and d is similar to the value expected for relaxed Ge on Si(001). The average MDs spacing in Fig. 4.10b is, however, bigger. It indicates, that the strain in Ge is not completely released and that the epilayer is compressed. Next, we corroborate the TEM results by highly sensitive synchrotron-based XRD studies which report a highly averaged structure analysis of samples A to D.

We start the analysis with the reciprocal space map (RSM) around the in-plane (400) Bragg reflections of Si and Ge ($L = 0.02$) presented in Fig. 4.11. The position of the bulk lattice constant is marked by a solid vertical line at $H = 3.84$ (Ge) and $H = 4$ (Si). In all cases, the position of Si reflection corresponds to bulk material and its shape is nearly symmetric. In order to analyse it in more detail, in Fig. 4.12 a high resolution RSM around Si(400) reflection is shown. We focus here only on sample D, however, the same tendencies are observed for all investigated samples. A strong peak at $H = 4$ corresponds to Si with bulk lattice constants. Additional satellites around the Bragg reflection correspond to the 2D lateral periodicity of the nanopatterned substrate. The expected positions for the 360 nm period structure are marked schematically by white circles and fit well to the experimental data. Fourier transformation of the real space pattern (pillars height and width) and strain fields within the nanostructure partially explain the observed intensity deviation and the absence of some satellites. Further theoretical simulations are currently on going. The elliptical shape of the satellites is a result of the instrumental resolution (detector slits etc.).

The character of Ge(400) Bragg reflection in Fig. 4.11 is influenced by the relaxation degree, size, and shape of the Ge nanocrystal. In sample A (Fig. 4.11a), the Ge signal is shifted towards Si which indicates an in-plane compressive strain. Its value of 1.4 - 2.6% cannot be precisely estimated due to a broad shape of the peak. This is probably caused by small lateral dimensions and/or a wide distribution of Ge crystal sizes with a varying degree of relaxation. The position of the Ge peak can be better resolved for sample B (see Fig. 4.11b). The epilayer is compressively strained with a strain value of around 1% in the in-plane direction. In Figs. 4.11c and d, we present the RSMs of (400) reflection for sample C and D, respectively. In both cases, the position of the Ge signal indicates material with relaxed bulk lattice constants ($H = 3.84$). The elongation in K direction can be attributed to a certain twist of lattice planes. Its value obtained from full width at half maximum (FWHM) amounts to 0.34° and 0.29° for sample C and D respectively. The Ge peak for

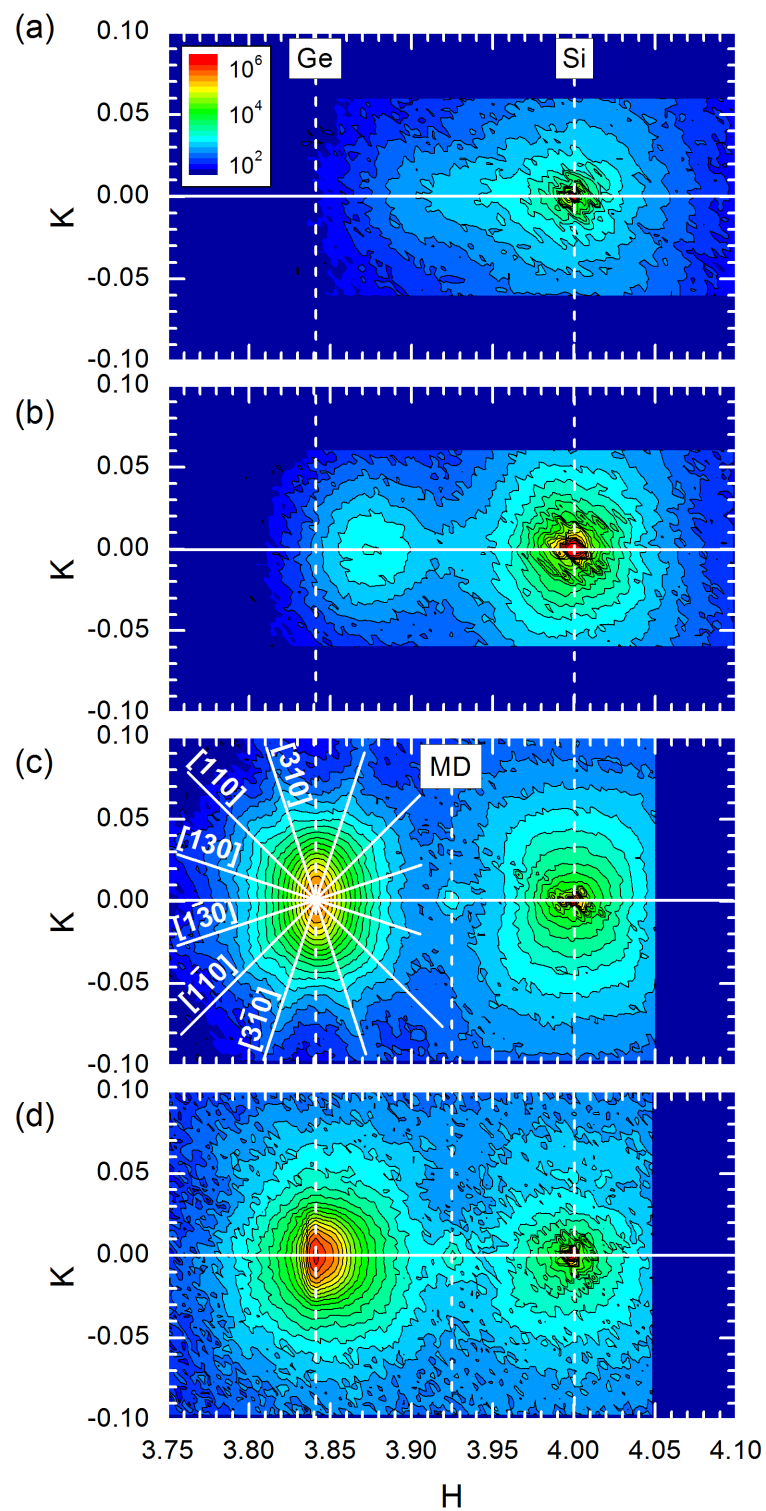


Figure 4.11: RSMs of in-plane (400) Bragg reflections: 4 nm (a), 8 nm (b), 80 nm (c), and annealed 80 nm thick Ge (d).

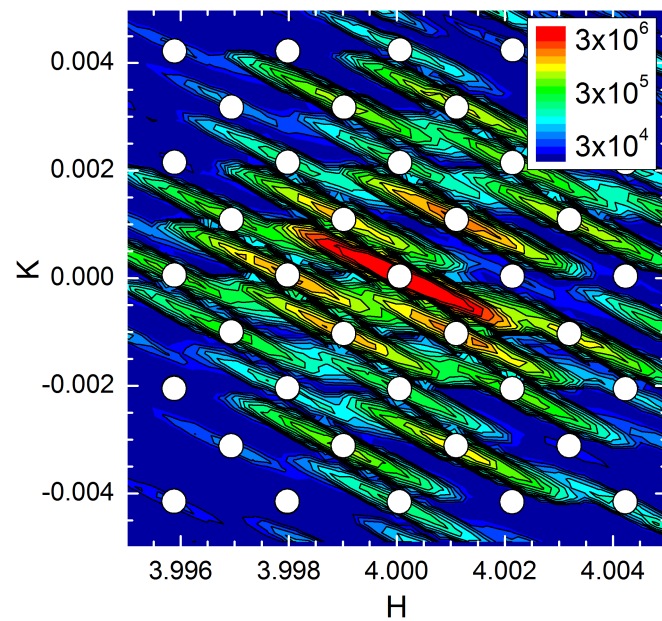


Figure 4.12: High resolution RSM of in-plane Si(400) Bragg reflection (sample D). Expected positions of satellites from the 360 nm periodic nanostructures are marked by white circles.

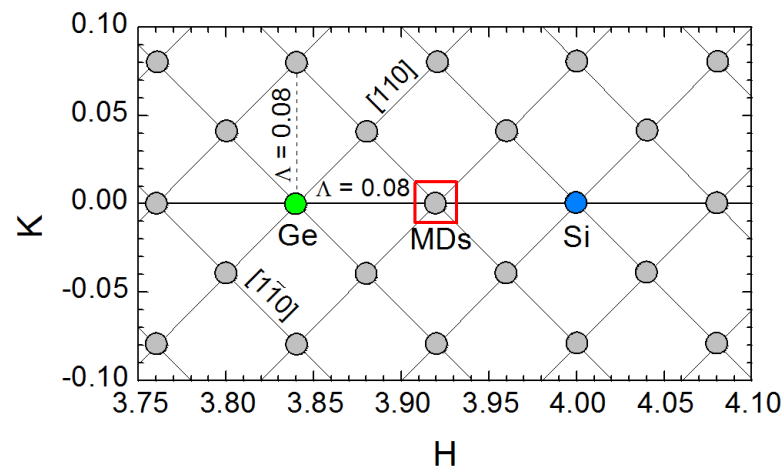


Figure 4.13: Schematic representation of the RSM around (400) Bragg reflection. Grey circles correspond to satellites of MDs at the Ge/Si interface along $\langle 110 \rangle$.

sample C is symmetric around $H = 3.84$ with well pronounced streaks along $\langle 130 \rangle$ and $\langle 310 \rangle$ which correspond to the projection of Ge crystal facets discussed already by TEM (Fig. 4.10). Additional $\langle 110 \rangle$ streaks can result from high density structural defects on $\{111\}$ planes (e.g. stacking faults). In contrast, diffuse scattering around Ge(400) reflection for the annealed sample D (Fig. 4.11d) shows no streaks even for $\langle 110 \rangle$ direction. The peak is, however, asymmetric with a shoulder at higher H values. This indicates Si interdiffusion and the formation of a SiGe layer during the annealing process.

It was already shown by TEM, that strain in the Ge epilayer is relieved plastically. In consequence, an ordered network of MDs at the Ge/Si interface is formed and can be detected by GI-XRD close to Bragg reflections. The periodicity of the ordered MD network is given by $\Lambda = a_s(1 - f)/f$, where a_s is the substrate lattice constant and f is the lattice mismatch [130]. For the Ge/Si(001) system $\Lambda = 12.5$ nm which results in our study in a reciprocal in-plane periodicity of 0.08. In Fig. 4.13, we present a schematic RSM around (400) reflection with MD satellites shown as grey circles. It is visible in Figs. 4.11c and d, that MDs contribute to an additional peak (MD) exactly situated between Ge and Si reflections at $H = 3.92$. Also in case of sample B, a linescan through (400) Bragg reflections at $K = 0$ (not shown) reveals an MD satellite exactly between Ge and Si peaks.

It was reported, that GI-XRD investigation around forbidden Bragg reflections can be used to detect the presence and determine the type of defects inside the material [131]. To study the effect of annealing on the quality of the Ge nanostructures, we next analyse the forbidden (200) Bragg reflection for samples C and D shown in Fig. 4.14. Both RSMs are presented on the same intensity scale range. Despite a small intensity difference of the background level, streaks along $\langle 110 \rangle$ crossing at the Ge(200) reflection for as deposited sample C are easily distinguished. Such streaks at Ge(200) are characteristic projections of either stacking faults or twin faults on $\{111\}$ planes [131]. Similar to sample C, the streaks are visible for the annealed sample D, however, the contrast in this case is much weaker. This result proves that the annealing step reduces the density of volume defects on $\{111\}$ crystal planes and thus the quality of epi-Ge nanostructures increases [132].

Fig. 4.15 shows RSMs of the out-of-plane (202) Bragg reflection for all investigated samples. A broad vertical streak at $H = 2$ corresponds to scattering from the Si(200) crystal truncation rod (CTR). Additional smaller lateral streaks marked by arrows are probably caused by the diffraction on the side-

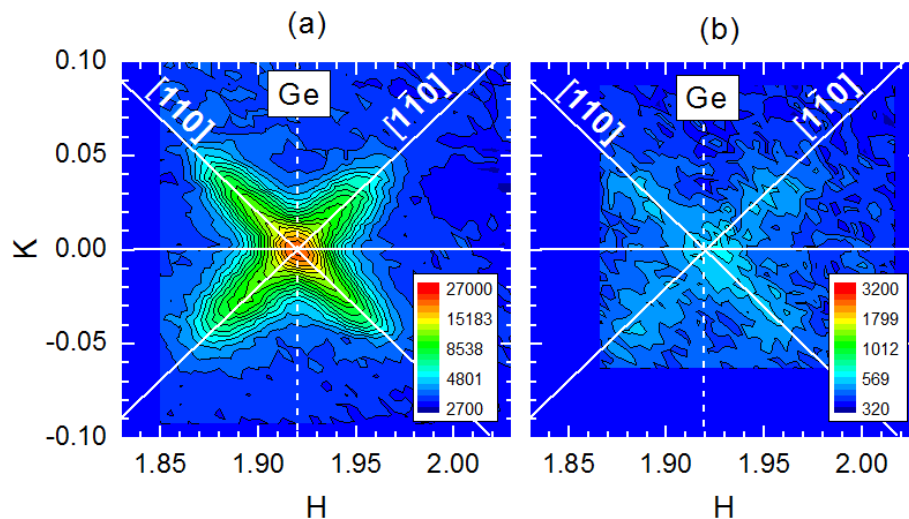


Figure 4.14: RSMs of in-plane (200) Bragg reflections: (a) as deposited, (b) annealed Ge.

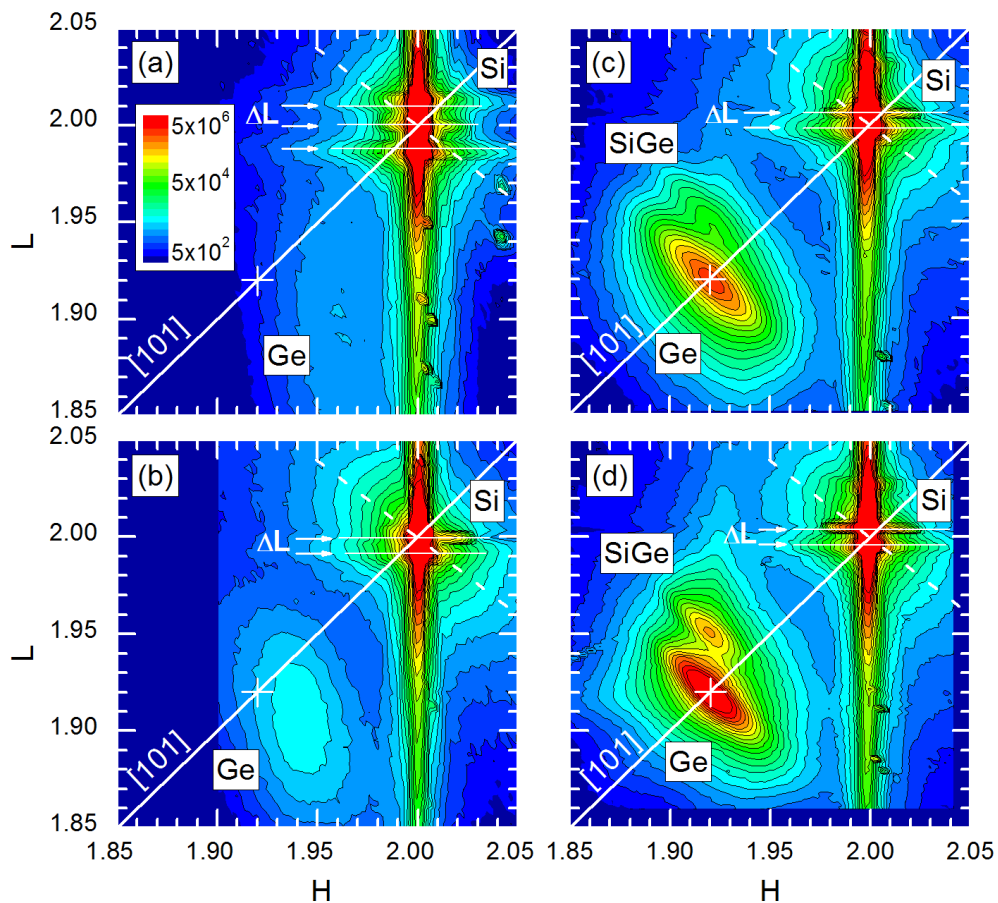


Figure 4.15: RSMs of in-plane (202) Bragg reflections: 4 nm (a), 8 nm (b), 80 nm (c), and annealed 80 nm thick Ge (d). The position of bulk Ge(202) is marked by a white cross.

walls of Si nanopillars. Their spacing ΔL roughly corresponds to the height of nanostructures. The intensity variation of these diffuse scattering signals from sample to sample may be caused by an insufficiently small step between the neighbouring measurement points. Diffuse scattering around the Si peak itself is a consequence of finite crystal size, defects, and strain fields in the patterned Si(001). Here, we focus on possible strain signatures which mostly contribute to the streak perpendicular to [101] direction (dashed line). The analysis of the in-plane strain in Si nanopillars of samples A to D shows that it is more affected by compressive strain due to the SiO₂ growth mask than by tensile strain due to Ge overgrowth.

It is visible for sample A (Fig. 4.15a) and B (Fig. 4.15b), that the Ge peak is shifted away from the expected bulk position marked by a cross. It is shifted away from the [101] direction towards higher H and lower L values. Its position corresponds thus to in-plane compressively strained Ge. The value of the relaxation degree amounts to, respectively, 50% and 75% for sample A and B. An evident difference of the FWHM in L direction is due to the thickness of the Ge epilayer. The position of the Ge peak in Figs. 4.15c and 4.15d indicates relaxed material with bulk lattice constant. The elongation along the line perpendicular to [101] most likely corresponds to twist and additional tilt of Ge lattice planes. The value of the latter obtained from the FWHM is 0.4° and 0.25° for sample C and D, respectively. This result shows, that the amount of lattice tilt and twist in the Ge nanostructures is reduced by thermal treatment.

A well pronounced SiGe(202) peak is found for samples C and D. Its position corresponds to the alloy pseudomorphic to Ge. This proves, that the Si diffusion occurred after nucleation of MDs and Ge relaxation. No additional SiGe layer pseudomorphic to Si was found which indicates, within the detection limit, no diffusion of Ge into the Si pillar. Similar conclusion was shown by Yamamoto [50] et al. in Ge grown on a blanket Si(001) substrates. A well pronounced SiGe peak corresponds to a layer of rather constant Ge concentration. Its estimated value amounts to around 80% in both cases. Additionally, a vertical streak from SiGe(202) at higher L values, corresponding to a SiGe layer of smaller Ge concentration, is found. The intensity of both, SiGe(202) peak and SiGe streak is higher for the annealed sample D indicating a stronger Si interdiffusion at the elevated annealing temperature.

To corroborate XRD results on the SiGe formation, EDX studies on samples C and D were performed. Si amount across the Ge/Si interface is shown in

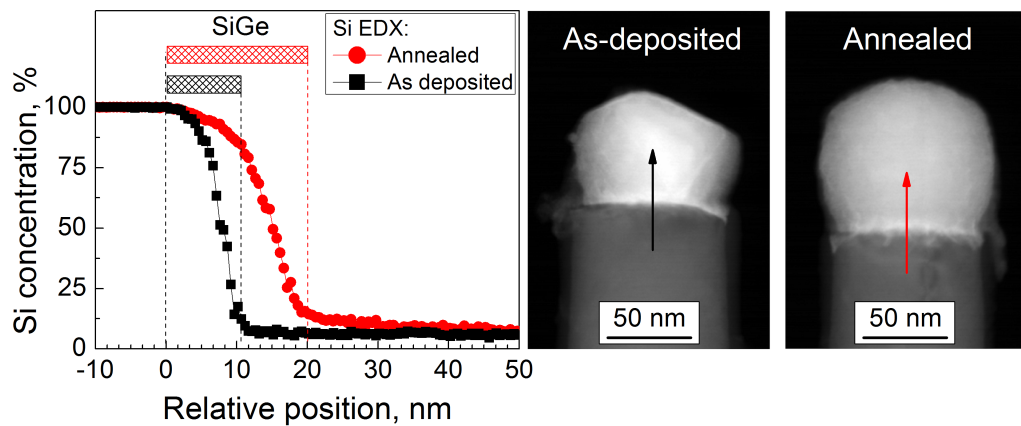


Figure 4.16: Si amount in an EDX scan across the Ge/Si interface for as-deposited and annealed sample shown in HAADF STEM micrographs on right. The arrows indicate the scan direction.

Fig. 4.16. In addition, scanning transmission electron microscope (STEM) images of two investigated nanostructures recorded by a high angle annular dark field (HAADF) detector are presented. The scan direction is indicated by an arrow. The zero-position on the scan x-axis was chosen to match the highest concentration of Si for both samples. The SiGe transition region is marked on the graph. It is evident, that for the annealed sample, Si diffuses further into Ge and forms a thicker SiGe alloy. This corresponds to a more intense SiGe(202) peak and the SiGe streak discussed above. However, the EDX results do not indicate the formation of a thicker SiGe layer with a constant ($\sim 80\%$) Ge concentration. This can be explained by the fact that: a) the thickness of the analysed lamella is thicker than a single nanostructure and b) the Ge/Si interface is not flat. In consequence, the detected signal is laterally averaged over the whole structure and no plateaus of Si concentration can be visible in the EDX scan.

4.2.3 Summary

In summary, we studied the growth and relaxation processes of Ge nanoclusters on 90 nm wide Si nanopillars. We showed, that during the deposition and in line with the theoretical predictions of the equilibrium crystal shape, Ge nanocrystals with well pronounced (001) and $\{113\}$ facets are formed on the Si nanostructures. Furthermore, the strain accumulated in Ge is plastically released by nucleation of MDs at the Ge/Si interface. This leads to the relaxation degree of 50%, 75%, and 100% respectively for 4, 8, and 80 nm thick

Ge. However, additional volume defects on $\{111\}$ crystal planes are formed during growth. In consequence, as deposited Ge nanostructures show a limited structural quality and uniformity of crystal shape and size. Our work proves, that this situation can be substantially improved by the annealing of Ge/Si nanostructures. Although an enhanced Si diffusion into Ge is detected after thermal treatment, Ge nanocrystals of increased crystal quality and shape/size uniformity are obtained.

After the growth studies presented here, investigation of Ge on Si nanostructures with the width of 50 nm are presented in the next section. Such fine nanoscale pillars are expected to trigger the strain partitioning phenomenon in the Ge/Si(001) system [71].

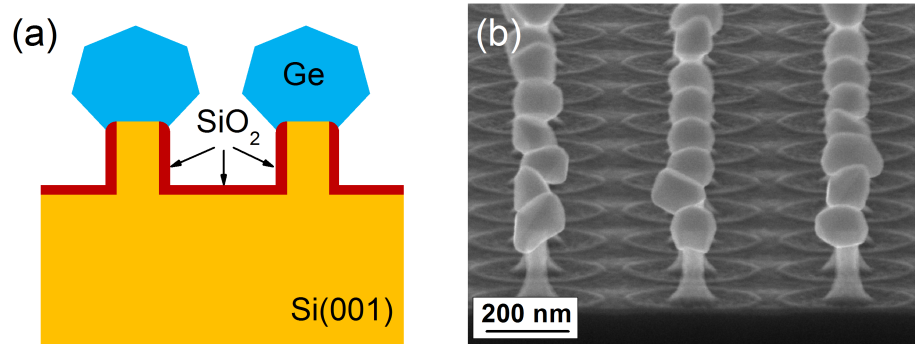


Figure 4.17: Ge clusters on free-standing Si nanopillars: a sketch (a) and SEM micrograph (b).

4.3 Compliant versus plastic relaxation of Ge nanostructures on free-standing sub 50 nm Si nanopillars

4.3.1 Scene setting

In our previous studies, we developed the selective growth process of Ge on Si nanostripes (section 4.1) and Si nanopillars (section 4.2) of 150 and 90 nm feature size, respectively. We demonstrated fully relaxed Ge achieved by 3D strain relief, plastic relaxation, and glide out of threading arms. Here, using 50 nm wide nanopillars together with synchrotron based x-ray diffraction and transmission electron microscopy we experimentally verify the nanoheteroepitaxy theory for the Ge/Si(001) system for which the compliant substrate effects were not observed so far. Although the structure dimensions are comparable to the theoretical values required for the strain partitioning phenomenon, the compliant character of Si is not unambiguously proven. In consequence, the strain is relieved by nucleation of misfit dislocations at the Ge/Si interface. By gliding out of threading arms, high quality Ge nanostructures are achieved. More details about the sample processing and characterization for this chapter can be found in section 3.3.

4.3.2 Results and discussion

The investigated nanostructures are shown in a scanning electron microscope (SEM) image in Fig. 4.17. High Ge growth selectivity and pronounced faceting of Ge crystals is visible.

In Fig. 4.18 we present the reciprocal space map (RSM) of the in-plane (400) Bragg reflection. The position of the Si(400) peak corresponds to its bulk lattice constant ($H = 4.00$). The compliant character of the Si pillar would be reflected by an asymmetry of its peak shape. In general, the in-plane tensile strain due to epi-Ge should result in an additional shoulder at $H < 4$. At the bottom of Fig. 4.18 we present an H-scan through Ge and Si (400) Bragg peaks at $K = 0$. Although, the Si peak is slightly asymmetric, the main observed shoulder lies at $H > 4$ indicating the in-plane compression by the SiO_2 growth mask [124, 129].

Although no dominating compliant character of Si nanopillars is observed, the position of the Ge peak ($H = 3.84$) corresponds to fully relaxed material with a bulk lattice constant. This fact indicates, that the relaxation of Ge occurs plastically by nucleation of misfit dislocations (MDs) at the Ge/Si interface, as discussed later. Experimental full width at half maximum (FWHM) along H is given by 0.009. Attributing this value to a finite crystal size effect, a Ge domain size of about 60 nm is extracted. As this value is of the same magnitude as the lateral size of the Ge nanostructure, it shows that heteroepitaxial single crystalline Ge nanoclusters of high quality structural coherence are achieved. Additional peak broadening is probably caused by microstrain close to MDs. FWHM along K is 0.038 and can be attributed to twist of Ge lattice planes with a value of 0.56° . In addition, there is no indication of Si interdiffusion into Ge. Interestingly, there are no pronounced streaks along $\{110\}$ directions around the in-plane Ge(400) peak. Such streaks can result from diffuse scattering tails of high density crystal defects on $\{111\}$ planes (e.g. stacking faults) [124].

Fig. 4.19 shows a RSM of the out-of-plane (202) Bragg reflection. A broad vertical streak at $H = 2$ corresponds to scattering from the Si(200) crystal truncation rod (CTR). Diffuse scattering around the Si peak results from finite crystal size effects, structural imperfection, and strain fields in the patterned Si(001) substrate. Here, we focus on possible strain signatures: for materials like Ge and Si with positive Poisson ratio, tensile strain in the in-plane direction results in compressive strain in the out-of-plane direction. In Fig. 4.19, we show the Poisson's line for pure Si (dashed). In addition, a scan along this line is presented in Fig. 4.20.

Diffuse scattering for $H > 2$ and $L < 2$ (area 1) corresponds to the Si pillar compressed in-plane by SiO_2 growth mask [124, 129] whereas the streak at $H < 2$ and $L > 2$ (area 2) stands for Si elastically deformed by epi-Ge and

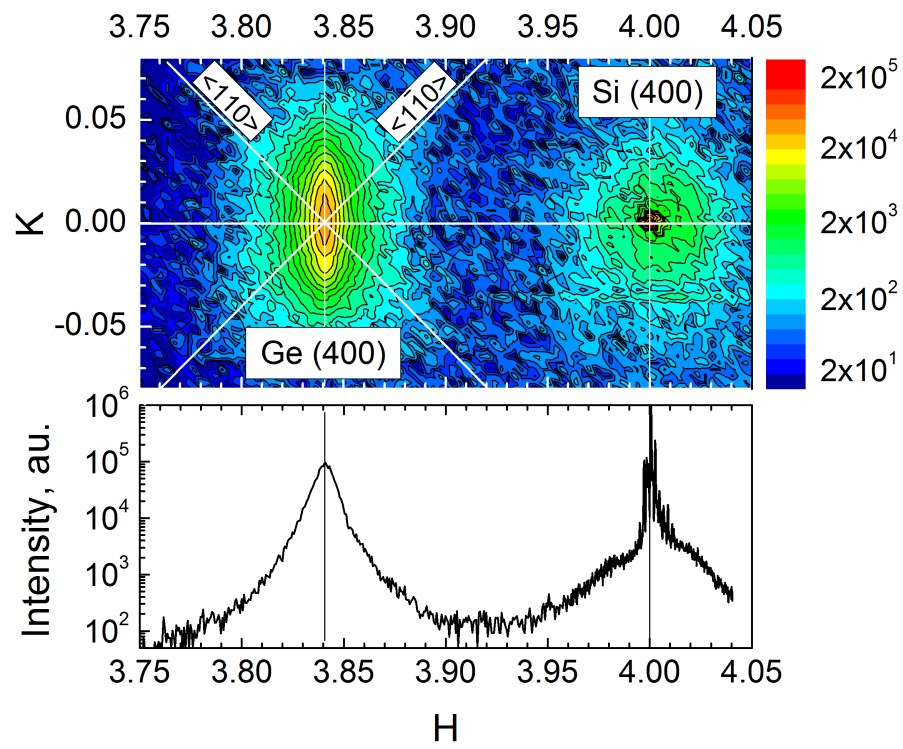


Figure 4.18: In-plane Si and Ge (400) Bragg reflection: RSM (top) and H-scan at $K = 0$ (bottom).

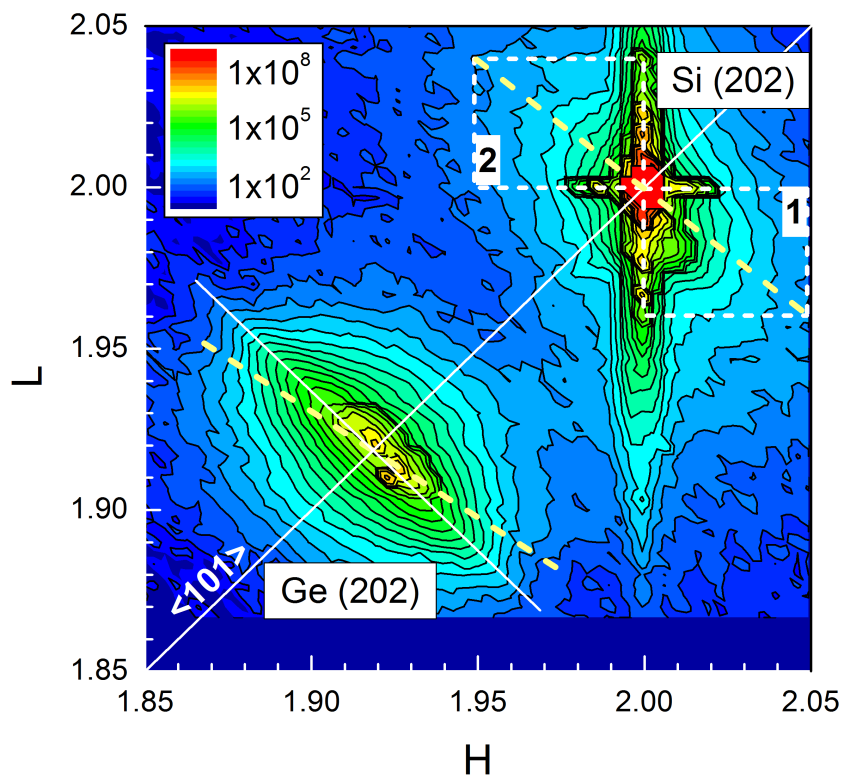


Figure 4.19: RSM of Si and Ge (202) Bragg reflections. Dashed line marks the Poisson's line.

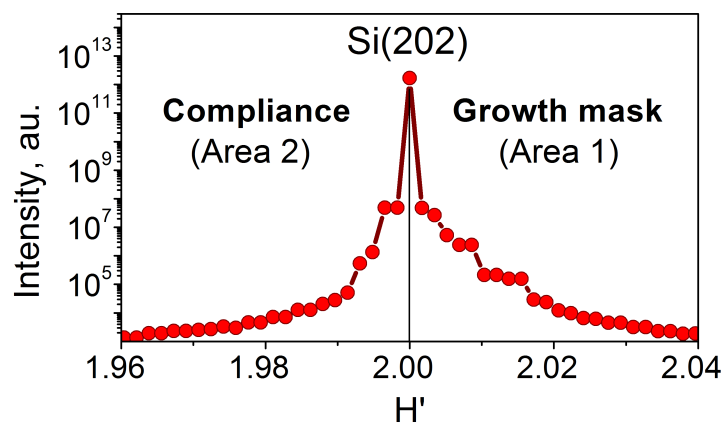


Figure 4.20: Intensity along the Poisson's line across the Si(202) Bragg reflection.

would be the proof of compliant behaviour of the nanopatterned substrate. The detection of diffuse scattering gives strong evidence that the GI-XRD detects a surface sensitive signal corresponding mainly to the Si nanostructures. Despite this fact, the diffuse XRD scattering in area 2 due to possible compliant behaviour of Si is less intense. In other words, the Si nanopillar structure is more affected by the SiO₂ growth mask than by compliant substrate effect due to Ge heteroepitaxy.

The position of the Ge(202) Bragg peak ($H = L = 1.92$) corresponds, similar to the (400) reflection, to fully relaxed material. Since the compliant character of Si was not observed, the relaxation of Ge occurs via nucleation of MDs. The calculated peak broadening due to finite dimensions of the crystal is in the range of 0.004. In consequence, the elongation along the line perpendicular to $\langle 101 \rangle$ (solid line in Fig. 4.19) most likely indicates twist and additional tilt of Ge lattice planes. The value of the latter obtained from the FWHM is 0.6°.

Despite high sensitivity of 3rd generation synchrotron radiation, no SiGe peak due to interdiffusion is observed.

To evaluate the crystal quality, transmission electron microscope (TEM) studies were performed using a Philips CM200 (see Fig. 4.21). The cross section (CS) image in Fig. 4.21a is an overview of a few nanostructures. Good growth selectivity is visible. Fig. 4.21b shows an example of a high quality Ge nanocluster. As expected, the relaxation of strain in the epilayer occurs by nucleation of MDs at the Ge/Si interface shown in a plane view (PV) in Fig. 4.21c. MDs can also contribute to tilt and twist of Ge and Si lattice planes observed in XRD [133]. It should be noted, that for all investigated symmetric Ge nanostructures, no additional structural defects were detected. Thus high quality Ge can be grown by the technique presented here. Any threading dislocations in the material glide out due to a small volume of the Ge crystal [52].

As already mentioned, Ge cluster shows well pronounced facets. Those are marked and labelled in Figs. 4.21b and c. Similar to the situation discussed in section 4.2, typical low energy $\{113\}$ facets are created [123]. (131) and (311) facets intersecting at (110) plane were found in the plane view TEM image in Fig. 4.21c. The edge formed on (110) plane and visible in Fig. 4.21b is labelled $(131)/(311)$.

In Fig. 4.21d, a plane view image over a bigger area is presented. Next to high quality symmetric Ge nanoclusters, asymmetric structures marked in circles are found. There are approximately two times more asymmetric than

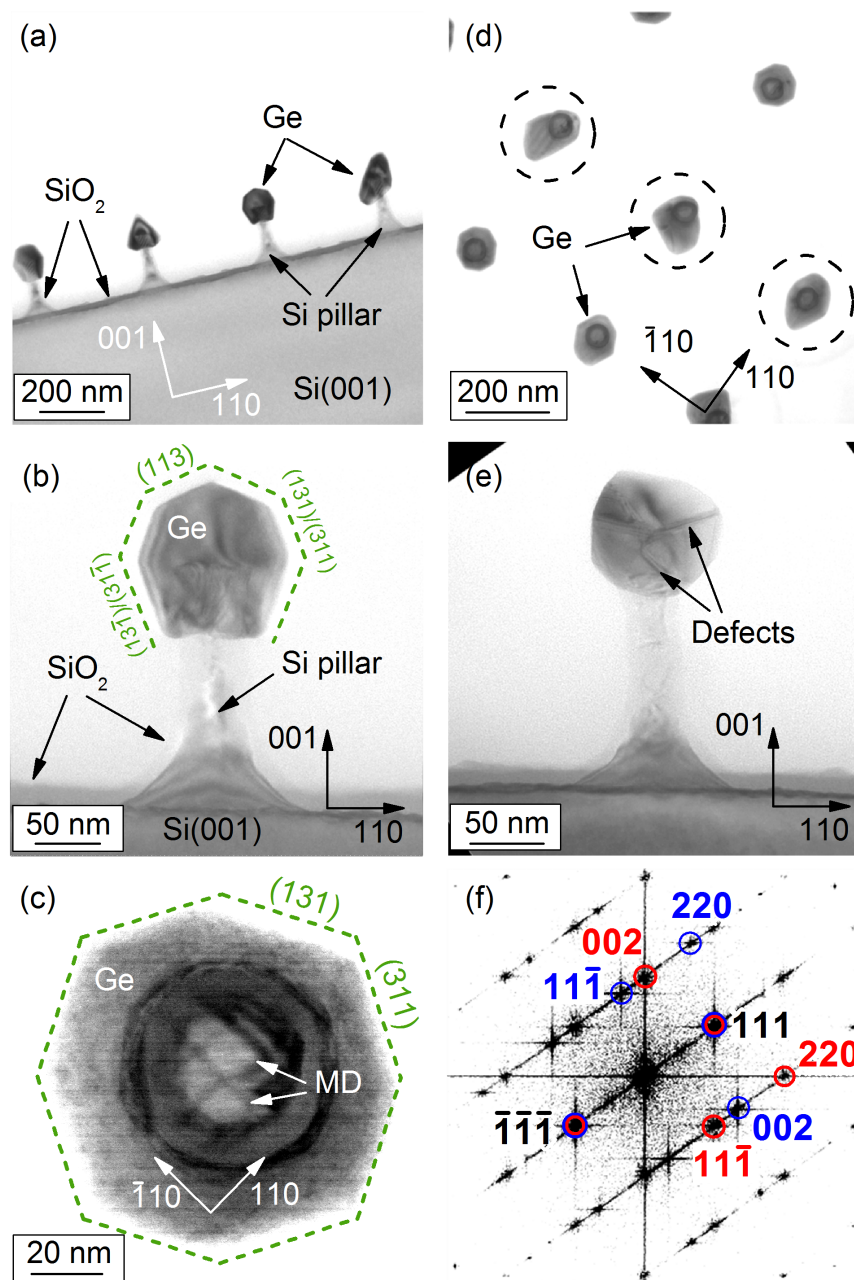


Figure 4.21: TEM micrographs: a) CS overview, b) side view of high quality Ge nanocluster, c) PV of Ge cluster, d) PV overview (asymmetric Ge crystals in circles), e) side view of asymmetric Ge nanostructure, f) FFT of HRTEM asymmetric Ge crystal containing dislocations.

symmetric Ge nanostructures. The coexistence of two types of Ge crystals suggests that the reason for the formation of asymmetric clusters could be related to the patterning of Si prior to Ge deposition. The patterning process could cause inhomogeneous residual strain fields in the Si pillar and deviation of the Si seed area that could finally alternate the Ge growth. A side view of an asymmetric Ge cluster is shown in Fig. 4.21e. We found that all asymmetric Ge crystals, besides MD at the Ge/Si interface, contain additional structural defects. In Fig. 4.21f, we present a fast Fourier transform (FFT) from a high resolution (HR) TEM image on a Ge region with defects. The analysis reveals the existence of two crystal orientations A and B separated by a series of twin boundaries. Type A orientation (orange circles) originates from the Si substrate, whereas type B orientation (blue circles) corresponds to the material with the stacking vector rotated 180° around $\langle 111 \rangle$ direction [59]. Thus, the observed asymmetric shape of Ge crystals is correlated with the presence of two different crystal orientations in Ge nanostructures. Moreover, inhomogeneous strain fields in the vicinity of defects can lead to strain enhanced migration growth. Further optimization of process parameters should allow growing high quality Ge nanoclusters as presented in Fig. 4.21b with MDs only at the Ge/Si interface.

4.3.3 Summary

In summary, we experimentally verified NHE using the Ge/Si(001) system. We presented fully relaxed Ge nanostructures grown on 50 nm wide Si pillars. Despite small dimensions, the compliant character of Si was not unambiguously proven. This is likely due to in-plane compressive strain from the SiO₂ growth mask. This result demonstrates that, in order to correctly describe complex thin film growth on the nanoscale studied here, NHE theory must be extended to include additional nanostructure effects (e.g. strain fields by growth masks).

Our TEM studies show that the strain in Ge is released by nucleation of MDs at the Ge/Si interface. Although additional structural defects were found in some clusters, by further process optimization, high quality, defect-free Ge nanostructures can be realized on free-standing Si nanopillars by selective CVD.

Chapter 5

Summary and Outlook

In the following, the discussion on Ge integration on nanopatterned Si(001) substrate will be summarized and the outlook on future research will be given.

5.1 Studies motivation

It is known that Si, dominating the platform for integrated circuitry (IC) technologies for over 50 years, is running into fundamental physical limits with further miniaturization ("More Moore") and / or functionalization ("More than Moore"). In this respect, new materials must be identified to enable new innovative functions without compromising the high performance of the Si chip baseline technology. The studies on the integration of Ge on Si(001) presented here, were motivated by its high potential for photonic application within the Si complementary metal oxide semiconductor (CMOS) platform.

Despite clear advantages of Ge integration in Si technology (e.g. identical to Si diamond crystal structure and CMOS compatibility), it is hindered by real challenges. Thermal and lattice mismatch, for example, result in too high defect levels which together with parasitic diffusion and formation of SiGe dramatically lowers the Ge optoelectronic properties. With this respect, an innovative **Nanoheteroepitaxy** (NHE) approach for Ge integration on Si(001) substrate was studied in this PhD thesis. NHE theory proposed by Zubia [71] gives a vision to grow defect-free Ge on free-standing nanoscale Si pillars. The high quality of the epilayer is expected to be the result of a) more efficient strain relief by 3D relaxation of the Ge cluster, b) dislocations gliding through the epilayer and exiting at free surfaces, and c) the strain partitioning phenomenon which is at the very heart of the compliant substrate (CS) effect. Please note, that a successful development of a compliant substrate

will prevent the formation of the misfit dislocation network at the Ge/Si interface whose parasitic "p-type doping" property is difficult to control and cannot be tolerated in Ge nanodevices. Theoretical calculations predict, that CS effects in Ge/Si(001) system can be triggered when pillars of sub-50 nm width are used. Taking this into account, the work presented here aimed on the structural studies on Ge selectively deposited by CVD on Si nanopatterns with dimensions ranging from 150 to 50 nm. The study was performed using various characterization techniques like Raman spectroscopy supported by finite element method (FEM) calculations, transmission electron microscopy (TEM), and most importantly synchrotron based x-ray diffraction.

5.2 Summary

At first, a successful process of Si(001) substrate nanopatterning and selective Ge deposition on 150 nm wide Si nanostripes was presented in section 4.1. The results indicate that, although thermal SiO₂ (used as the growth mask during Ge growth) stresses Si, the structural quality of the Si nanopattern is not affected. In addition, Ge grows in a relaxed form (see Fig. 5.1) with nearly the whole strain energy released by nucleation of misfit dislocations at the Ge/Si interface. The residual stress is mainly accumulated in the bird's beak region of Ge/Si nanostructures investigated by Raman spectroscopy and FEM analysis.

Next, studies on growth and relaxation processes in Ge nanocrystals on free-standing 90 nm wide Si(001) nanopillars were discussed in section 4.2. The strain energy in Ge epilayer with the thickness ranging from 4 - 80 nm releases plastically. As a result, Ge relaxation degrees between 50 and 100% were measured. Although Ge nanocluster growth follows the equilibrium crystal shape with well pronounced low energy (001) and {113} facets, the shape and size of crystals is not uniform and the structural quality is limited by volume defects on {111} planes. Substantial increase of crystal quality with high uniformity of shape and size is obtained after thermal processing (see Fig. 5.2). Elevated temperature leads, however, to unintended Si interdiffusion through the MD network into Ge and results in the formation of the SiGe interlayer pseudomorphic to Ge.

Finally, **in order to experimentally verify the vision of strain par-**

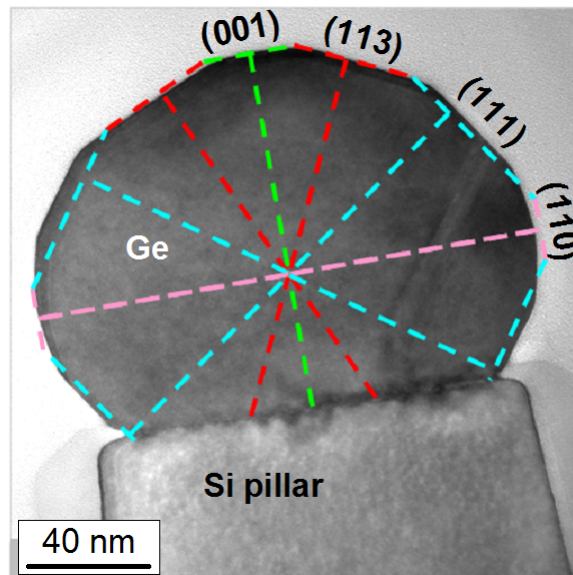


Figure 5.1: Cross section transmission electron microscope image of Ge/Si nanostructure. The faceted shape of Ge crystal fits well to the superimposed equilibrium crystal shape indicating relaxed epilayer growth.

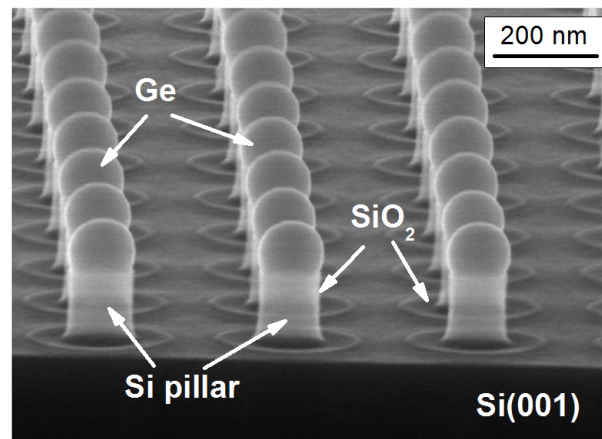


Figure 5.2: Scanning electron microscope image of highly uniform annealed Ge nanoclusters. Enhanced quality in terms of volume defects was proven by XRD measurements in section 4.2.

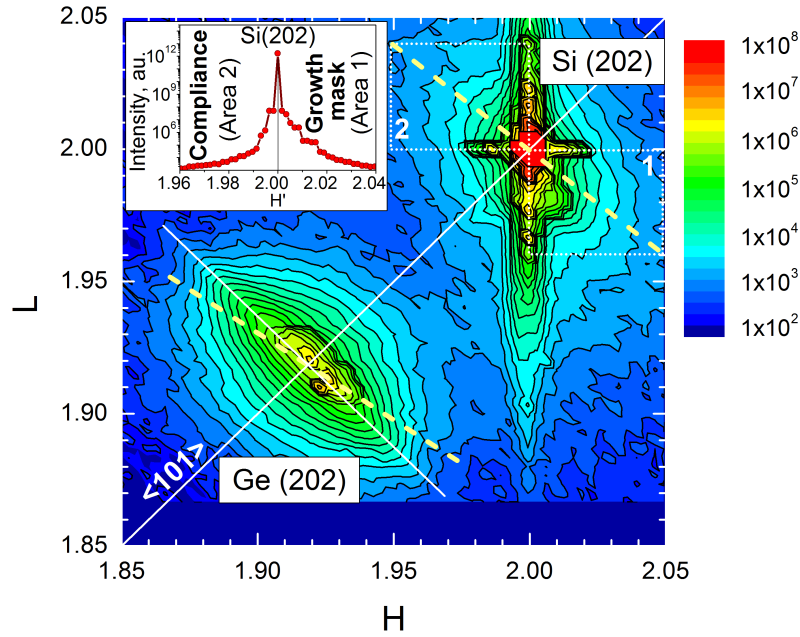


Figure 5.3: Reciprocal space map around the Ge and Si (202) Bragg reflections. The compliance of Si nanopillars is studied along the dashed Poisson's line in the inset.

titiation phenomena between Ge and Si, nanopillars with diameter of 50 nm were fabricated and studied in section 4.3. Despite such small dimensions, the compliant character of Si was not unambiguously proven. It was found, that thermal SiO_2 , protecting the substrate from unintended Ge deposition, limits Si pillar to act as a compliant substrate during Ge overgrowth (see Fig. 5.3). Despite the absence of strain partitioning, the presented results show, that after further optimization of nanopatterning process and growth conditions, the technique can be used to grow high quality Ge clusters with the height up to 100 nm.

5.3 Outlook

The results on Ge/Si nanostructures demonstrate that, NHE theory must be extended to consider additional nanostructure effects (like strain fields by growth masks etc) in order to successfully predict conditions required for compliant substrate effects. Based on the insights gained by this thesis, compliant substrate (CS) effects in the Ge/Si system can be realized in a few ways.

5.3.1 Growth mask optimization

One approach of triggering CS effects is to optimize the growth mask. Although, the thinning of thermal SiO₂ lowers the strain level in Si nanopillars as shown in section 4.1, further decrease of oxide thickness can eventually lead to a non-selective Ge growth. Thermal annealing of the Si nanostructures prior to Ge deposition was also found to be effective in reducing the SiO₂ growth mask strain. The use of alternative masking materials is currently under discussion. They should limit or even exclude the strain generation in Si prior to Ge deposition. Under consideration are such materials like CVD deposited oxide (TEOS) or Si₃N₄. In the latter case, however, a new selective Ge growth process must be developed.

5.3.2 Ge/Si nanostructures on Silicon-on-insulator (SOI)

Furthermore, the problem of strain in Si prior to Ge deposition can be eliminated when no growth mask is used. According to our first results, this approach is very promising. It requires, however, the use of Silicon-on-insulator (SOI) substrates. Here, Si cap layer is first thinned and then patterned down to the buried oxide to force the selective Ge growth. In order to enhance the capability of Si nanopillars to act as a CS, no additional growth mask on Si nanostructures is used in this approach. As a result, free-standing 10–50 nm high and 50–100 nm wide Si nanopillars with uncovered top and sidewalls on buried SiO₂ are fabricated. This wide set of height to width aspect ratio is to analyse in detail the influence of Si pillar dimensions on its capability to act as a CS for Ge nanoheteroepitaxy. As discussed already in chapter 2.4, thinner Si growth seeds are more promising and thus desirable in this approach.

First results and preliminary discussion

An example of Ge/Si nanostructures on SOI wafer is shown in a scanning electron microscope (SEM) image in Fig. 5.4. As expected, good selectivity of Ge deposition is observed with Ge nanoclusters grown only around free-standing Si nanoseeds. It is noted, that the pillars visible in the SEM image are SiO₂ resulting from the patterning process. The Si nanopillars themselves are not visible by SEM after Ge growth. To report evidence on the compliant substrate behaviour of free-standing Si nanostructures for high quality Ge nanoheteroepitaxy, high resolution, grazing incidence x-ray diffraction (HR-GIXRD) study was employed at ID01 beamline of the European Synchrotron

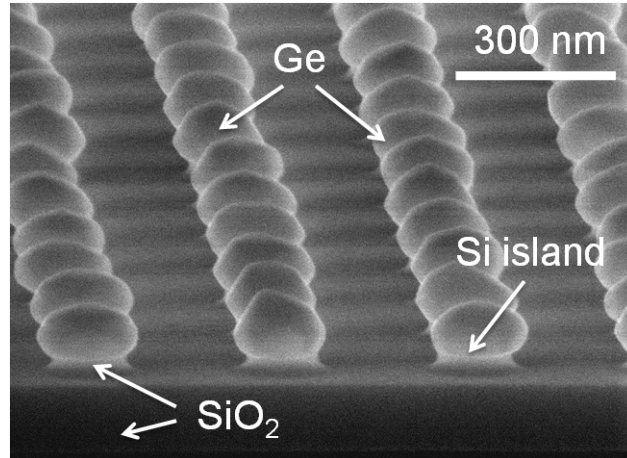


Figure 5.4: SEM micrograph of Ge/Si nanostructures on SOI wafer.

Radiation Facility (ESRF) in Grenoble (France).

To study the strain partitioning phenomenon in the Ge/Si nanostructures, a reciprocal space map (RSM) around Si and Ge (400) Bragg reflections, presented in Fig. 5.5, was performed. Next to the Si substrate peak at $H = 4$ and $K = 0$, an additional signal originating from Si nanoislands is visible at $H < 4$. This shift corresponds to the in-plane tensile strain in the Si nanoislands due to epi-Ge overgrowth. It thus points to **the presence of a compliant character of Si pillars for Ge nanoheteroepitaxy**. The position of the Ge related Ge(400) signal at $H > 3.84$ indicates **small amount of elastic strain in Ge nanostructures**. It is noted that Ge and Si peaks are shifted to smaller K values with respect to the substrate peak. This result is due to a certain twist of the Ge/Si nanostructures on top of buried SiO_2 and can be attributed to a slight misorientation in the wafer bonding process. It is noted, that **no diffuse scattering signals around the forbidden (200) Bragg reflection were found**. Although this result indicates the presence of Ge material of high structural quality with low defect densities, it does not mean that no defects are present at all. This is true because the complete Ge relaxation process cannot be fully attributed to the observed compliant substrate effect in the Si nanoisland because the strain in Si islands is too small. In other words, the Ge relaxation process is based on the compliant substrate as well as plastic defect nucleation terms. It is thus not surprising that evidence of single threading dislocations were found in the Ge nanostructures as well as misfit dislocations at the Ge/Si interface by transmission electron microscopy (TEM) studies. Fig. 5.6 shows an example of a TEM study of a typical Ge/Si

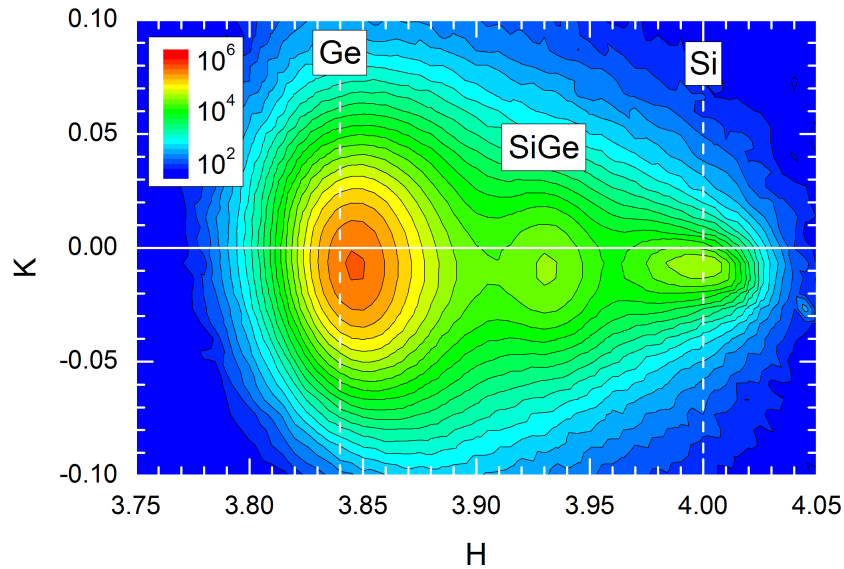


Figure 5.5: RSM around the in-plane Ge and Si (400) Bragg reflections.

nanostructure prepared on patterned SOI wafers.

In order to determine the role of Si and Ge interdiffusion, anomalous XRD studies around the Ge K-edge on the (620) Bragg reflection was performed. This high order Bragg reflection peak was chosen for improved sensitivity [134]. As an example, in Fig. 5.7 a diffraction pattern measured for three different energies is shown. The preliminary results indicate Si diffusion towards Ge and the **formation of a SiGe layer** for as-deposited samples. Moving away from the Ge/Si interface, the purity of the material (both in the Ge nanocluster and the Si pillar) increases. It is evident: The shift of Ge and Si island diffraction peaks (e.g. observed in the in-plane (400) reflection) is not caused

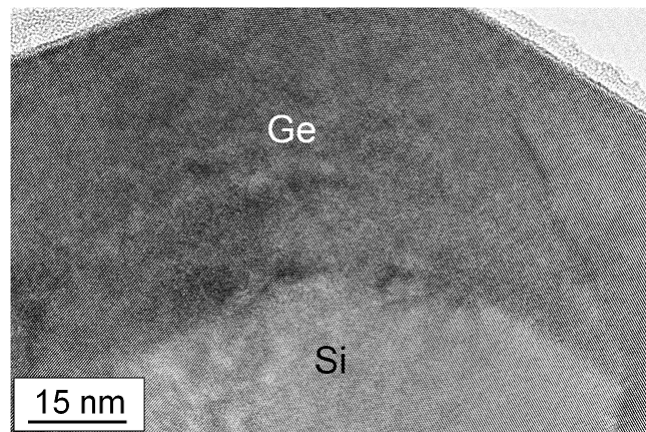


Figure 5.6: TEM image of Ge/Si nanostructure on SOI wafer.

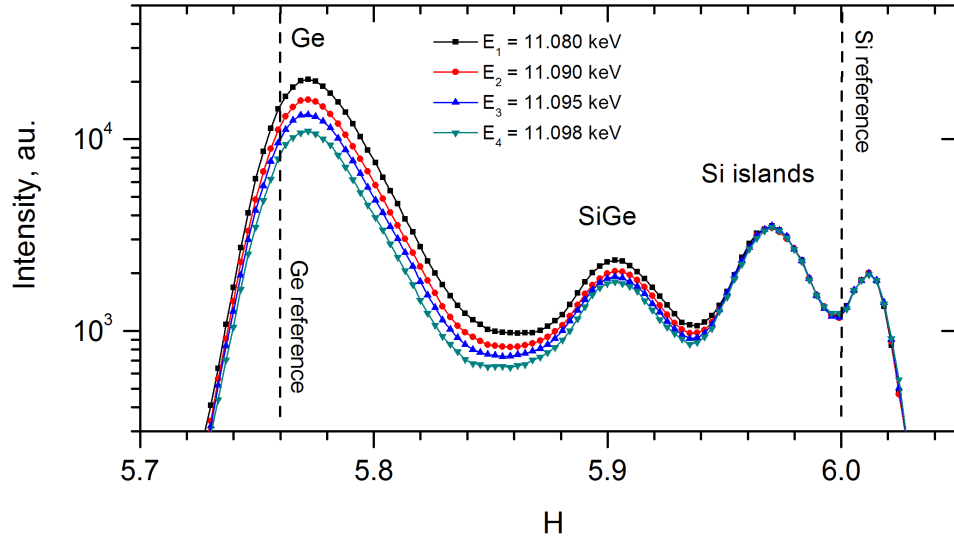


Figure 5.7: Anomalous XRD study of (620) Bragg peak for energies close to Ge K-edge. Si islands are free of Ge thus the displacement of Si(620) island peak is due to Ge epilayer strain.

by mixing between Ge and Si but corresponds to **the strain partitioning phenomenon between Ge nanostructures and Si nanopillars.**

To summarize, the **preliminary results on Ge/Si nanostructures on SOI substrate successfully demonstrate the existence of compliant substrate effects in Si nanopillars during Ge nanoheteroepitaxy. The complete relaxation process of Ge nanostructures is more complicated and includes in addition strain-driven SiGe diffusion phenomena as well as plastic relaxation by defect nucleation.** Although this "proof of principle" study already resulted in high quality Ge nanostructures on Si(001), future work will focus on the **optimization of the here demonstrated CS effect by unveiling fundamental differences of SiGe epitaxy between the well-studied bulk case and the innovative nanoheteroepitaxy approach.**

As nanoscale Ge/Si structures are of interest for future nanoelectronic and nanophotonic applications, future studies will focus also on **the characterization of Ge/Si nanostructures in terms of optoelectronic properties (e.g. photoluminescence, Hall measurements etc.).**

Finally, it is noted that here developed growth approach is fully

Si CMOS compatible and is not only relevant for Ge integration but also for other lattice mismatched alternative semiconductors (GaAs etc.) to enable higher performance / new functions in future Si microelectronics technologies.

Chapter 6

Scientific visibility

6.1 Publications in peer-reviewed journals

1. **G. Kozlowski**, P. Zaumseil, M. A. Schubert, Y. Yamamoto, J. Bauer, J. Matejova, T. Schulli, B. Tillack, and T. Schroeder, *Compliant substrate versus plastic relaxation effects in Ge nanoheteroepitaxy on free-standing Si(001) nanopillars*, Appl. Phys. Lett. **99**, 141901 (2011)
2. **G. Kozlowski**, Y. Yamamoto, J. Bauer, M. A. Schubert, B. Dietrich, B. Tillack, and T. Schroeder, *Selective Ge heteroepitaxy on free-standing Si (001) nanopatterns: A combined Raman, transmission electron microscopy, and finite element method study*, J. Appl. Phys. **110**, 053509 (2011)
3. **G. Kozlowski**, P. Zaumseil, M. A. Schubert, Y. Yamamoto, J. Bauer, T. U. Schüllli, B. Tillack, and T. Schroeder, *Growth and relaxation processes in Ge nanocrystals on free-standing Si(001) nanopillars*, Nanotechnology **submitted** (2011)
4. P. Zaumseil, Y. Yamamoto, J. Bauer, M. A. Schubert, J. Matejova, **G. Kozlowski**, T. Schroeder, and B. Tillack, *Characterization of Structural Defects in Germanium Epitaxially Grown on Nano-structured Silicon*, Solid State Phenomena, **178 - 179**, 43 (2011)
5. J. Matejova, **G. Kozlowski**, P. Zaumseil, V. Holy, and T. Schroeder, *X-ray Diffraction Analysis of Surface Si Nanostructures Used for Ge Nanoheteroepitaxy*, Mater. Struct., **submitted** (2011)
6. J. Bauer, Y. Yamamoto, P. Zaumseil, O. Fursenko, K. Schulz, **G. Kozlowski**, A. Schubert, T. Schroeder, and B. Tillack, *Nanostructured Sil-*

icon for Ge Nanoheteroepitaxy, Microelectronic Engineering **submitted** (2011)

7. P. Zaumseil, **G. Kozlowski**, M. A. Schubert, Y. Yamamoto, J. Bauer, T. Schüllli, B. Tillack, and T. Schroeder, *On the compliant behaviour of Ge nanocrystals on free-standing Si(001) nanopillars*, Phys. Rev. Lett. **to be submitted** (2012)
8. Y. Yamamoto, **G. Kozlowski**, P. Zaumseil, B. Tillack, *Low threading dislocation Ge on Si by combining deposition and etching*, Thin Solid Films **to be published** (2011)

6.2 Own presentations at conferences and courses

1. **G. Kozlowski**, P. Zaumseil, M. A. Schubert, Y. Yamamoto, J. Bauer, T. Schüllli, B. Tillack, and T. Schroeder, *On the compliant behaviour of Ge nanocrystals on free-standing Si(001) nanopillars*, ESRF Users' Meeting, Invited oral presentation (accepted), February 2012, Grenoble (France)
2. **G. Kozlowski**, P. Zaumseil, M. A. Schubert, Y. Yamamoto, J. Bauer, T. Schüllli, B. Tillack, and T. Schroeder, *On the strain partitioning phenomenon in Ge clusters on free-standing Si(001) nanopillars*, German Physical Society (DPG) Spring Meeting, Oral presentation (accepted), March 2012, Berlin (Germany)
3. **G. Kozlowski**, P. Zaumseil, M. A. Schubert, Y. Yamamoto, J. Bauer, T. Schüllli, B. Tillack, and T. Schroeder, *On the strain partitioning phenomenon in free-standing Ge/Si nanostructures on Si(001)*, 1. Workshop Leibniz Nano, Poster presentation (accepted), January 2012, Berlin (Germany)
4. **G. Kozlowski**, P. Zaumseil, M. A. Schubert, Y. Yamamoto, J. Bauer, J. Matejova, B. Tillack, and T. Schroeder, *Structure characterization on selective Ge nanostructures on free-standing Si(001) patterns*, 8th Autumn School on X-ray Scattering from Surfaces and Thin Layers, Oral presentation, October 2011, Smolenice (Slovakia)
5. **G. Kozlowski**, P. Zaumseil, M. A. Schubert, Y. Yamamoto, J. Bauer, B. Tillack, and T. Schroeder, *Structure characterization of Ge - nanoclus-*

ters on patterned Si(001), International Students and Young Scientists Workshop "Photonics and Microsystems", Oral presentation, July 2011, Cottbus (Germany)

6. **G. Kozlowski**, P. Zaumseil, M. A. Schubert, Y. Yamamoto, J. Bauer, B. Tillack, and T. Schroeder, *Structure characterization of Ge - nanoclusters on patterned Si(001)*, E-MRS Spring Meeting, Oral presentation, May 2011, Nice (France)
7. **G. Kozlowski**, P. Zaumseil, Y. Yamamoto, J. Bauer, B. Tillack, and T. Schroeder, *Structure characterization on selective Ge CVD heteroepitaxy on freestanding Si(001) nanopatterns*, German Physical Society (DPG) Spring Meeting, Oral presentation, March 2011, Dresden (Germany)

Bibliography

- [1] G. MOORE, *Fairchild Semiconductor internal publication* (1964).
- [2] G. MOORE, *Proc. SPIE* **2437**, 2 (1995).
- [3] ITRS, <http://public.itrs.net/>.
- [4] J. DORSCH, <http://www.edavision.com/200111/feature.pdf> (2001).
- [5] B. SCHALLER, http://research.microsoft.com/en-us/um/people/gray/moore_law.html (1996).
- [6] R. WILSON, <http://www.eetimes.com/electronics-news/4052047/The-Great-Debate-SOC-vs-SIP> (2005).
- [7] D. J. PAUL, *Semicond. Sci. Technol.* **19**, R75 (2004).
- [8] R. G. BEAUSOLEIL, J. AHN, N. BINKERT, A. DAVIS, D. FATTAL, M. FIORENTINO, N. P. JOUPPI, M. MCLAREN, C. M. SANTORI, R. S. SCHREIBER, S. M. SPILLANE, D. VANTREASE, and Q. XU, *IEEE LEOS Newsletter* **22**, 15 (2008).
- [9] K.-W. ANG, T.-Y. LIOW, Q. FANG, M. B. YU, F. F. REN, S. Y. ZHU, J. ZHANG, J. W. NG, J. F. SONG, Y. Z. XIONG, G. Q. LO, and D.-L. KWONG, *IEDM*, 1 (2009).
- [10] M. H. LIAO, T.-H. CHENG, and C. W. LIU, *Appl. Phys. Lett.* **89**, 261913 (2006).
- [11] H. PRESTING, T. ZINKE, A. SPLETT, H. KIBBEL, and M. JAROS, *Appl. Phys. Lett.* **69**, 2376 (1996).
- [12] Q. MI, X. XIAO, J. C. STURM, L. C. LENCHYSHYN, and M. L. W. THEWALT, *Appl. Phys. Lett.* **60**, 3177 (1992).

- [13] T.-H. CHENG, P.-S. KUO, C. T. LEE, M. H. LIAO, T. A. HUNG, and C. W. LIU, *IEDM*, 659 (2007).
- [14] S.-L. CHENG, J. LU, G. SHAMBAT, H.-Y. YU, K. SARASWAT, J. VUCKOVIC, and Y. NISHI, *Optics Express* **17**, 10019 (2009).
- [15] T.-H. CHENG, M. H. LIAO, L. YEH, T.-L. LEE, M.-S. LIANG, and C. W. LIU, *J. Appl. Phys.* **103**, 016103 (2008).
- [16] M. V. FISCHETTI and S. E. LAUX, *J. Appl. Phys.* **80**, 2234 (1996).
- [17] J. LIU, X. SUN, D. PAN, X. WANG, L. C. KIMERLING, T. L. KOCH, and J. MICHEL, *Optics Express* **15**, 11272 (2007).
- [18] J. LIU, X. SUN, R. CAMACHO-AGUILERA, L. C. KIMERLING, and J. MICHEL, *Opt. Lett.* **35**, 679 (2010).
- [19] Y. HUO, H. LIN, R. CHEN, M. MAKAROVA, Y. RONG, M. LI, T. I. KAMINS, J. VUCKOVIC, and J. S. HARRIS, *Appl. Phys. Lett.* **98**, 011111 (2011).
- [20] J. FAIST, F. CAPASSO, D. L. SIVCO, C. SIRTORI, A. L. HUTCHINSON, and A. Y. CHO, *Science* **264**, 553 (1994).
- [21] S. A. LYNCH, D. J. PAUL, P. TOWNSEND, G. MATMON, S. ZHANG, R. W. KELSALL, Z. IKONIC, . J. Z. P. HARRISON, D. J. NORRIS, A. G. CULLIS, C. R. PIDGEON, P. MURZYN, B. MURDIN, M. BAIN, H. S. GAMBLE, and Z. M. . W.-X. NI, *IEEE J. Sel. Top. Quant. Electron.* **12**, 1570 (2006).
- [22] G. CIASCA, M. D. SETA, G. CAPELLINI, F. EVANGELISTI, M. ORTOLANI, M. VIRGILIO, G. GROSSO, A. NUCARA, and P. CALVANI, *Phys. Rev. B* **79**, 085302 (2009).
- [23] M. D. SETA, G. CAPELLINI, Y. BUSBY, F. EVANGELISTI, M. ORTOLANI, M. VIRGILIO, G. GROSSO, G. PIZZI, A. NUCARA, and S. LUPI, *Appl. Phys. Lett.* **95**, 051918 (2009).
- [24] P. H. LIM, Y. KOBAYASHI, S. TAKITA, Y. ISHIKAWA, and K. WADA, *Appl. Phys. Lett.* **93**, 041103 (2008).
- [25] G. T. REED, *Silicon Photonics: The state of the art*, Willey, 2008.

- [26] J. LIU, M. BEALS, A. POMERENE, S. BERNARDIS, R. SUN, J. CHENG, L. C. KIMERLING, and J. MICHEL, *Nature Photon.* **2**, 433 (2008).
- [27] M. FUKUDA, *Optical semiconductor devices*, Wiley, 1999.
- [28] G. T. REED and A. P. KNIGHTS, *Silicon photonics: an introduction*, Wiley, 2004.
- [29] S. JONGTHAMMANURAK, J. LIU, K. WADA, D. D. CANNON, D. T. DANIELSON, D. PAN, L. C. KIMERLING, and J. MICHEL, *Appl. Phys. Lett.* **89**, 161115 (2006).
- [30] A. E.-J. LIM, T.-Y. LIOW, F. QING, N. DUAN, L. DING, M. YU, G.-Q. LO, and D.-L. KWONG, *Optics Express* **19**, 5040 (2011).
- [31] Y.-H. KUO, Y. K. LEE, Y. GE, S. REN, J. E. ROTH, T. I. KAMINS, D. A. B. MILLER, and J. S. HARRIS, *Nature* **437**, 1334 (2005).
- [32] L. PAVESI and G. GUILLOT, *Optical Interconnects: The Silicon Approach*, Springer, 2006.
- [33] Y. RONG, Y. GE, Y. HUO, M. FIORENTINO, M. TAN, T. KAMINS, T. J. OCHALSKI, G. HUYET, and J. S. HARRIS, *IEEE J. Sel. Top. Quant. Electron.* **16**, 85 (2010).
- [34] J. WANG and S. LEE, *Sensors* **11**, 696 (2011).
- [35] S. M. SZE, *Physics of Semiconductor Devices (2nd Edition)*, Willey, 1981.
- [36] S. FAMÁ, L. COLACE, G. MASINI, G. ASSANTO, and H.-C. LUAN, *Appl. Phys. Lett.* **81**, 586 (2002).
- [37] J. LIU, J. MICHEL, W. GIZIEWICZ, D. PAN, K. WADA, D. D. CANNON, S. JONGTHAMMANURAK, D. T. DANIELSON, L. C. KIMERLING, J. CHEN, F. O. ILDAY, F. X. KÄRTNER, and J. YASAITIS, *Appl. Phys. Lett.* **87**, 103501 (2005).
- [38] M. OEHME, J. WERNER, E. KASPER, M. JUTZI, and M. BERROTH, *Appl. Phys. Lett.* **89**, 071117 (2006).
- [39] J. MICHEL, J. LIU, and L. C. KIMERLING, *Nature Photon.* **4**, 527 (2010).

- [40] H. ZANG, S. J. LEE, W. Y. LOH, J. WANG, M. B. YU, G. Q. LO, D. L. KWONG, and B. J. CHO, *Appl. Phys. Lett.* **92**, 051110 (2008).
- [41] C. O. CHUI, A. K. OKYAY, and K. C. SARASWAT, *IEEE Photonic Tech. L.* **15**, 1585 (2003).
- [42] C.-H. LIN and C. W. LIU, *Sensors* **10**, 8797 (2010).
- [43] Y. KANG, H.-D. LIU, M. MORSE, M. J. PANICCIA, M. ZADKA, S. LITSKI, G. SARID, A. PAUCHARD, Y.-H. KUO, H.-W. CHEN, W. S. ZAOUI, J. E. BOWERS, A. BELING, D. C. MCINTOSH, X. ZHENG, and J. C. CAMPBELL, *Nature Photon.* **3**, 59 (2009).
- [44] R. B. EMMONS, *J. Appl. Phys.* **38**, 3705 (1967).
- [45] R. JASZEK, *J. Mater. Sci-Mater. El.* **12**, 1 (2001).
- [46] N. G. WEIMANN, L. F. EASTMAN, D. DOPPALAPUDI, H. M. NG, and T. D. MOUSTAKAS, *J. Appl. Phys.* **83**, 3656 (1998).
- [47] J.-L. FARVACQUE, *Mater. Sci. Eng. B* **42**, 110 (1996).
- [48] H.-C. LUAN, D. R. LIM, K. K. LEE, K. M. CHEN, J. G. SANDLAND, K. WADA, and L. C. KIMERLING, *Appl. Phys. Lett.* **75**, 2009 (1999).
- [49] J. M. BARIBEAU, T. E. JACKMAN, D. C. HOUGHTON, P. MAIGN, and M. W. DENHOFF, *J. Appl. Phys.* **63**, 5738 (1988).
- [50] Y. YAMAMOTO, P. ZAUMSEIL, T. ARGUIROV, M. KITTLER, and B. TILLACK, *Solid State Electron.* **60**, 2 (2011).
- [51] S. LURYI, A. KASTALSKY, and J. C. BEAN, *IEEE T. Electron. Dev.* **31**, 1135 (1984).
- [52] E. A. FITZGERALD, *Mater. Sci. Rep.* **7**, 87 (1991).
- [53] M. T. CURIE, S. B. SAMAVEDAM, T. A. LANGDO, C. W. LEITZ, and E. A. FITZGERALD, *Appl. Phys. Lett.* **72**, 1718 (1998).
- [54] Z. HUANG, J. OH, and J. C. CAMPBELL, *Appl. Phys. Lett.* **85**, 3286 (2004).
- [55] E. KASPER and K. LYUTOVICH, *Solid State Phenom.* **108-109**, 797 (2005).

- [56] K. LYUTOVICH, E. KASPER, M. OEHME, J. WERNER, and T. S. PEROVA, *Solid State Phenom.* **108-109**, 463 (2005).
- [57] D. BUCA, S. FESTE, B. HOLLÄNDER, S. MANTL, R. LOO, M. CAYMAX, R. CARIUS, and H. SCHAEFER, *Solid State Electron.* **50**, 32 (2006).
- [58] D. BUCA, R. A. MINAMISAWA, H. TRINKAUS, B. HOLLÄNDER, N. D. NGUYEN, R. LOO, and S. MANTL, *Appl. Phys. Lett.* **95**, 144103 (2009).
- [59] A. GIUSSANI, P. RODENBACH, P. ZAUMSEIL, J. DABROWSKI, R. KURPS, G. WEIDNER, H.-J. MÜSSIG, P. STORCK, J. WOLLSCHLÄGER, and T. SCHROEDER, *J. Appl. Phys.* **105**, 033512 (2009).
- [60] J. SEO, C. DIEKER, A. TAPPONNIER, C. MARCHIORI, M. SOUSA, J.-P. LOCQUET, J. FOMPEYRINE, A. ISPAS, C. ROSSEL, Y. PANAYIOTATOS, A. SOTIROPOULOS, and A. DIMOULAS, *Microelectron. Eng.* **84**, 2328 (2007).
- [61] T. SCHROEDER, A. GIUSSANI, H.-J. MUESSIG, G. WEIDNER, I. COSTINA, C. WENGER, M. LUKOSIUS, P. STORCK, and P. ZAUMSEIL, *Microelectron. Eng.* **86**, 1615 (2009).
- [62] T. SCHROEDER, A. GIUSSANI, J. DABROWSKI, P. ZAUMSEIL, H.-J. MÜSSIG, O. SEIFARTH, and P. STORCK, *Phys. Status Solidi C* **6**, 653 (2009).
- [63] I. BERBEZIER and A. RONDA, *Surf. Sci. Rep.* **64**, 47 (2009).
- [64] E. A. FITZGERALD, G. P. WATSON, R. E. PROANO, D. G. AST, P. D. KIRCHNER, G. D. PETTIT, and J. M. WOODALL, *J. Appl. Phys.* **65**, 2220 (1989).
- [65] M. YAMAGUCHI, M. TACHIKAWA, M. SUGO, S. KONDO, and Y. ITOH, *Appl. Phys. Lett.* **56**, 27 (1990).
- [66] J. BAI, J.-S. PARK, Z. CHENG, M. CURTIN, B. ADEKORE, M. CARROLL, A. LOCHTEFELD, and M. DUDLEY, *Appl. Phys. Lett.* **90**, 101902 (2007).

- [67] J.-S. PARK, J. BAI, M. CURTIN, B. ADEKORE, M. CARROLL, and A. LOCHTEFELD, *Appl. Phys. Lett.* **90**, 052113 (2007).
- [68] P. ZAUMSEIL, T. SCHROEDER, J.-S. PARK, J. G. FIORENZA, and A. LOCHTEFELD, *J. Appl. Phys.* **106**, 093524 (2009).
- [69] T. A. LANGDO, C. W. LEITZ, M. T. CURRIE, E. A. FITZGERALD, A. LOCHTEFELD, and D. A. ANTONIADIS, *Appl. Phys. Lett.* **76**, 3700 (2000).
- [70] G. WANG, E. ROSSEEL, R. LOO, P. FAVIA, H. BENDER, M. CAYMAX, M. M. HEYNS, and W. VANDERVORST, *Appl. Phys. Lett.* **96**, 111903 (2010).
- [71] D. ZUBIA and S. D. HERSEE, *J. Appl. Phys.* **85**, 6492 (1999).
- [72] E. A. FITZGERALD, *J. Vac. Sci. Technol. B* **7**, 782 (1989).
- [73] J. W. MATTHEWS, *J. Vac. Sci. Technol.* **12**, 126 (1975).
- [74] D. ZUBIA, S. H. ZAIDI, S. D. HERSEE, and S. R. J. BRUECK, *J. Vac. Sci. Technol. B* **18**, 3514 (2000).
- [75] J. HIRTH and J. LOTHE, *Theory of Dislocations*, Krieger, 1992.
- [76] J. P. HIRTH and A. G. EVANS, *J. Appl. Phys.* **60**, 2372 (1986).
- [77] Y. H. LO, *Appl. Phys. Lett.* **59**, 2311 (1991).
- [78] A. R. POWELL, S. S. IYER, and F. K. LEGOUES, *Appl. Phys. Lett.* **64**, 1856 (1994).
- [79] S. LURYI and E. SUHIR, *Appl. Phys. Lett.* **49**, 140 (1986).
- [80] S. BALAKUMAR, M. M. ROY, B. RAMAMURTHY, C. H. TUNG, G. FEI, S. TRIPATHY, C. DONGZI, R. KUMAR, N. BALASUBRAMANIAN, and D. L. KWONG, *Electrochem. Solid St.* **9**, G158 (2006).
- [81] M. MIYAO, K. TOKO, T. TANAKA, and T. SADOH, *Appl. Phys. Lett.* **95**, 022115 (2009).
- [82] M. MIYAO, T. TANAKA, K. TOKO, and M. TANAKA, *Appl. Phys. Express* **2**, 045503 (2009).

- [83] T. TANAKA, K. TOKO, T. SADOH, and M. MIYAO, *Appl. Phys. Express* **3**, 031301 (2010).
- [84] E. P. A. M. BAKKERS, M. T. BORGSTRÖM, and M. A. VERHEIJEN, *MRS Bulletin* **32**, 117 (2007).
- [85] M. HEURLIN, P. WICKERT, S. FÄLT, M. T. BORGSTRÖM, K. DEPERT, L. SAMUELSON, and M. H. MAGNUSSON, *Nano Lett.* **11**, 2028 (2011).
- [86] T. MARTENSSON, J. B. WAGNER, E. HILNER, A. MIKKELSEN, C. THELANDER, J. STANGL, B. J. OHLSSON, A. GUSTAFSSON, E. LUNDGREN, L. SAMUELSON, and W. SEIFERT, *Adv. Mater.* **19**, 1801 (2007).
- [87] J. E. AYERS, *Heteroepitaxy of Semiconductors: Theory, Growth and Characterization*, Taylor & Francis Group, 2007.
- [88] F. SHIMURA, *Semiconductor Silicon Crystal Technology*, Academic Press, 1989.
- [89] B. GALLAS, J. M. HARTMANN, I. BERBEZIER, M. ABDALLAH, J. ZHANG, J. J. HARRIS, and B. A. JOYCE, *J. Cryst. Growth* **201**, 547 (1999).
- [90] A. SAKAI, N. TAOKA, O. NAKATSUKA, S. ZAIMA, and Y. YASUDA, *Appl. Phys. Lett.* **86**, 221916 (2005).
- [91] Y. B. BOLKHOVITYANOV, A. S. DERYABIN, A. K. GUTAKOVSKII, and L. V. SOKOLOV, *J. Appl. Phys.* **107**, 123521 (2010).
- [92] M. PEACH and J. S. KOEHLER, *Phys. Rev.* **80**, 436 (1950).
- [93] J. MATTHEWS, A. BLAKESLEE, and S. MADER, *Thin Solid Films* **33**, 253 (1976).
- [94] A. H. COTTRELL and B. A. BILBY, *Proc. Phys. Soc. A* **62**, 49 (1949).
- [95] J. L. WEYHER and J. V. DE VEN, *J. Cryst. Growth* **88**, 221 (1988).
- [96] F. C. FRANK and W. T. READ, *Phys. Rev.* **79**, 722 (1950).
- [97] E. S. MEIERAN, *J. Appl. Phys.* **36**, 1497 (1965).

- [98] A. AUTHIER and A. R. LANG, *J. Appl. Phys.* **35**, 1956 (1964).
- [99] R. BEANLAND, *J. Appl. Phys.* **72**, 4031 (1992).
- [100] W. HAGEN and H. STRUNK, *Appl. Phys. A* **17**, 85 (1978).
- [101] I. D. WOLF, *Semicond. Sci. Tech.* **11**, 139 (1996).
- [102] S. M. HU, *J. Appl. Phys.* **70**, R53 (1991).
- [103] Z. ZHOU, C. LI, H. LAI, S. CHEN, and J. YU, *J. Cryst. Growth* **310**, 2508 (2008).
- [104] B. E. WARREN, *X-ray diffraction*, Dover publications Inc., 1990.
- [105] *European Synchrotron Radiation Facility*, <http://www.esrf.eu/>.
- [106] J. ALS-NIELSEN and D. MCMORROW, *Elements of modern x-ray physics*, Wiley, 2001.
- [107] A. SMEKAL, *Naturwiss.* **11**, 873 (1923).
- [108] C. V. RAMAN and K. S. KRISHNAN, *Nature* **121**, 501 (1928).
- [109] R. LOUDON, *Adv. Phys.* **13**, 423 (1964).
- [110] W. H. WEBER and R. MERLIN, *Raman Scattering in Material Science*, Springer, 2000.
- [111] M. CARDONA and G. GÜNTHERODT, *Light scattering in solids II: basic concepts and instrumentation*, Springer, 1982.
- [112] D. B. WILLIAMS and B. C. CARTER, *Transmission Electron Microscopy: A Textbook for Materials Science*, Plenum Press, 1996.
- [113] G. PELOSI, *IEEE Antennas Prop.* **49**, 180 (2007).
- [114] K. BATHE, *Finite element procedures in engineering analysis*, Prentice Hall, Inc., 1996.
- [115] G. BUCHANAN, *Finite element analysis*, McGraw Hill, 1995.
- [116] FLEXPDE, *PDE Solutions Inc.*: <http://www.pdesolutions.com/>.

- [117] H. RÜCKER, B. HEINEMANN, W. WINKLER, R. BARTH, J. BORNGRÄBER, J. DREWS, G. FISCHER, A. FOX, T. GRABOLLA, U. HAAK, D. KNOLL, F. KORNDÖRFER, A. MAI, S. MARSCHMEYER, P. SCHLEY, D. SCHMIDT, J. SCHMIDT, K. SCHULZ, B. TILLACK, D. WOLANSKY, and Y. YAMAMOTO, *IEEE BCTM*, 166 (2009).
- [118] S. GANESAN, A. A. MARADUDIN, and J. OITMAA, *Ann. Phys.* **56**, 556 (1970).
- [119] E. ANASTASSAKIS, A. PINCZUK, E. BURSTEIN, F. H. POLLAK, and M. CARDONA, *Solid State Commun.* **8**, 133 (1970).
- [120] I. D. WOLF, H. E. MAES, and S. K. JONES, *J. Appl. Phys.* **79**, 7148 (1996).
- [121] *Weierstrass Institute for Applied Analysis and Stochastics: Annual Research Report* (2009).
- [122] S. E. CRANDALL, N. C. DAHL, and T. J. LARDNER, *Introduction to the Mechanics of Solids*, McGraw-Hill, 1978.
- [123] A. A. STEKOLNIKOV and F. BECHSTEDT, *Phys. Rev. B* **72**, 125326 (2005).
- [124] P. ZAUMSEIL, Y. YAMAMOTO, J. BAUER, M. A. SCHUBERT, and T. SCHROEDER, *J. Appl. Phys.* **109**, 023511 (2011).
- [125] I. V. MARKOV, *Crystal Growth for Beginners*, World Scientific, 2003.
- [126] P. MÜLLER and R. KERN, *Appl. Surf. Sci.* **162/163**, 133 (2000).
- [127] S. MIRACLE-SOLE, *J. Stat. Phys.* **79**, 183 (1995).
- [128] J. BRICMONT, J. R. FONTAINE, and J. L. LEBOWITZ, *J. Stat. Phys.* **29**, 193 (1982).
- [129] G. KOZLOWSKI, Y. YAMAMOTO, J. BAUER, M. A. SCHUBERT, B. DIETRICH, B. TILLACK, and T. SCHROEDER, *J. Appl. Phys.* **110**, 053509 (2011).
- [130] G. RENAUD, P. GUÉNARD, and A. BARBIER, *Phys. Rev. B* **58**, 7310 (1998).

- [131] M.-I. RICHARD, A. MALACHIAS, J.-L. ROUVIÈRE, T.-S. YOON, E. HOLMSTRÖM, Y.-H. XIE, V. FAVRE-NICOLIN, V. HOLÝ, K. NORDLUND, G. RENAUD, and T.-H. METZGER, *Phys. Rev. B* **84**, 075314 (2011).
- [132] M.-I. RICHARD, T. H. METZGER, V. HOLÝ, and K. NORDLUND, *Phys. Rev. Lett.* **99**, 225504 (2007).
- [133] B. J. SPENCER and J. TERSOFF, *Phys. Rev. B* **63**, 205424 (2001).
- [134] T. U. SCHÜLLI, J. STANGL, Z. ZHONG, R. T. LECHNER, M. SZTUCKI, T. H. METZGER, , and G. BAUER, *Phys. Rev. Lett.* **90**, 066105 (2003).